Journal of Instrumentation

SISSA

OPEN ACCESS

Performance of the CMS Level-1 trigger in proton-proton collisions at $\sqrt{s}$ = 13 TeV

To cite this article: A.M. Sirunyan *et al* 2020 *JINST* **15** P10017

View the article online for updates and enhancements.



IOP ebooks™

Bringing together innovative digital publishing with leading authors from the global scientific community.

Start exploring the collection–download the first chapter of every title for free.

This content was downloaded from IP address 155.198.10.231 on 17/03/2021 at 09:16

Published by IOP Publishing for Sissa Medialab

Received: *June 17, 2020*
Accepted: *August 20, 2020*
Published: *October 19, 2020*

Performance of the CMS Level-1 trigger in proton-proton collisions at $\sqrt{s} = 13$ TeV



The CMS collaboration

E-mail: cms-publication-committee-chair@cern.ch

Abstract: At the start of Run 2 in 2015, the LHC delivered proton-proton collisions at a center-of-mass energy of 13 TeV. During Run 2 (years 2015–2018) the LHC eventually reached a luminosity of 2.1×10^{34} cm^{-2} s^{-1}, almost three times that reached during Run 1 (2009–2013) and a factor of two larger than the LHC design value, leading to events with up to a mean of about 50 simultaneous inelastic proton-proton collisions per bunch crossing (pileup). The CMS Level-1 trigger was upgraded prior to 2016 to improve the selection of physics events in the challenging conditions posed by the second run of the LHC. This paper describes the performance of the CMS Level-1 trigger upgrade during the data taking period of 2016–2018. The upgraded trigger implements pattern recognition and boosted decision tree regression techniques for muon reconstruction, includes pileup subtraction for jets and energy sums, and incorporates pileup-dependent isolation requirements for electrons and tau leptons. In addition, the new trigger calculates high-level quantities such as the invariant mass of pairs of reconstructed particles. The upgrade reduces the trigger rate from background processes and improves the trigger efficiency for a wide variety of physics signals.

Keywords: Large detector-systems performance; Trigger algorithms

ArXiv ePrint: 2006.10165

© 2020 CERN for the benefit of the CMS collaboration. Published by IOP Publishing Ltd on behalf of Sissa Medialab. Original content from this work may be used under the terms of the Creative Commons Attribution 4.0 licence. Any further distribution of this work must maintain attribution to the author(s) and the title of the work, journal citation and DOI.

https://doi.org/10.1088/1748-0221/15/10/P10017

2020 JINST 15 P10017

Contents

1 Introduction **2**

2 The CMS detector **3**

3 The LHC in Run 2 **3**

4 The physics program and the trigger menu **4**

5 The Level-1 trigger architecture **8**

6 The Level-1 muon trigger and its performance **12**
- 6.1 Barrel muon trigger primitives 13
- 6.2 Endcap RPC trigger primitives 14
- 6.3 Barrel muon track finder 14
- 6.4 Overlap muon track finder 14
- 6.5 Endcap muon track finder 15
- 6.6 Global muon trigger 16
- 6.7 Performance 16

7 The Level-1 calorimeter trigger and its performance **21**
- 7.1 Input calorimeter trigger primitive processing 21
- 7.2 The electron and photon trigger algorithm 22
- 7.3 The hadronic tau lepton trigger algorithm 25
- 7.4 The jet and energy sum trigger algorithms 28
- 7.5 Adjustments for heavy ion collisions 32

8 The global trigger **32**
- 8.1 Dedicated analysis triggers 33

9 Data certification and validation **34**

10 Summary and conclusions **36**

A Level-1 trigger prefiring **38**

The CMS collaboration **42**

2020 JINST 15 P10017

1 Introduction

The CERN LHC collides bunches of particles in the CMS and ATLAS experiments at a maximum rate of about 40 MHz, where the bunches are spaced 25 ns apart. Of these only about 1000 per second can be recorded for further analysis. The Level-1 trigger system uses custom hardware processors to select up to 100 kHz of the most interesting events with a latency of 4 µs. The High Level Trigger (HLT) then performs a more detailed reconstruction, including particle tracking, on a commodity computing processor farm, reducing the rate by another factor of 100 in a few hundred milliseconds. Events passing the HLT selection are sent to a separate computing farm for more accurate event reconstruction and storage.

The LHC operation is organized into periods of physics production, where protons or heavy ions are collided, and periods of shutdown during which repairs and upgrade work are performed. The original CMS trigger system performed efficiently in the LHC Run 1 (between 2009 and 2013) and 2015. Its design is described in ref. [1] and its performance in ref. [2]. In 2015 the LHC increased the proton-proton center-of-mass collision energy from 8 to 13 TeV. The instantaneous luminosity steadily increased throughout Run 2, which ended in 2018. These changes were designed to provide a larger data set for studies of rare interactions and searches for new physics, but they also presented several challenges to the trigger system. Improved trigger algorithms were needed to enhance the separation of signal and background events and to provide more accurate energy reconstruction in the presence of a larger number of simultaneous collisions per LHC bunch crossing (pileup).

The CMS Collaboration undertook a major upgrade to the Level-1 trigger system (Phase 1) between Run 1 and Run 2, and plans a second upgrade (Phase 2) after Run 3 ends (expected in 2024). The Phase 1 upgrade replaced all of the Level-1 trigger hardware, cables, electronics boards, firmware, and software, as described in the Technical Design Report for the Level-1 trigger upgrade [3]. Despite higher instantaneous luminosity, energy, and pileup, the upgraded Level-1 trigger maintained or increased its efficiency to separate the chosen signal events from background, because of finer detector input granularity, enhanced object reconstruction (e.g., μ, e/γ, jet, τ, and energy sums), and correlated multi-object triggers targeting specific physics signatures.

This paper describes the trigger algorithms of the Phase 1 Level-1 trigger upgrade and reports their performance, measured using Run 2 data. A brief overview of the CMS detector is given in section 2. Section 3 describes the performance of the LHC and its impact on the CMS trigger system in Run 2. Section 4 provides an overview of the large collection of algorithms used to select events for physics measurements. Section 5 describes the design of the upgraded Level-1 trigger, including updates since ref. [3]. The reconstruction algorithms, along with their performance, are described in detail for each subdetector: the muon trigger in section 6, and the calorimeter trigger in section 7; appendix A provides details on a calorimeter trigger issue that affected Run 2 data. Section 8 provides two examples of new multi-object global trigger algorithms, while section 9 describes how the data quality of the Level-1 trigger is monitored in real time. Section 10 summarizes and draws conclusions regarding the achievements of the upgraded Level-1 trigger in Run 2.

2020 JINST 15 P10017

2 The CMS detector

The central feature of the CMS apparatus is a superconducting solenoid of 6 m internal diameter, providing a magnetic field of 3.8 T. Within the solenoid volume are a silicon pixel and strip tracker, a lead tungstate crystal electromagnetic calorimeter (ECAL), and a brass and scintillator hadron calorimeter (HCAL), each composed of a barrel and two endcap sections. Forward calorimeters extend the pseudorapidity (η) coverage provided by the barrel and endcap detectors. Muons are detected in gas-ionization chambers embedded in the steel flux-return yoke outside the solenoid. Drift tubes (DTs) cover the central region ($|\eta| < 1.2$), cathode strip chambers (CSCs) are installed in the endcaps ($0.9 < |\eta| < 2.4$), and resistive plate chambers (RPCs) provide overlap out to $|\eta| < 1.7$. A more detailed description of the CMS detector, together with a definition of the coordinate system used and the relevant kinematic variables, can be found in ref. [4].

3 The LHC in Run 2

Trigger performance depends on the running conditions of the LHC, such as instantaneous luminosity, number of colliding bunches, and even the structure of the filling scheme. The LHC was designed to collide protons with a center-of-mass energy of 14 TeV and an instantaneous luminosity corresponding to 1.0×10^{34} cm^{-2} s^{-1}, but it initially operated at lower energies and intensities. During Run 1 the center-of-mass energy was increased in steps up to 8 TeV with a peak instantaneous luminosity near 8.0×10^{33} cm^{-2} s^{-1}. At that time, the LHC operated with a longer minimum bunch spacing of 50 ns, instead of the originally foreseen 25 ns.

During the first long shutdown period of the LHC in 2013–2014, the accelerator was modified to provide safe operation at 13 TeV with 25 ns bunch spacing, and the CMS experiment underwent upgrades [5] to prepare for a dramatic increase in collision rate. Run 2 of the LHC lasted from 2015 until the end of 2018 with peak instantaneous luminosities of about 2.1×10^{34} cm^{-2} s^{-1}. A typical filling scheme for the LHC in Run 2 comprised 2556 proton bunches per beam out of 3564 possible bunch locations. The bunches were grouped in "trains" of 48 bunches with 25 ns spacing, with larger gaps between trains. Of these, 2544 bunches collided at the CMS interaction point. In the second long shutdown of the LHC (2019–2020), upgrades to the accelerator are planned, possibly increasing the center-of-mass energy for Run 3 (foreseen to start late 2021 or early 2022), and allowing the LHC to sustain a maximum instantaneous luminosity of 2.0×10^{34} cm^{-2} s^{-1} for longer periods of time.

In 2017 the LHC suffered frequent beam dumps. These were caused when an electron cloud generated by tightly packed bunches interacted with frozen gas in the beam pipe. The gas had become trapped in one area of the LHC during the year-end technical stop between 2016 and 2017 [6]. To mitigate this effect, the LHC moved to a special "8b4e" filling scheme in September 2017. In this scheme the standard 48 bunch trains are replaced by mini-trains of 8 filled bunches followed by 4 empty slots, suppressing the formation of electron clouds. Since the 8b4e filling scheme allows a maximum of 1916 filled bunches in the LHC, the peak instantaneous luminosity was leveled to $\approx 1.55 \times 10^{34}$ cm^{-2} s^{-1}, so the average pileup would not exceed 60. The LHC delivered 41.0 and 49.8 fb^{-1} of proton-proton collisions to CMS in 2016 and 2017, respectively, during which 35.9 and 41.5 fb^{-1} of good quality data were recorded.

2020 JINST 15 P10017

In 2018 the beam dump issues had largely been mitigated so that a return to the preferred nominal scheme was possible. The advantage of this scheme is the use of a larger number of colliding bunches, providing higher instantaneous luminosity without increasing the pileup. The peak luminosity of about $2.0 \times 10^{34}\,\mathrm{cm^{-2}\,s^{-1}}$ led to an average pileup of 55, similar to that at the start of 2017. The LHC ran smoothly in 2018 and delivered an integrated luminosity of $68.0\,\mathrm{fb^{-1}}$ to CMS, which recorded $59.7\,\mathrm{fb^{-1}}$ of good quality data.

The LHC periodically provides short special runs, such as the van der Meer scans, with non-standard beam settings, which require dedicated triggers and calibrations. The precise measurement of the integrated luminosity recorded by CMS is a necessary ingredient for most of the CMS physics results, and the CMS experiment has several detectors dedicated to this measurement. The van der Meer scans provide data necessary to calibrate these measurements.

During the van der Meer scans, the LHC beams are scanned across each other to provide an accurate luminosity calibration. The trigger system is used to measure the rate of the beam collisions, which is used to calculate the luminosity, as described in ref. [7]. For some periods of the van der Meer scan, the Level-1 trigger system records, with high rate, only events from selected bunch crossings in the LHC orbit bunch structure to improve the precision of the luminosity calibration.

4 The physics program and the trigger menu

The CMS physics program targets many areas of interest to the high-energy physics community. After the discovery of the Higgs boson [8–10], measuring its properties, which are currently compatible with the standard model (SM) predictions [11], became of central importance. Searches for supersymmetric and exotic particles, together with candidates for dark matter, are also central to the CMS physics program and they require a high-performance trigger. Such a high-performance trigger also enables precision measurements of SM properties in the electroweak, top quark, and quantum chromodynamics (QCD) sectors, with special attention to the physics of bottom quarks, where triggering objects often have low transverse momentum (p_{T}). Heavy ion collisions are included in the CMS physics program, expanding our knowledge of quark-gluon plasma dynamics.

The Level-1 trigger information from the muon and calorimeter detectors with coarse granularity and precision is used to select collision events for investigations in all of the previously mentioned physics areas. The selection is performed using a list of algorithms (known as "seeds"), which check events against predetermined criteria, that are collectively called the "menu". Any event that satisfies the conditions of at least one seed in the menu is accepted for further processing in the trigger chain. This initiates a readout of the complete detector information from the data acquisition system, and the data are sent to the HLT. The broad range of menu algorithms reflects the wide variety of research interests of the CMS Collaboration. The Level-1 menu evolves with shifting CMS physics priorities and adapts to changes in beam or detector performance.

The most straightforward trigger algorithms consist of criteria applied to one or more objects of a single type, such as muons, hadronic jets, tau leptons, photons or electrons, scalar sum of transverse energy (H_{T}), and the energy corresponding to the vector sum of the transverse missing momentum ($E_{\mathrm{T}}^{\mathrm{miss}}$). Typical criteria include thresholds on the transverse component of the object's energy E_{T} (or momentum), and on its η. Signal processes with massive particles typically produce objects at high p_{T} and low $|\eta|$ values (central in the detector), whereas the vast majority of background

2020 JINST 15 P10017

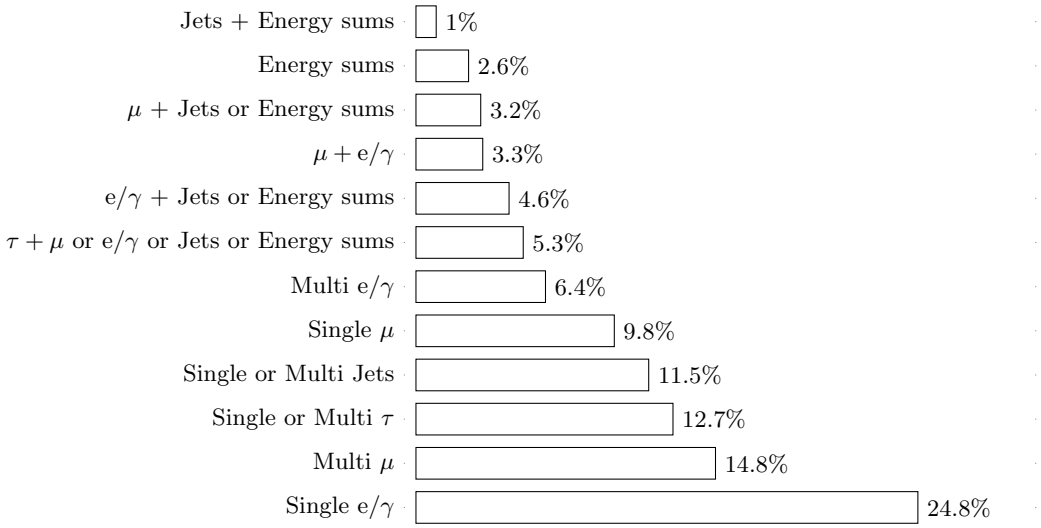


Figure 1. Fractions of the 100 kHz rate allocation for single- and multi-object triggers and cross triggers in a typical CMS physics menu during Run 2.

objects are low p_{T} and tend to have higher $|\eta|$. Single- and double-object seeds form the majority of the menu and cover about 75% of the available rate. Muon and electron thresholds are chosen to efficiently select leptonic W and Z boson decays, and $\tau\tau$ thresholds are set to maximize the Higgs boson acceptance in this decay channel.

The "cross" seeds combine physics objects of different types, for example a muon and a jet, allowing lower thresholds that target a diverse range of signals. More complex algorithms using correlations between multiple objects select highly specific signal events, such as hadrons decaying to muons, or Higgs bosons produced via vector boson fusion (VBF). Finally, a small fraction of events passing less restrictive algorithms are collected to calibrate the detectors and measure trigger efficiencies. Figure 1 shows the "proportional rate", the fraction of the maximum Level-1 trigger rate allocated to single-, multi- (same type), and cross- (different type) object seeds. In the proportional rate calculation, events triggered by N different seeds are weighted by $1/N$ to ensure that the total sums to 100%.

The menu algorithms are designed using a simulation of the Level-1 object reconstruction using either Monte Carlo (MC) simulated collision events or, where possible, previously collected data. The seed thresholds are adjusted to achieve a total menu rate that is less than 100 kHz, estimated with data collected with a trigger that requires only a crossing of proton bunches, referred to as a zero-bias trigger. The detection of the crossing of bunches consists of the coincidence of two simultaneous signals from the two beam pick-up monitors installed at the opposite ends of CMS along the beam line.

Trigger algorithm rates depend on the ability of the trigger reconstruction to discriminate between signal objects, arising in hard collisions, from backgrounds or misidentified objects. This becomes more difficult as pileup increases. Figure 2 shows the rate of some benchmark trigger seeds targeting leptons (left) and hadrons (right) as a function of pileup. Rate and pileup are measured

2020 JINST 15 P10017

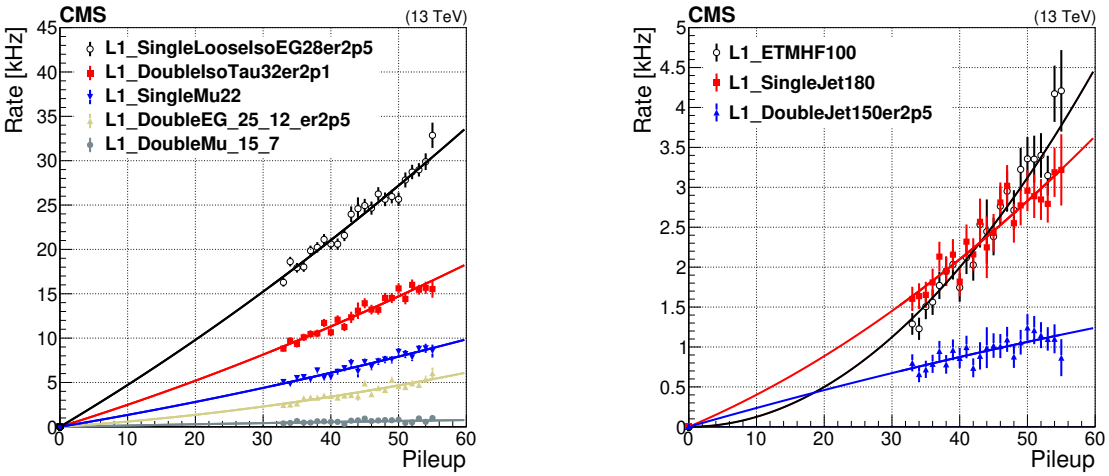


Figure 2. Level-1 trigger rates as a function of pileup for some benchmark seeds targeting leptons (left) and hadrons (right). Rates are measured using data recorded during the 2018 LHC run. Definitions of the seed names are in table 1. The curves represent fits to the data points that are quadratic and constrained to pass through the origin.

Table 1. Detailed description of Level-1 trigger seed names used in figure 2.

Algorithm name	Description
L1_SingleLooseIsoEG28er2p5	Single loosely isolated e/γ with $E_T > 28$ GeV and $\lvert\eta\rvert < 2.5$
L1_DoubleIsoTau32er2p1	Double isolated τ with $E_T > 32$ GeV and $\lvert\eta\rvert < 2.1$
L1_SingleMu22	Single muon with $p_T > 22$ GeV
L1_DoubleEG_25_12_er2p5	Double e/γ with $E_T > 25$ GeV, 12 GeV and $\lvert\eta\rvert < 2.5$
L1_DoubleMu_15_7	Double muon with $p_T > 15$ GeV, 7 GeV
L1_ETMHF100	$E_T^{miss} > 100$ GeV
L1_SingleJet180	Single jet with $E_T > 180$ GeV
L1_DoubleJet150er2p5	Double jet with $E_T > 150$ GeV and $\lvert\eta\rvert < 2.5$

in a time interval of a "luminosity section", corresponding to 2^{18} LHC orbits or 23.3 seconds of data taking. In this and subsequent figures, error bands in the data points represent their statistical uncertainty only. Single-object trigger rates generally increase linearly with pileup, whereas double-object paths may have a higher-order dependency. The largest dependence on pileup is shown by the seeds based on the missing transverse energy. The Level-1 trigger reconstruction cannot distinguish between objects generated by different collisions within the same bunch crossing. However, in offline reconstruction the objects are associated with different reconstructed vertices that originate from different collisions. This requires tracking information, which is not available in the Level-1 trigger.

The rate of an algorithm can be reduced by applying a "prescale" that determines what fraction of events selected by the seed will pass the trigger. A prescale of N means that only one in every N events satisfying the condition is accepted. Prescale values can only be positive integer numbers.

2020 JINST 15 P10017

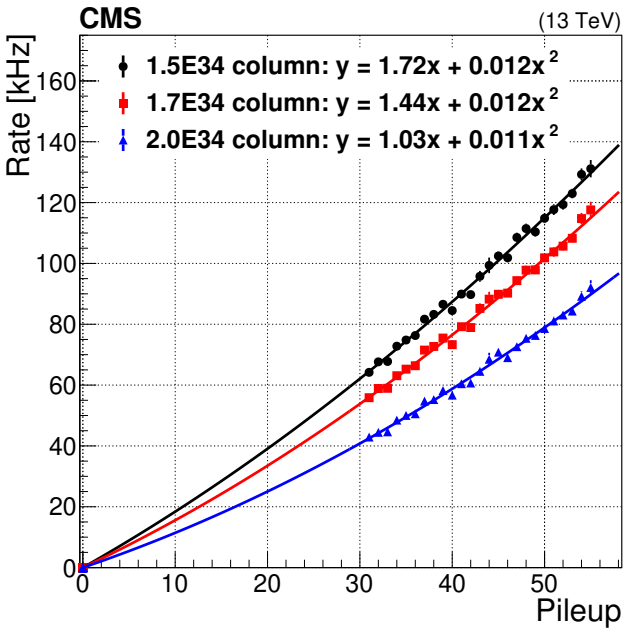


Figure 3. Total Level-1 menu rates as a function of pileup for three sets of algorithms, or "prescale columns", defined in the text. The rates were recorded during a LHC fill with 2544 proton bunches. The instantaneous luminosities of 2.0×, 1.7×, and 1.5×10^{34} cm^{-2} s^{-1} correspond to an average pileup of 55, 47, and 42 respectively. The curves represent fits to the data points that are quadratic and constrained to pass through the origin.

With a prescale of two, for example, only half of the events selected by the seed will propagate to the HLT. A "prescale column" is a set of prescale values applied to each of the seeds in a particular menu. During an LHC fill the beam intensity decreases with time, so multiple prescale columns with decreasing prescale values are used, to maximize signal efficiency while keeping the rate under 100 kHz.

Trigger algorithms used for most physics analyses have a prescale value of one in all columns, whereas high rate calibration triggers generally have prescale values that are greater than one. Figure 3 shows the trigger rate as a function of pileup, defined as for figure 2, for a few benchmark prescale columns of the trigger menu. These were tuned to reach a total Level-1 trigger rate of 100 kHz for three different target instantaneous luminosity values. The prescale columns for luminosities of 1.5×10^{34} cm^{-2} s^{-1} and 1.7×10^{34} cm^{-2} s^{-1}, represented by the black dots and red squares, respectively, were not used to collect data at the highest pileup, but were activated only when their corresponding Level-1 trigger rate was lower than 100 kHz. Although quadratic functions fit the data points well, the very small quadratic coefficient of these fits indicates a mostly linear dependence of the rate on pileup suggesting a negligible contamination from pileup events.

The total number of algorithms in the CMS Level-1 menu used in proton-proton collisions is between 350 and 400; the system architecture is limited to 512, which is a factor 4 larger than the Run 1 system. There were about 150 unprescaled seeds in the menu at the end of 2018, of which approximately 100 were "contingency" seeds with stricter selection requirements. The remaining 50 were responsible for collecting data for all physics analyses that used the full

2020 JINST 15 P10017

integrated luminosity delivered by the LHC. The other 250 algorithms were prescaled and used for calibrations, monitoring, trigger efficiency measurements, and other ancillary measurements. Tables 2 and 3 show the unprescaled algorithms and their corresponding thresholds. Algorithms with no p_T threshold for muons have an effective minimum p_T that varies as a function of $|\eta|$, because very low-p_T muons do not reach the muon chambers.

5 The Level-1 trigger architecture

During the first LHC long shutdown and extending into 2015, the new CMS Level-1 trigger was installed to run in parallel with the Run 1 (legacy) Level-1 trigger, and eventually replaced it. The upgraded Level-1 trigger is described in detail in ref. [3], with the exception of two new muon systems: the concentrator and preprocessor fanout (CPPF) and the TwinMux, which are described in section 6. Section 5 summarizes the overall design of the upgraded trigger, shown in figure 4.

In contrast to the Run 1 system that used the Versa Module Eurocard (VME) standard and many parallel electrical cables for the interconnects, the upgraded trigger uses Advanced Mezzanine Cards (AMC) based on MicroTCA technology [12] and multi-Gb/s serial optical links for data transfer between modules. The MicroTCA crate provides a high-bandwidth backplane, system monitoring capabilities, and redundant power modules. The number of distinct electronics board types is greatly reduced because many components are based on common hardware designs.

The calorimeter trigger consists of two layers: Layer-1 receives, calibrates, and sorts the local energy deposits ("trigger primitives") which are sent to the trigger by the ECAL and HCAL; Layer-2 uses these calibrated trigger primitives to reconstruct and calibrate the physics objects such as electrons, tau leptons, jets, and energy sums. The calorimeter trigger follows a time-multiplexed trigger design [13] illustrated in figure 5. Each main processing node has access to a whole event with a granularity of $\Delta\eta\times\Delta\phi$ of 0.087×0.087 radians (where phi is azimuthal angle) in most of the calorimeter acceptance (a slightly coarser granularity is used at high $|\eta|$). A demultiplexer (DeMux) board then reorders, reserializes, and formats the events for the global trigger (μGT, which is pronounced micro-GT to emphasize the connection to the MicroTCA technology used in this upgrade) processing. Because the volume of incoming data and the algorithm latency are fixed, the position of all data within the system is fully deterministic and no complex scheduling mechanism is required. The benefits of time multiplexing include removal of regional boundaries for the object reconstruction and full granularity when computing energy sums. The multiplicity of processing nodes provides the flexibility to add nodes as required by complex trigger algorithms. These algorithms are fully pipelined and start processing as soon as the minimum amount of data is received.

The muon trigger system includes three muon track finders (MTF) which reconstruct muons in the barrel (BMTF), overlap (OMTF), and endcap (EMTF) regions of the detector, and the global muon trigger (μGMT, pronounced micro-GMT) for final muon selection. The μGT finally collects muons and calorimeter objects and executes every algorithm in the menu in parallel for the final trigger decision.

2020 JINST 15 P10017

Table 2. List of the most used unprescaled Level-1 trigger algorithms (seeds) during Run 2 and their requirements.

Algorithm	Requirements (p_T, E_T, $m_{\mu\mu}$, and m_{jj} in GeV)
Muons	
Single μ	$p_T > 22$ & Tight quality
Double μ	$p_T > 15, 7$ & Medium quality
Double μ	$p_T > 15, 5$ & Tight quality
Double μ	$p_T > 8, 8$ & Tight quality
Double μ + mass	$p_T > 4.5$ & $\|\eta\| < 2.0$ & Tight quality & OS & $m_{\mu\mu} > 7$
Double μ + ΔR	$p_T > 4$ & Tight quality & OS & $\Delta R < 1.2$
Double μ + ΔR	$p_T > 0$ & $\|\eta\| < 1.5$ & Tight quality & OS & $\Delta R < 1.4$
Double μ + BX	$p_T > 0$ & $\|\eta\| < 1.4$ & Medium quality & Non-colliding BX
Triple μ	$p_T > 5, 3, 3$ & Medium quality
Triple μ	$p_T > 3, 3, 3$ & Tight quality
Triple μ + mass	$p_T > 5, 3.5, 2.5$ & Med. qual.; two μ OS & $p_T > 5, 2.5$ & $5 < m_{\mu\mu} < 17$
Triple μ + mass	Three μ any qual.; two μ & $p_T > 5, 3$ & Tight qual. & OS & $m_{\mu\mu} < 9$
Electrons / photons	(e/γ)
Single e/γ	$p_T > 60$
Single e/γ	$p_T > 36$ & $\|\eta\| < 2.5$
Single e/γ	$p_T > 28$ & $\|\eta\| < 2.5$ & Loose isolation
Double e/γ	$p_T > 25, 12$ & $\|\eta\| < 2.5$
Double e/γ	$p_T > 22, 12$ & $\|\eta\| < 2.5$ & Loose isolation
Triple e/γ	$p_T > 18, 17, 8$ & $\|\eta\| < 2.5$
Triple e/γ	$p_T > 16, 16, 16$ & $\|\eta\| < 2.5$
Tau leptons (τ)	
Single τ	$p_T > 120$ & $\|\eta\| < 2.1$
Double τ	$p_T > 32$ & $\|\eta\| < 2.1$ & Isolation
Jets	
Single jet	$p_T > 180$
Single jet + BX	$p_T > 43$ & $\|\eta\| < 2.5$ & Non-colliding BX
Double jet	$p_T > 150$ & $\|\eta\| < 2.5$
Double jet + $\Delta\eta$	$p_T > 112$ & $\|\eta\| < 2.3$ & $\Delta\eta < 1.6$
Double jet + mass	$p_T > 110, 35$; two jets $p_T > 35$ & $m_{jj} > 620$
Double jet + mass	$p_T > 30$ & $\|\eta\| < 2.5$ & $\Delta\eta < 1.5$ & $m_{jj} > 300$
Triple jet	$p_T > 95, 75, 65$; two jets $p_T > 75, 65$ & $\|\eta\| < 2.5$
Energy sums	
E_T^{miss}	$E_T^{miss} > 100$ (Vector sum of p_T of calorimeter deposits with $\|\eta\| < 5.0$)
H_T	$H_T > 360$ (Scalar sum of p_T of all jets with $p_T > 30$ and $\|\eta\| < 2.5$)
E_T	$E_T > 2000$ (Scalar sum of p_T of calorimeter deposits with $\|\eta\| < 5.0$)

Terms used

Tight quality: muons with hits in at least 3 different muon stations.

Medium quality: muons with hits in at least 2 different muon stations.

The "non-colliding BX" requirement selects beam-empty events.

$\Delta R \equiv ((\Delta\phi)^2 + (\Delta\eta)^2)^{1/2}$, and phi is the azimuthal angle in radians.

OS: Opposite Sign (of electric charge).

E_T: scalar sum of p_T of calorimeter deposits.

H_T: scalar sum of p_T of jets.

Isolation and loose isolation: the isolation requires an upper limit on the transverse calorimeter energy surrounding the candidate. The limit depends on the pileup, the Level-1 candidate E_T and $|\eta|$. Details are given in sections 7.2 and 7.3.

2020 JINST 15 P10017

Table 3. List of the most used cross object unprescaled Level-1 trigger algorithms (seeds) during Run 2 and their corresponding requirements.

Algorithm	Requirements (p_T, E_T, $m_{\mu\mu}$, and m_{jj} in GeV)
Two objects	
Single μ + Single e/γ	$p_T(\mu) > 20$ & Tight quality(μ) & $p_T(e/\gamma) > 10$ & $\lvert\eta(e/\gamma)\rvert < 2.5$
Single μ + Single e/γ	$p_T(\mu) > 7$ & Tight quality(μ) & $p_T(e/\gamma) > 20$ & $\lvert\eta(e/\gamma)\rvert < 2.5$
Single μ + Single τ	$p_T(\mu) > 18$ & $\lvert\eta(\mu)\rvert < 2.1$ & Tight quality(μ) & $p_T(\tau) > 24$ & $\lvert\eta(\tau)\rvert < 2.1$
Single μ + H_T	$p_T(\mu) > 6$ & Tight quality(μ) & $H_T > 240$
Single e/γ + Single τ	$p_T(e/\gamma) > 22$ & $\lvert\eta(e/\gamma)\rvert < 2.1$ & Loose isolation(e/γ) & $p_T(\tau) > 26$ & $\lvert\eta(\tau)\rvert < 2.1$ & Isolation(τ) & $\Delta R > 0.3$
Single e/γ + Single jet	$p_T(e/\gamma) > 28$ & $\lvert\eta(e/\gamma)\rvert < 2.1$ & Loose isolation(e/γ) & $p_T(\text{jet}) > 34$ & $\lvert\eta(\text{jet})\rvert < 2.5$ & $\Delta R > 0.3$
Single e/γ + H_T	$p_T(e/\gamma) > 26$ & $\lvert\eta(e/\gamma)\rvert < 2.1$ & Loose isolation(e/γ) & $H_T > 100$
Single τ + E_T^{miss}	$p_T(\tau) > 40$ & $\lvert\eta(\tau)\rvert < 2.1$ & $E_T^{miss} > 90$
Single jet + E_T^{miss}	$p_T(\text{jet}) > 140$ & $\lvert\eta(\text{jet})\rvert < 2.5$ & $E_T^{miss} > 80$
Three objects	
Single μ + Double jet + ΔR	$p_T(\mu) > 12$ & $\lvert\eta(\mu)\rvert < 2.3$ & Tight quality(μ) & $p_T(\text{jet}) > 40$ & $\Delta\eta(\text{jet,jet}) < 1.6$ & $\lvert\eta(\text{jet})\rvert < 2.3$ & $\Delta R(\mu,\text{jet}) < 0.4$
Single μ + Single jet + E_T^{miss}	$p_T(\mu) > 3$ & $\lvert\eta(\mu)\rvert < 1.5$ & Tight quality (μ) & $p_T(\text{jet}) > 100$ & $\lvert\eta(\text{jet})\rvert < 2.5$ & $E_T^{miss} > 40$
Double μ + H_T	$p_T(\mu) > 3$ & Tight quality(μ) & $H_T > 220$
Double μ + Single jet + ΔR	$p_T(\mu) > 0$ & Medium quality(μ) & $\Delta R(\mu,\mu) < 1.6$ & $p_T(\text{jet}) > 90$ & $\lvert\eta(\text{jet})\rvert < 2.5$ & $\Delta R(\mu,\text{jet}) < 0.8$
Double μ + Single e/γ	$p_T(\mu) > 5$ & Tight quality(μ) & $p_T(e/\gamma) > 9$ & $\lvert\eta(e/\gamma)\rvert < 2.5$
Double e/γ + Single μ	$p_T(e/\gamma) > 12$ & $\lvert\eta(e/\gamma)\rvert < 2.5$ & $p_T(\mu) > 6$ & Tight quality(μ)
Double e/γ + H_T	$p_T(e/\gamma) > 8$ & $\lvert\eta(e/\gamma)\rvert < 2.5$ & $H_T > 300$
Four objects	
Double μ + Double e/γ	$p_T(\mu) > 3$ & Medium quality(μ) & OS(μ) & $p_T(e/\gamma) > 7.5$
Double μ + Double e/γ	$p_T(\mu) > 5$ & Medium quality(μ) & OS(μ) & $p_T(e/\gamma) > 3$
Five objects	
Double μ + E_T^{miss} + Single jet OR Double jet	$p_T(\mu) > 3$ & Tight quality(μ) & $E_T^{miss} > 50$ & ($p_T(\text{jet}) > 60$ & $\lvert\eta(\text{jet})\rvert < 2.5$) OR ($p_T(\text{jet}) > 40$ & $\lvert\eta(\text{jet})\rvert < 2.5$)
H_T + Quad jet	$H_T > 320$ & $p_T(\text{jet}) > 70, 55, 40, 40$ & $\lvert\eta(\text{jet})\rvert < 2.4$

2020 JINST 15 P10017

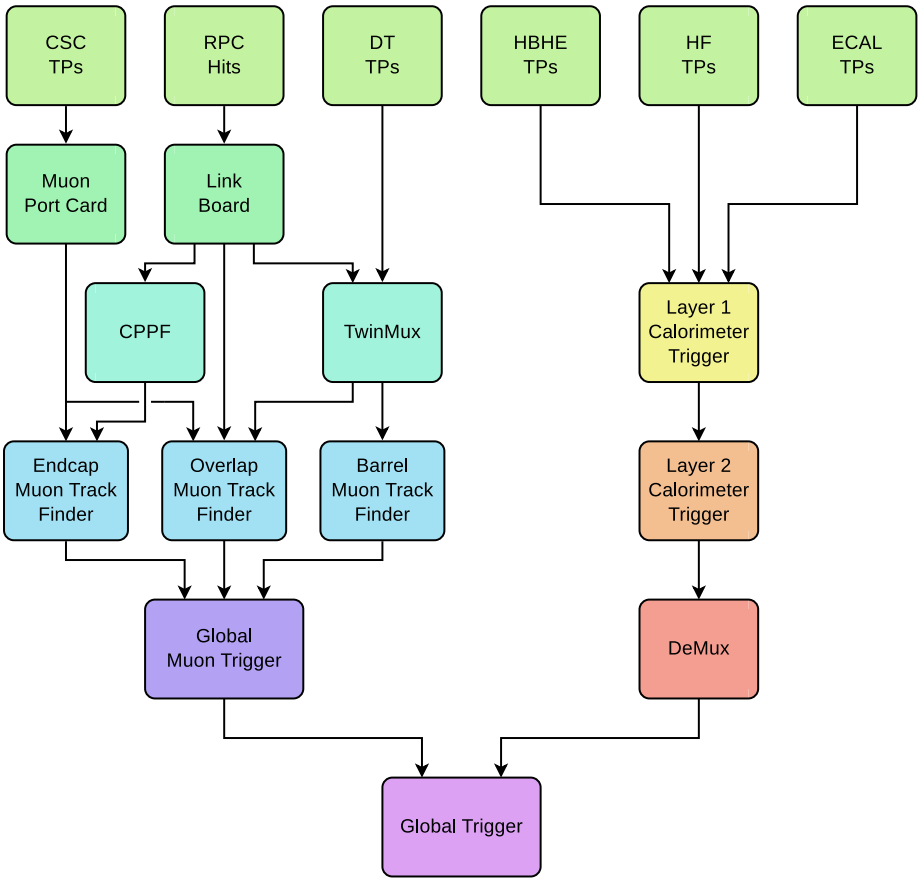


Figure 4. Diagram of the upgraded CMS Level-1 trigger system during Run 2. More details about the muon and calorimeter trigger systems in section 6 and 7 respectively. Labels in the diagram correspond to trigger primitives (TPs), cathode strip chambers (CSC), drift tubes (DT), resistive plate chambers (RPC), concentration preprocessing and fan-out (CPPF), hadron calorimeter barrel (HB) and endcap (HE), hadron calorimeter forward (HF), electromagnetic calorimeter (ECAL), demultiplexing card (DeMux).

In the upgraded trigger, the BMTF, μGMT, μGT, and Layer-2 use the same type of processor card. The OMTF and EMTF electronic boards similarly share a common design, whereas Layer-1, TwinMux, and CPPF each use a different design. All processor cards, however, use a Xilinx Virtex-7 Field Programmable Gate Array (FPGA). Thus many firmware and control software components, e.g., data readout and link monitoring, can be reused by several systems, reducing the workload for development and maintenance.

An advanced mezzanine card called the AMC13 [14] provides fast control signals from the trigger control and distribution system to the trigger AMCs over the MicroTCA backplane. If an event is selected, the trigger AMCs send their data over the backplane to the AMC13, which also connects to the central CMS data acquisition system via 10 Gb/s optical links. More details on the hardware can be found in ref. [3].

2020 JINST 15 P10017

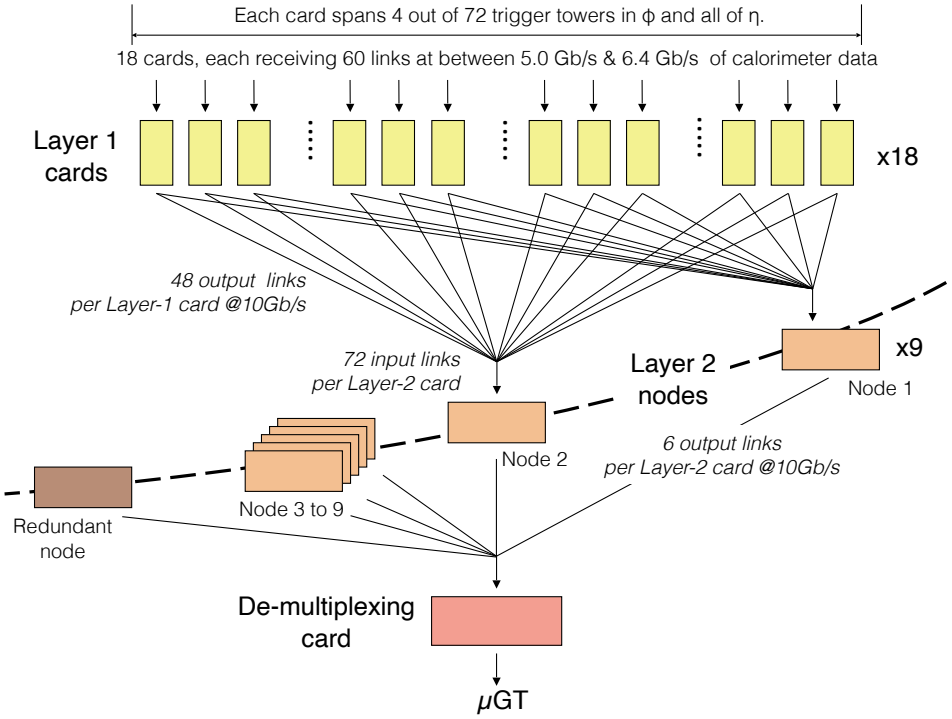


Figure 5. The time-multiplexed trigger architecture of the upgraded CMS calorimeter trigger.

6 The Level-1 muon trigger and its performance

The CMS muon detector is composed of three partially overlapping subdetectors (CSCs, DTs, and RPCs, as described in section 2), whose signals are combined together into "trigger primitives" (TPs) to reconstruct muons and measure their p_{T}. Trigger primitives provide coordinates, timing, and quality information from detector hits. Figure 6 shows the geometrical arrangement of the three muon subdetectors in a quadrant of the CMS detector.

In the legacy trigger, data from each of the three subdetectors were used separately to build independent muon tracks, which were combined by a global muon trigger. The upgraded Level-1 trigger combines information from all available subdetectors to reconstruct tracks in three distinct pseudorapidity regions, improving the muon reconstruction efficiency and resolution while reducing the misidentification rate.

The BMTF takes inputs from DT and RPC chambers in the barrel; all three muon subsystems contribute to the OMTF tracks in the overlap between barrel and endcap; and the EMTF uses CSC and RPC information to reconstruct endcap muons. Detector symmetry allows each track finder to run the same algorithm in parallel for different regions in ϕ. The BMTF is segmented in twelve sectors of 30° each, and both the OMTF and EMTF are segmented into 12 sectors of 60°, six on each end of the experiment. A single board builds tracks in one sector, plus 20–30° of overlap to account for muon bending in ϕ.

2020 JINST 15 P10017

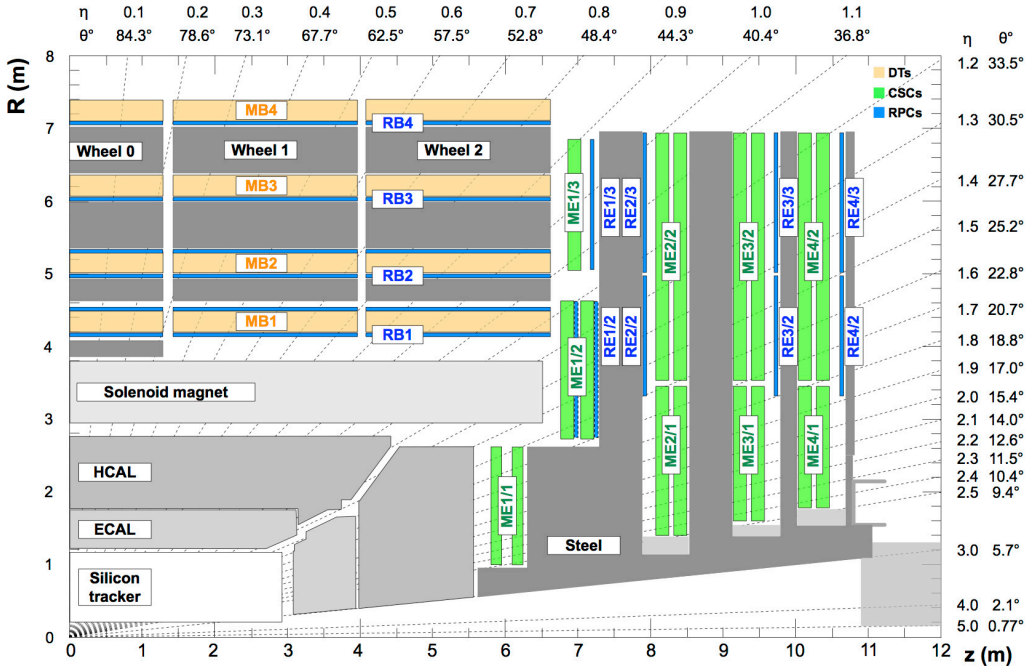


Figure 6. An R-z slice of a quadrant of the CMS detector [15]. The origin of the axes represents the interaction point. The proton beams travel along the z-axis and cross at the interaction point. The three CMS muon subdetectors are shown: four stations of DTs in yellow, labelled MB; four stations of CSCs in green, labelled ME; and four stations of RPCs in blue, labelled RB or RE.

The track finders use muon detector TPs to build muon track candidates, assign a quality to each, and measure the charge and the p_{T} of each candidate from the bending in the fringe field of the magnet yoke. Each track finder uses muon finding and p_{T} assignment logic optimized for its region, and assigns the track quality corresponding to the estimated p_{T} resolution.

Each track finder transmits up to 36 muons to the μGMT, which resolves duplicates from different boards, and sends the data for a maximum of eight muons of highest rank (a linear combination of p_{T} and a quality value) to the μGT, where they are used in the final Level-1 trigger decision.

6.1 Barrel muon trigger primitives

The DT and RPC barrel systems consist of four cylindrical stations wrapped around the solenoid, each split into 12 wedges in ϕ and 5 wheels along the beam direction. In the upgraded Level-1 trigger, a new layer called the TwinMux merges DT trigger primitives and RPC hits from the same station (i.e., detector layer) into "superprimitives". Superprimitives combine the better spatial resolution of the DT and the more precise timing from the RPC. Each superprimitive is assigned a quality, which depends on the location of its inputs, η and ϕ coordinates, and an internal bending angle ϕ_{b}. The TwinMux then sends superprimitives to the BMTF. The TwinMux also transmits unmerged DT TPs and RPC hits to the OMTF. In both cases the TwinMux increases the bandwidth of the data links used to transmit TPs, thus reducing the number of data links. Merging DT and

2020 JINST 15 P10017

RPC hits also improves the TP efficiency and timing in each station, which results in improved BMTF performance. The TwinMux is described in detail in ref. [16].

6.2 Endcap RPC trigger primitives

The CPPF consists of eight MicroTCA boards with FPGA processors, designed to concentrate endcap RPC TPs for transmission onto higher-bandwidth optical links. The CPPF clusters RPC hits in adjacent strips into a single TP, and computes their θ and ϕ coordinates before transmitting up to two clusters per 10° chamber to the EMTF. The CPPF was commissioned in 2017. A detailed description is given in ref. [17].

6.3 Barrel muon track finder

The BMTF reconstructs muons in the barrel region ($|\eta| < 0.83$). The BMTF track finding and p_{T} assignment algorithms are similar to their predecessors running on the DTTF [2, 18]. Look-up tables (LUTs) use the bending angle and the quality of the superprimitives of an inner station to form an acceptance window for the outer station through an extrapolation unit. Each extrapolation unit receives superprimitives from one thirty-degree sector/wheel and its five neighbors, i.e. the two adjacent sectors in the same wheel and the corresponding three in the neighboring wheel. The track assembler unit receives the paired superprimitives for all stations and combines them. Tracks with more stations, especially inner stations where the magnetic field is stronger, are assigned higher quality.

The assignment unit uses LUTs to assign p_{T}, ϕ, and η of a track. The p_{T} value is assigned based on the difference of the ϕ coordinates of TPs in neighboring stations, $\Delta\phi$, for the majority of tracks. However, $\Delta\phi$ by itself cannot distinguish high- and low-p_{T} tracks because of the inversion of their curvature due to the inversion of the magnetic field direction in the yoke with respect to the inner solenoid region. For this reason two LUTs encode the p_{T} value for either the high- or low-p_{T} case, and the internal bending angle of the superprimitive, ϕ_{b}, is used to select the appropriate result. A LUT based purely on the bending angle ϕ_{b} augments the p_{T} assignment for tracks reconstructed from only two superprimitives, where at least one of the TPs is assigned good quality by the TwinMux. The p_{T} assigned by this LUT is compared to the one obtained using the TP $\Delta\phi$ and the smaller value is selected.

6.4 Overlap muon track finder

The OMTF receives data from three DT and five RPC stations in the barrel, plus four CSC and three RPC stations in the endcap, giving 18 total "layers" that are used to build tracks (since each DT station has two layers). Track reconstruction occurs independently in each sector in ϕ. The OMTF uses detector hits directly from the RPC system and trigger primitives from the DT and CSC systems. In the following section the word "hits" is used to indicate either. Each track is constructed starting from a single reference hit in one layer, so the first step is to select up to four reference hits, favoring hits from inner layers and those with good ϕ resolution. Up to two reference hits may come from the same layer, enabling efficient reconstruction of nearby muons.

The algorithm uses patterns generated from simulated events to associate hits in other layers with the reference hit. For each muon charge there are twenty-six patterns corresponding to different p_{T} ranges, from 2 to 140 GeV. Each pattern encapsulates information about the average muon track

2020 JINST 15 P10017

propagation between layers and the probability density function of hit spread in ϕ in each layer, with respect to the reference hit. The patterns differ depending on the reference layers used. When multiple patterns match a given hit, a statistical estimator based on the ϕ distribution of the hits resolves the ambiguity, preferring patterns with a larger number of matched layers. The OMTF reconstruction algorithm can be regarded as a naive Bayes classifier.

Properties of the best matched patterns, together with the reference hit ϕ, are passed to the internal muon sorter, which removes possible duplicates from a single muon producing multiple reference hits. The three best muons per board are transmitted to the μGMT, giving a maximum of 36 muons. A more detailed description of the algorithm is found in ref. [19].

6.5 Endcap muon track finder

The EMTF builds muon tracks from CSC and RPC TPs in the endcap. Both detectors are composed of four stations separated in z and covering 360° in ϕ. The CSCs have complete four-station coverage in the pseudorapidity range $1.2 < |\eta| < 2.4$ in two or three concentric rings of detectors per station, whereas the endcap RPCs cover approximately $1.2 < |\eta| < 1.7$ in two rings of detectors per station. The CSCs deliver up to two local charged tracks per BX from each 10° or 20° chamber in each station and ring, with $\approx 1/16^\circ$ precision in ϕ and $\approx 1/4^\circ$ precision in θ. The RPCs send hits from chambers with similar geometry, which are clustered by the CPPF into TPs with $\approx 1/4^\circ$ precision in ϕ and $\approx 1^\circ$ precision in θ.

The EMTF builds tracks using at most one TP (CSC or RPC) per station. The algorithm first looks for CSC TPs correlated in ϕ in multiple stations consistent with the presence of a muon track, matching at least one of the five predefined patterns. The pattern recognition runs in parallel in four zones in θ. After the patterns are found, the CSC or RPC TP in each station closest to the pattern is taken for further processing. Resulting tracks are ranked according to their straightness and the number of stations with hits. Stations 1 and 2 are prioritized because the magnetic field is much stronger between stations 1 and 2 than beyond station 2. A muon track with TPs in these two stations therefore has a more precise p_T assignment. The three hit patterns with highest quality from each sector are kept for the p_T assignment, and the others are discarded.

The bending angles in ϕ and θ of the muon track are used to calculate the track p_T. However, this relationship is complicated by several factors. At low p_T, muons can experience significant multiple scattering and energy loss and at high p_T, they can initiate electromagnetic showers. In addition, the CMS magnetic field strength and direction varies with η outside the solenoid, so muons of similar momenta can have different behavior in the more central region ($|\eta| < 1.55$) than in the more forward region ($|\eta| > 2.1$). The complicated dependencies make this an ideal case for machine learning. A boosted decision tree (BDT) regression technique is used to provide an estimate of the track p_T, taking these dependencies into account. The BDT input variables are compressed into 30 bits, and training parameters are optimized using MC simulation of single-muon events. The BDT output values are pre-evaluated and stored in a LUT loaded in a $\approx$1 GB memory module of the EMTF for fast determination. Additional details about the design, training, and implementation of the BDT can be found in ref. [20].

2020 JINST 15 P10017

6.6 Global muon trigger

The μGMT receives up to 108 muon candidates (3 per sector) sent from the three muon track finders. The μGMT sorts the muons and identifies and removes duplicates, sending up to eight muons to the μGT. Such duplicate muons would significantly increase the trigger rate for multimuon trigger algorithms and must be removed while keeping a high efficiency for events with two genuine muons. In parallel to the duplicate removal and sorting stage, the μGMT also corrects the spatial coordinates of each muon by extrapolating the track from the muon stations back to the interaction region.

The μGMT uses the p_{T} and the quality of input muons to define an initial ranking, separately sorting muons from the positive and negative η sides of the OMTF and EMTF, as well as from the BMTF. It keeps the four highest ranked muons coming from each endcap of the OMTF and EMTF, along with the highest ranked eight BMTF muons. The second sorting stage compares the ranks of muons coming from the first stage and selects the eight with the highest rank.

Because of the overlap between adjacent wedges or sectors of the track finders (TFs), a muon traversing the detector in these overlap regions can be found by the TF processors of both sides on the overlap. In addition to this overlap in ϕ, the different regional TFs also have an overlap in η where a muon can be found by both the BMTF and OMTF, or by the OMTF and EMTF. Two different methods are used for the identification of duplicates. The first method makes use of the "track address" of the muon, which encodes the TPs used to build the muon track, to find duplicates between BMTF wedges. The second method uses the muon track coordinates, which are applied to find duplicates between adjacent sectors in the OMTF and the EMTF, and between different regional TFs. For the second method, simulated events are used to determine the optimal size and shape of the regions in which tracks should be marked as duplicates.

Because the TF systems measure the muon coordinates within the muon systems, the μGMT extrapolates all input muon track parameters back to the collision point. The extrapolation corrections are derived from MC simulation as a function of p_{T}, ϕ, η, and charge of the muon, and are stored in a LUT. The corrections have a coarse granularity since they are limited to 4 bits: they have steps of 0.05 radians in $\Delta\phi$ and 0.01 in $\Delta\eta$ and are applied to muons with $p_{\mathrm{T}} < 64\,\mathrm{GeV}$. These corrected coordinates are then propagated to the μGT to improve the performance of trigger algorithms relying on the invariant mass or difference in spatial coordinates between multiple muons.

The μGMT also transmits the track quality to the μGT as a selection option for specific trigger paths. Quality is also used for cancellation in case duplicates are found. Muons passing the "tight" quality criteria have good p_{T} resolution, and are used in single-muon seeds. All BMTF tracks pass the tight criteria, thanks to the strong magnetic bending effect in the barrel region, whereas OMTF and EMTF tracks must have TPs in at least three layers, and in EMTF one of those TPs must be in the innermost layer. The "medium" and "loose" criteria are used in OMTF and EMTF to increase the trigger efficiency for events with multiple muon tracks by including tracks with fewer TPs, or without a TP in the first layer.

6.7 Performance

The data recorded since the start of Run 2 are used to study the performance of the upgraded muon trigger. The performance studies presented in this section use data collected during 2018. Data collected during 2016 and 2017 give similar results. Figure 7 shows the correlation between the

2020 JINST 15 P10017

inverse of the muon p_T assigned at Level-1, proportional to the track curvature, and the inverse of the offline reconstructed muon p_T for the three η regions of interest. The correlation is linear but slightly off-diagonal, because Level-1 muon p_T values are scaled up to provide 90% efficiency for any given trigger p_T threshold. The resolution in the barrel shows better resolution because the orientation of the magnetic field with respect to the muon track causes less bending in the forward regions. The figure uses a data set triggered by a single isolated muon, with two oppositely charged muons consistent with a Z boson decay.

The efficiency measurements use a tag-and-probe [21] technique with offline reconstructed muons from preselected Drell-Yan events. The tag muon is reconstructed with the CMS particle-flow algorithm [22], and it is required to have $p_T > 26\,\text{GeV}$ and be isolated such that nearby calorimeter energy deposits must sum to less than 15% of the muon p_T. The tag muon must match within a cone of $\Delta R = \sqrt{(\Delta\eta)^2 + (\Delta\phi)^2} < 0.1$ to a muon reconstructed by the single isolated muon HLT algorithm with $p_T > 24\,\text{GeV}$. The HLT muon must be seeded by the single-muon Level-1 trigger with a p_T threshold of 22 GeV.

The numerator of the efficiency measurement includes events where a Level-1 muon from the triggering bunch crossing matches a probe muon, reconstructed using the particle-flow information, within $\Delta R < 0.2$. The denominator includes all events with a tag muon. The tag and the probe muons must be separated by $\Delta R > 0.4$. This guarantees that the tag and the probe are two different muons. Figure 8 shows trigger efficiencies measured for a single-muon trigger with a p_T threshold of 22 GeV as a function of the offline reconstructed muon p_T. At the threshold value the efficiency reaches about 86% of the plateau, which is measured to be ≈93%. A more detailed description of the trigger performance at high muon p_T, where radiative showering complicates the reconstruction, is given in ref. [23]. Figure 9 shows the efficiency as a function of the reconstructed p_T of the probe muon, p_T^{offline}, for the three track finder regions (left), and as a function of η (right). The three track finders reach an efficiency plateau over 90% for the same p_T^{reco} value, with the barrel track finder exhibiting the sharpest turn-on curve. Figure 10 includes efficiency measurements for different quality thresholds versus muon p_T and η. The detector geometry is responsible for the reduction of trigger efficiency in certain η regions. Figure 11 shows the efficiency in different $|\eta|$ regions as a function of the number of pileup vertices and muon ϕ. In events with high pileup, extra tracks can confuse the endcap muon reconstruction, causing the trigger efficiency to drop by a few % in the far forward region.

In comparison to the legacy trigger system, the efficiency from the upgraded muon trigger is similar or higher, depending on the η region, as seen in figure 12. Figure 13 overlays the re-emulated Run 1 (legacy) single-muon algorithm rates and Run 2 (upgrade) rates as a function of Level-1 muon p_T (left) and η (right). The muon trigger rate was studied with an unbiased Run 2 data sample taken with a prescaled trigger that only required colliding bunches for triggering. For the single-muon trigger with a 22 GeV threshold, the rate is approximately a factor of 2 lower than for the legacy trigger system, estimated from studies with simulated events. The rate reduction improves at higher trigger thresholds, giving flexibility for tuning in higher instantaneous luminosity conditions. The use of more sophisticated p_T assignment algorithms, also exploiting multivariate analysis tools allowed by the more powerful trigger firmware and hardware, result in a significant rate reduction compared to the legacy system.

2020 JINST 15 P10017

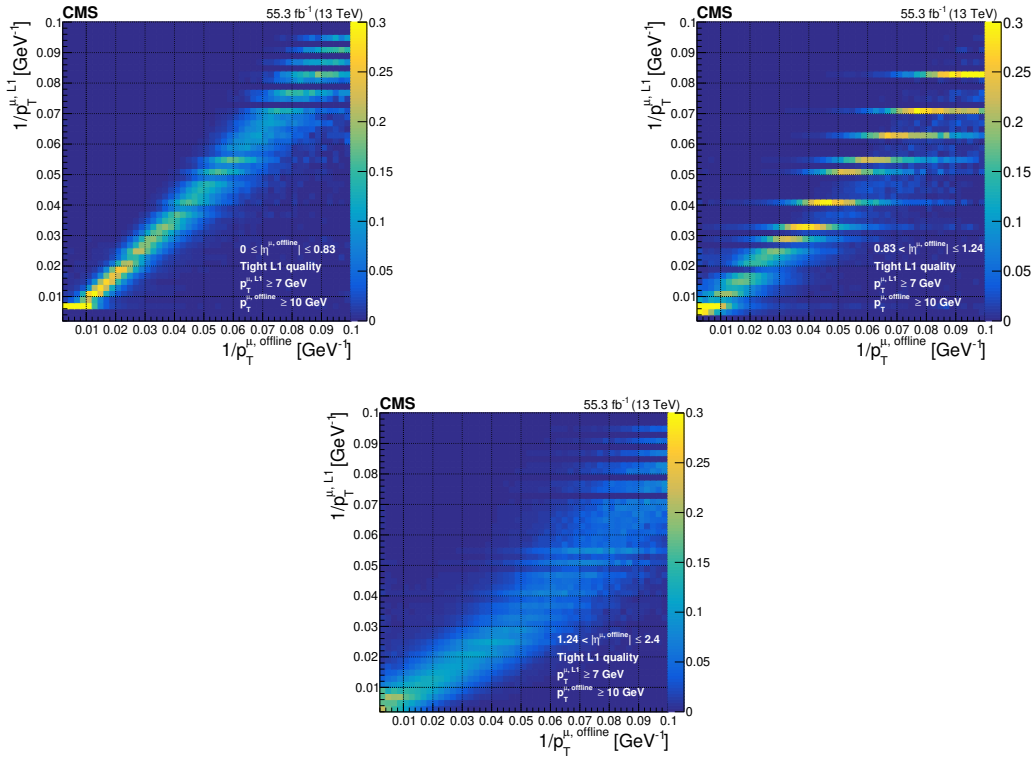


Figure 7. Correlation between $1/p_{\mathrm{T}}$ of the muon (proportional to curvature) as assigned at Level-1 vs. offline for three $|\eta|$ regions: barrel (top left), overlap (top right), and endcap (bottom). The measurements come from a data set enriched with events with a Z boson. Distinct bands in the overlap region come from more discrete p_{T} assignment with the OMTF patterns.

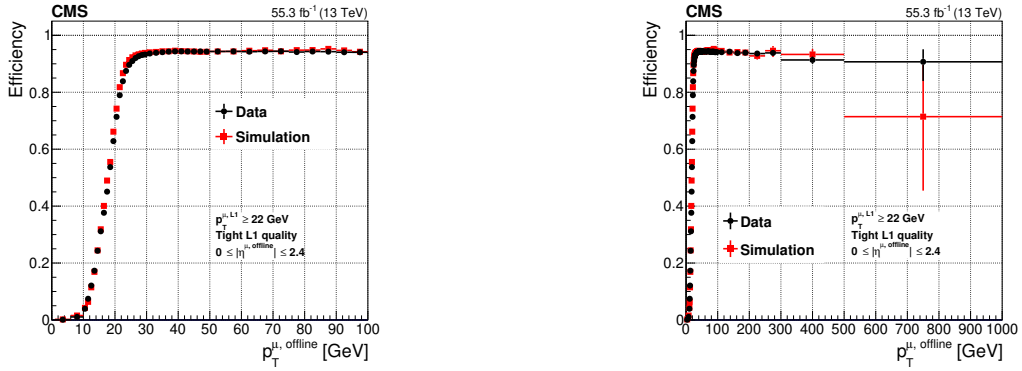


Figure 8. Level-1 trigger efficiency, for data and simulation as a function of $p_{\mathrm{T}}^{\mathrm{offline}}$, for all reconstructed muons in the CMS acceptance ($|\eta^{\mathrm{offline}}| < 2.4$) for the most commonly used single-muon trigger during Run 2 ($p_{\mathrm{T}}^{\mathrm{L1}} > 22\,\mathrm{GeV}$), measured with the tag-and-probe method described in the text with the full 2018 data set. The left plot focuses on the steep increase part of the curve close to the trigger threshold. The right plot shows the full momentum range up to 1 TeV. The simulation reproduces the data within a few percent accuracy. The Level-1 trigger efficiency plateau is stable as a function of the muon transverse momentum, retaining a high triggering efficiency for muon $p_{\mathrm{T}}^{\mathrm{offline}} \leq 1$ TeV.

2020 JINST 15 P10017

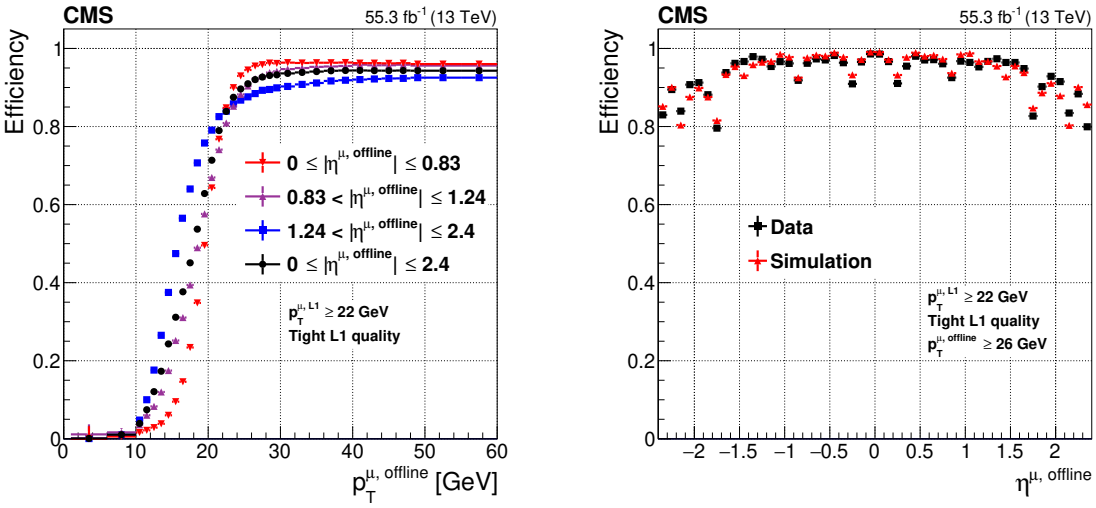


Figure 9. The left plot shows the Level-1 muon trigger efficiency for data as a function of the offline reconstructed muon $p_{\mathrm{T}}^{\mathrm{offline}}$ for each η region: barrel region in red, overlap region in purple, endcap region in blue, and the total in black. Turn-on curves for more central muons rise faster primarily because of improved momentum resolution from increased bending in the magnetic field of the yoke. The right plot shows the Level-1 muon efficiency for data and simulation as a function of the offline reconstructed muon η. The modulation of the efficiency in η is because of the acceptance of the muon systems. The efficiency is measured with the tag-and-probe method described in the text with the full 2018 data set.

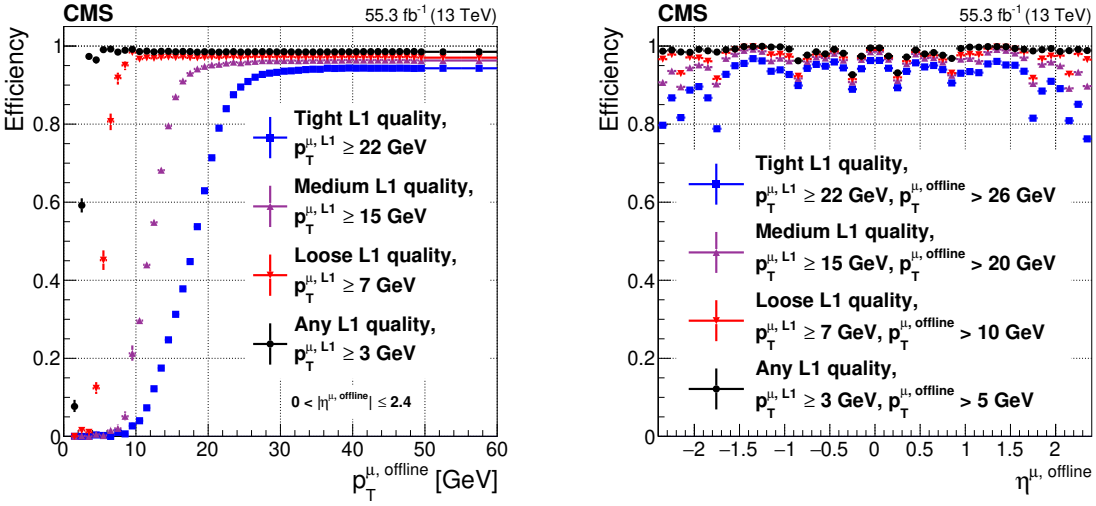


Figure 10. Level-1 muon trigger efficiency for all possible Level-1 muon qualities as a function of $p_{\mathrm{T}}^{\mathrm{offline}}$ (left) and η^{offline} (right), for all reconstructed muons in the CMS acceptance ($|\eta^{\mathrm{offline}}| < 2.4$), measured with the tag-and-probe method described in the text with the full 2018 data set. The $p_{\mathrm{T}}^{\mathrm{L1}}$ thresholds and muon qualities shown are the most commonly used during Run 2. The efficiency in the right plot is for muons with $p_{\mathrm{T}}^{\mathrm{offline}}$ in the plateau region, well above the $p_{\mathrm{T}}^{\mathrm{L1}}$ threshold.

2020 JINST 15 P10017

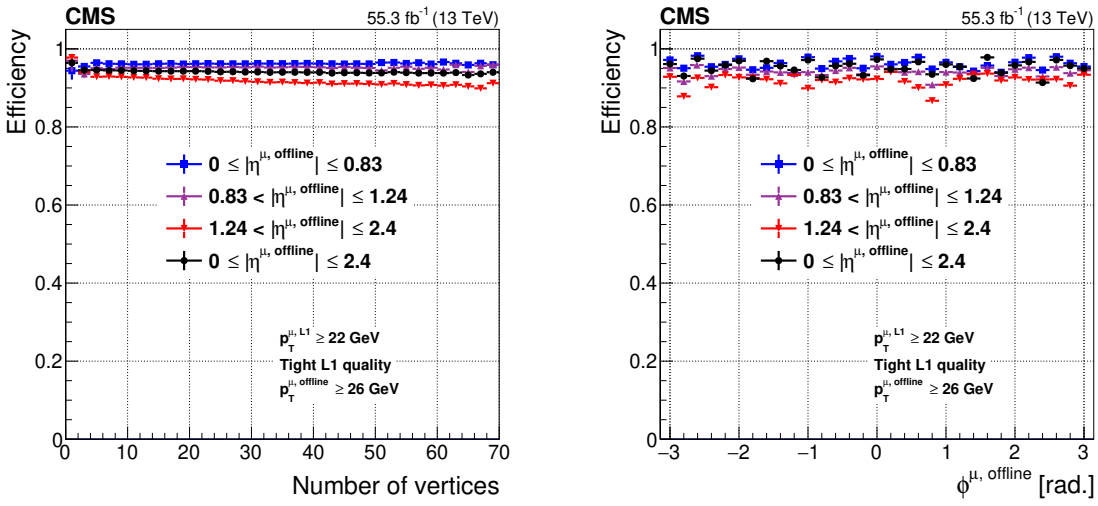


Figure 11. Level-1 trigger efficiency of the muon track finders as a function of the number of offline reconstructed vertices (left) and muon ϕ (right), measured with the tag-and-probe method described in the text with the full 2018 data set. These measurements are shown for the most commonly used single-muon trigger threshold in 2018 ($p_{\mathrm{T}}^{\mathrm{L1}} > 22\,\mathrm{GeV}$). The efficiency has no dependence on the number of vertices for central muons, and a very mild dependence for endcap muons. The efficiency modulation in ϕ follows the geometrical acceptance of the muon detector: the efficiency is higher in the regions where the detector layers overlap. The efficiency drops at $\phi = -2.8$ and 0.8 are caused by detector inefficiencies.

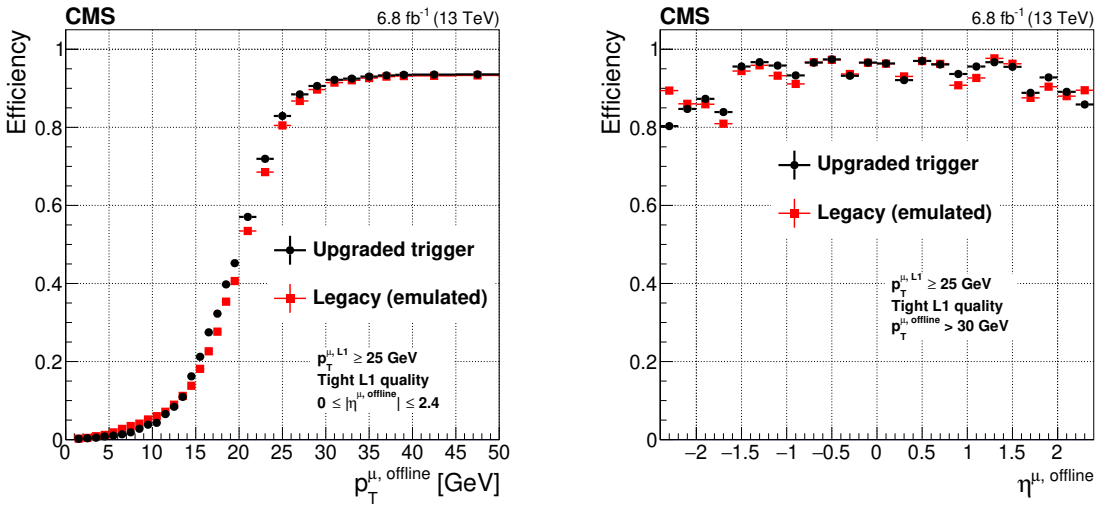


Figure 12. Efficiency of the re-emulated legacy Run 1 algorithms compared with the upgraded Run 2 algorithms, measured using a tag-and-probe technique described in the text, plotted as a function of the offline reconstructed muon p_{T} (left) and η (right). The left figure shows a sharper turn-on efficiency for the upgraded system for muons with p_{T} between 5 and 25 GeV.

2020 JINST 15 P10017

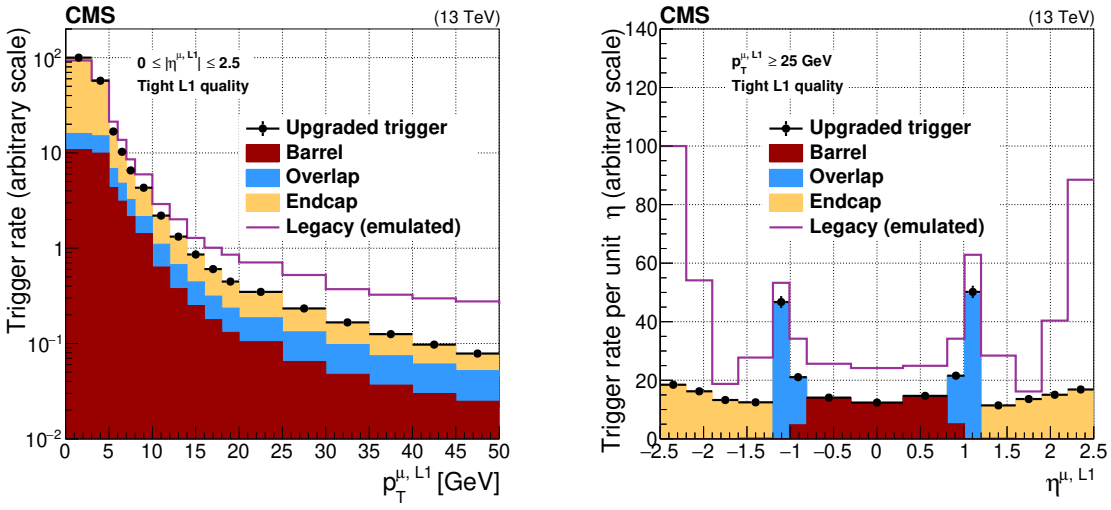


Figure 13. Rates of the re-emulated legacy Run 1 algorithms compared to the upgraded Run 2 algorithms, as a function of the Level-1 muon trigger p_{T} threshold (left) and η (right). The most common Level-1 single-muon trigger threshold used in 2017 was $p_{\mathrm{T}}^{\mu,\,\mathrm{L1}} \geq 25$ GeV.

7 The Level-1 calorimeter trigger and its performance

The calorimeter trigger was partially upgraded before data taking in the spring of 2015, and was completed in March 2016.

It is organized in two layers: Layer-1 collects and calibrates the trigger primitives coming from the calorimeters. Layer-2 receives the output from Layer-1 and reconstructs and calibrates further physics objects like electrons, photons, tau leptons, jets, and energy sums. The following sections describe the algorithms developed to reconstruct and identify electrons and photons, tau leptons, and hadron jets, and to assign accurate energies and positions to each.

7.1 Input calorimeter trigger primitive processing

Calorimeter trigger towers (TTs) group 5×5 crystals in the ECAL barrel (EB) along with the HCAL barrel (HB) tower directly behind them, with a $\Delta\eta\times\Delta\phi$ size of 0.087×0.087. In the endcaps (EE crystals, HE, and HF), the grouping logic is more complicated because of the layout of the crystals, which results in TTs with $\Delta\eta\times\Delta\phi$ sizes of up to 0.17×0.17. Look-up tables are implemented in Layer-1 to calibrate electromagnetic energy deposits in the ECAL, as well as hadronic energy deposits in both ECAL and HCAL towers. This calibration is performed in addition to calibrations already applied by the ECAL and HCAL electronics, and accounts for the changing calorimeter response over time, in particular, from radiation damage. An unforeseen timing effect of the changing crystal response is discussed in appendix A. The Layer-1 calibrations compensate for various effects including, but not limited to, the average particle energy loss in the tracker material in front of the calorimeters. The calibration factors for ECAL (HCAL) are binned in η and E_{T}, and are derived from single-photon (single-pions) simulations.

Figure 14 shows the scale factors derived for both ECAL and HCAL trigger tower inputs, as a function of η, for various bins in E_{T}. The increase of the calibration factors with η reflects the profile

2020 JINST 15 P10017

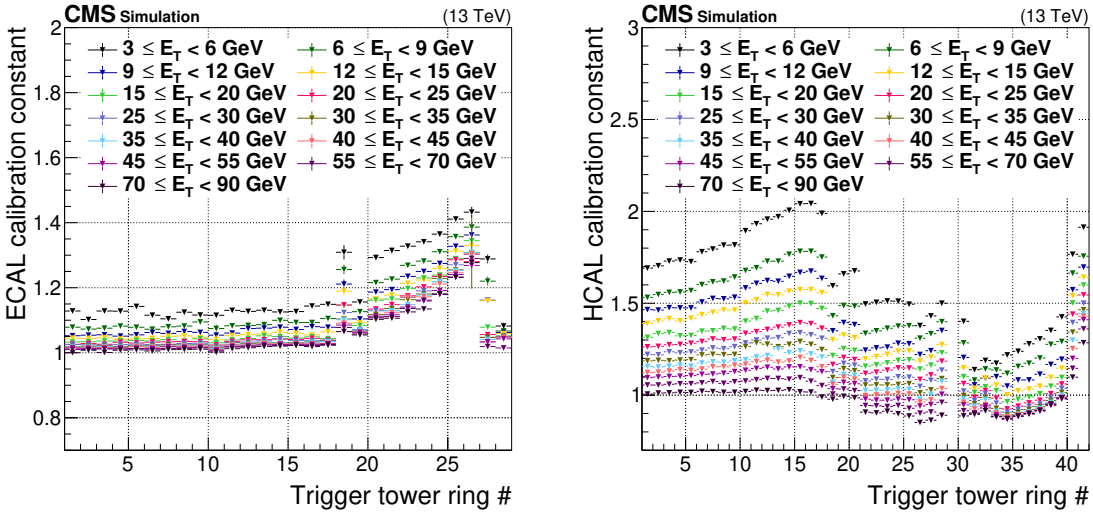


Figure 14. Layer-1 energy scale factors for ECAL (left) and HCAL (right), shown for each constant-$|\eta|$ ring of trigger towers. As specified in the legend, the color of each point corresponds to a range of uncalibrated trigger primitive transverse energy values received by the Layer-1 calorimeter trigger. Because of the HCAL geometry, the signals from trigger tower ring 29 are divided between rings 28 and 30, and no scale factors are applied.

of the detector material in front of the calorimeters. The choice of the binning of the scale factors respects the hardware limitation and takes into account the dependency of the resolution in E_{T}.

The ECAL and HCAL TT information sent to the Layer-2 contains the combined ECAL plus HCAL energy sum, the ECAL/HCAL energy ratio, and additional flags, such as the fine-grain veto bit described in section 7.2, and a minimum-bias collision bit based on the HF detector used for some special runs. The TT information, which constitutes the calorimeter trigger primitives, is streamed with a 9-fold time multiplexing, and sent via asynchronous 10 Gb/s optical links to the Layer-2 trigger.

7.2 The electron and photon trigger algorithm

Electrons (e) and photons (γ) are indistinguishable to the Level-1 trigger since tracking information is not available. The e/γ reconstruction algorithm proceeds by clustering total (ECAL plus HCAL) energy deposits around a "seed" trigger tower defined as a local energy maximum above $E_{\mathrm{T}} = 2$ GeV. Clusters are built dynamically, i.e., including surrounding towers over 1 GeV without any predetermined cluster shape requirement, and further trimmed to include only contiguous towers to match the electron footprint in the calorimeter and optimize the trigger response. The trimming process results in various candidate shapes being produced that can be categorized and used for identification purposes. As illustrated in figure 15, the maximum size of the clusters is limited to 8 TTs to minimize the impact of pileup energy deposits, while including most of the electron or photon energy. An extended region in the ϕ direction is used to obtain better coverage of the shower since the electron energy deposit extends along the ϕ-direction because of the magnetic field and bremsstrahlung.

2020 JINST 15 P10017

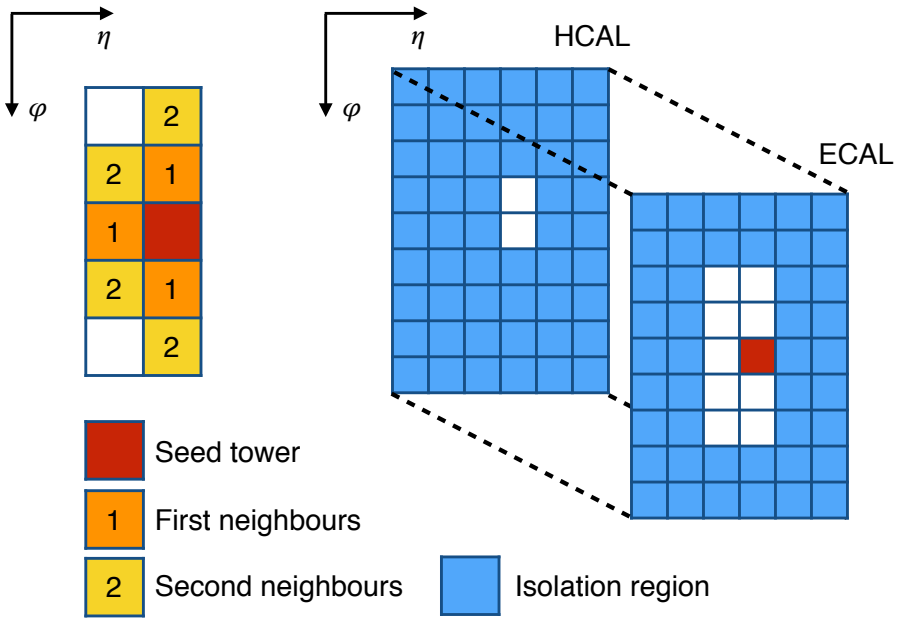


Figure 15. The Level-1 e/γ clustering algorithm and isolation definition. A candidate is formed by clustering neighboring towers (orange and yellow) if they can be linked to the seed tower (red). Each square represents a trigger tower. A candidate is considered isolated if the E_T in the isolation region (blue) is smaller than a given value. Details are given in the text.

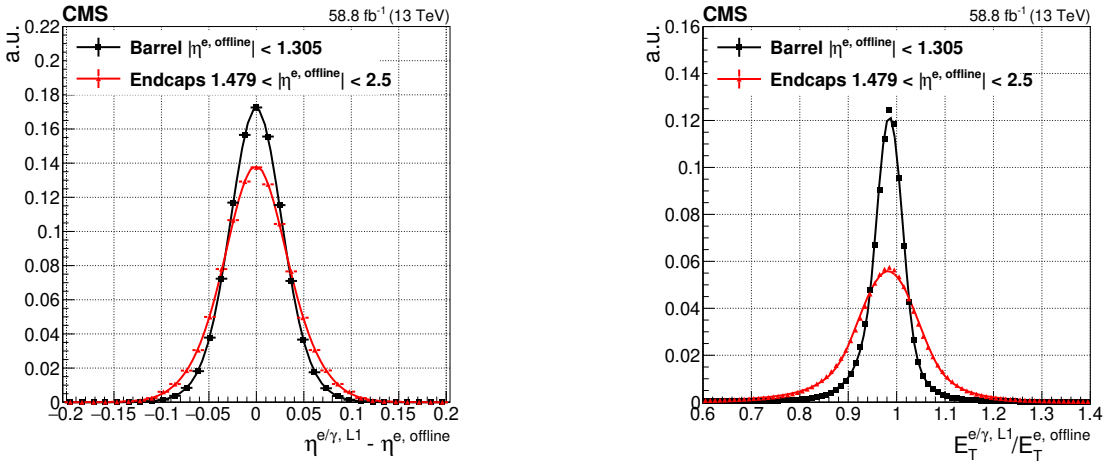


Figure 16. The pseudorapidity position of Level-1 e/γ candidates with respect to the offline reconstructed electron position, separately for the barrel and endcap regions(left). The relative transverse energy of the Level-1 e/γ candidates with respect to the offline reconstructed electron transverse energy, also separately for the barrel and endcap regions (right). The functional form of the fits consists of a two-sided tail symmetric Crystal Ball function for the left plot and a combination of a Gaussian and an one-sided tail asymmetric Crystal Ball function for the right plot.

2020 JINST 15 P10017

The e/γ candidate position is the energy-weighted position of the cluster towers. Figure 16 shows the position and transverse energy compared with those for objects reconstructed offline. Better position resolution improves the computation of more sophisticated variables, such as invariant masses at the μGT level. The data used consist of events triggered by a single electron trigger and tag-and-probe selections, which makes the sample pure in $Z \rightarrow ee$ candidates, with the corresponding p_T spectrum. The resolution of the offline position is driven by the tracker track uncertainty.

To reduce background rates, a shape veto is defined to reject the clusters least compatible with a genuine e/γ candidate such as pileup-induced energy deposits. Additional identification criteria are also defined:

- The Fine Grain Veto Bit. This veto is used in the barrel to quantify the compactness of the electromagnetic shower within the seed tower and discriminates against hadron-induced showers.

- The H/E veto. This veto requires a low ratio of HCAL to ECAL energy in the seed tower. Different thresholds are used in the barrel and the endcap regions.

These identification variables are optimized to reduce the rate of misidentified electrons while maintaining the maximum trigger efficiency for genuine electrons, and are removed for candidates with $E_T > 128$ GeV.

Isolation requirements are added to the identification criteria to produce a collection of isolated Level-1 e/γ candidates. The isolation transverse energy E_T^{iso} corresponds to the E_T deposit in the 6×9 TT region in $\eta \times \phi$ around the seed tower, from which the e/γ E_T is subtracted (illustrated in figure 15). To determine if an e/γ candidate is isolated, a threshold stored in a LUT is applied to E_T^{iso} depending on the $E_T^{e/\gamma}$, the η position, and a pileup estimator called n_{TT}. The latter is obtained by counting the number of TTs with $E_T^{TT} \geq 0.5$ GeV in the eight central η rings of the calorimeters ($|\eta| \leq 0.34$). The isolation threshold is optimized to target a specific rate and efficiency for certain E_T ranges. Two working points were derived using $Z \rightarrow ee$ collision events and a zero bias trigger sample to estimate the rate. A loose set of isolation requirements is used for candidates in trigger algorithms with intermediate E_T thresholds (between 20 and 30 GeV), which are typically dielectron and cross-trigger algorithms. For single electron algorithms, which apply energy thresholds on the electrons above 30 GeV, that are targeting events with a Z or a W boson, a tighter set of isolation requirements is implemented.

The sum of the E_T of the seed and clustered towers is the raw E_T of the e/γ candidate. An additional energy calibration is performed in the Layer-2 trigger with the scale factors derived from $Z \rightarrow ee$ collision events. The raw energy is scaled with factors depending on the η position of the seed tower, the cluster shape, and the cluster E_T.

The trigger efficiency of the upgraded e/γ algorithm is shown in figure 17. Performances for both the nonisolated and the isolated Level-1 e/γ triggers are provided. The studies are performed using a tag-and-probe technique based on $Z \rightarrow ee$ events recorded in 2018 by an HLT trigger path requiring a tight electron with $p_T > 32$ GeV. Both the tag and the probe are offline electrons required to be within the ECAL fiducial volume ($|\eta| < 1.4442$, or $|\eta| > 1.566$ and $|\eta| < 2.5$) and to pass the loose electron identification criteria. In addition, the tag is required to have a p_T above 30 GeV, and to be geometrically matched to the HLT electron triggering the event within

2020 JINST 15 P10017

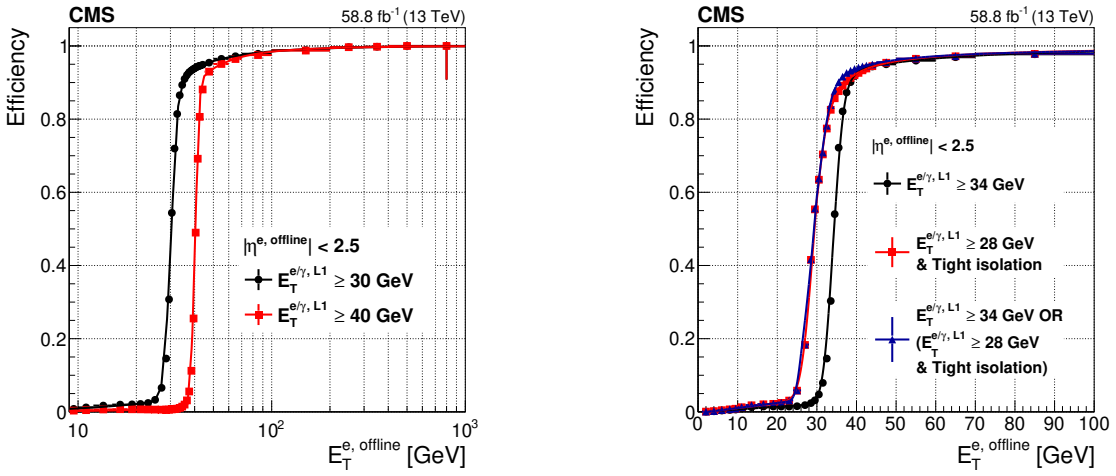


Figure 17. The Level-1 e/γ trigger efficiency as a function of the offline reconstructed electron E_T for thresholds of 30 and 40 GeV (left). The Level-1 trigger efficiency as a function of the offline reconstructed electron E_T for two typical unprescaled algorithms used in 2018 (right): an E_T threshold of 34 GeV in black, and of 28 GeV with the tight set of isolation requirements in red (as discussed in the text). The efficiency curve for the logical OR of the two algorithms is shown in blue. The functional form of the fits consists of a cumulative Crystal Ball function convolved with a polynomial or exponential function in the low E_T region.

$\Delta R < 0.3$. All other reconstructed electrons in the event passing the loose identification criteria are probe electrons. They are geometrically matched to Level-1 e/γ candidates with $\Delta R < 0.3$ and are used to evaluate the Level-1 e/γ trigger efficiency. The tag-and-probe electrons in the pair must not be within $\Delta R < 0.6$ of each other. The invariant mass of the tag-and-probe electron system is required to be between 60 and 120 GeV. The trigger efficiency as a function of the number of offline reconstructed vertices is shown in figure 18. The left plot shows the Level-1 e/γ isolated trigger efficiency for a 32 GeV threshold as a function of the number of offline reconstructed vertices. The trigger efficiency is also shown for the tight set of isolation requirements. The right plot shows in black (red) the Level-1 trigger rate, measured using an unbiased data set with an average pileup of 49, for a single e/γ algorithm as a function of the E_T threshold applied on the candidate without (with) the tight set of isolation requirements. The same plot shows in blue (yellow), the Level-1 trigger rate for a double e/γ algorithm as a function of the E_T threshold applied on the subleading e/γ candidate without (with) the tight set of isolation requirements on the leading e/γ candidate (the E_T threshold on the leading candidates is always 10 GeV higher). The rates of seeds with and without isolation converge at high $E_T^{e/\gamma,\,L1}$ because of the relaxation of the isolation criteria with $E_T^{e/\gamma,\,L1}$.

7.3 The hadronic tau lepton trigger algorithm

The hadronically decaying τ lepton trigger algorithm efficiently reconstructs τ lepton decays to one, two, or three charged or neutral pions (τ_h). These pions may produce more than one cluster spatially separated in ϕ because of the magnetic field. Although the τ_h energy deposit is typically more spread out than that of an electron, the dynamic clustering developed for the e/γ trigger is adapted to reconstruct these individual clusters, which can subsequently be merged.

2020 JINST 15 P10017

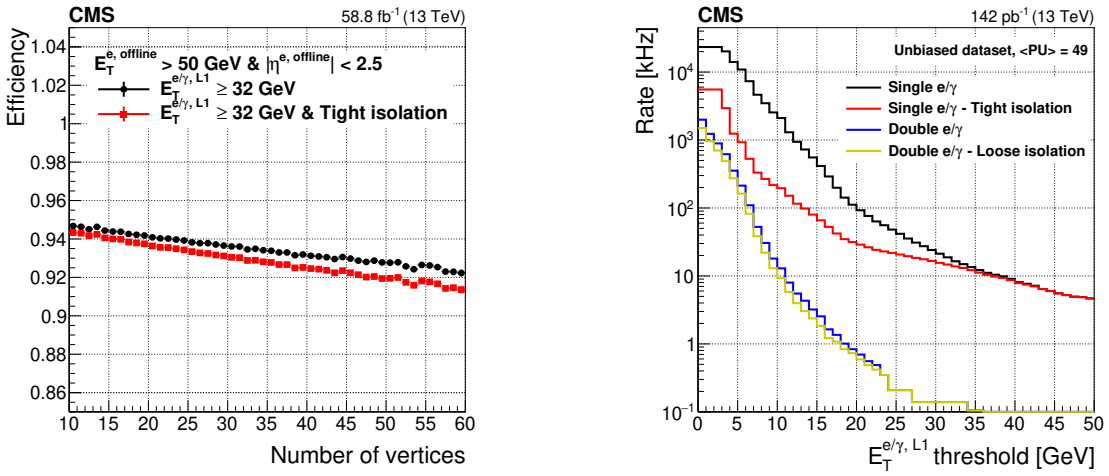


Figure 18. The Level-1 e/γ isolated trigger efficiency (left) as a function of the number of offline reconstructed vertices and the Level-1 trigger rate (right) as a function of the E_T threshold applied on the candidate.

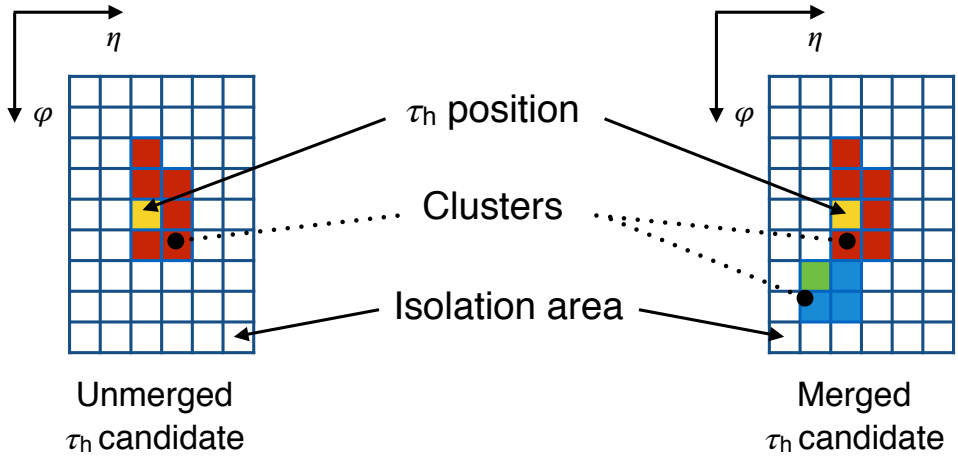


Figure 19. The Level-1 τ clustering algorithm and isolation definition. The e/γ dynamic clustering is used to reconstruct single clusters around local maxima or seeds (yellow and green), which can then be merged into a single τ_h candidate. Each square represents a trigger tower where the ECAL and HCAL energies are summed. A candidate is considered isolated if the E_T in the isolation region (white) is smaller than a chosen value.

Figure 19 illustrates the τ lepton reconstruction algorithm, which merges two neighboring clusters under some proximity conditions. Hadronically decaying τ leptons are typically low-multiplicity jets, and have less surrounding hadronic activity than QCD-induced jets. The candidate position is computed as an energy-weighted average centered around the seed tower of the main cluster, giving four times better resolution than the Run 1 τ lepton trigger algorithm. An isolation threshold, which depends on the E_T and η of the τ lepton, and the n_{TT} variable (as discussed in section 7.2), is applied to discriminate genuine τ leptons from QCD-induced jets. The isolation requirement is loosened for high n_{TT} to ensure constant τ lepton identification efficiency as a function of pileup. A relaxation of the isolation with E_T is also implemented to achieve the

2020 JINST 15 P10017

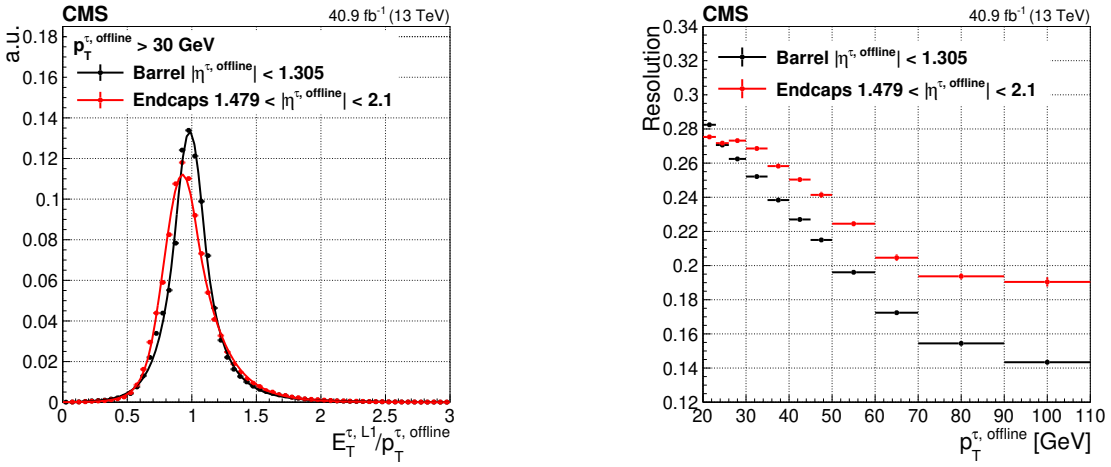


Figure 20. The Level-1 τ trigger energy response with respect to the offline reconstructed τ lepton p_T, as measured in 2017 data for the barrel and endcap regions (left). The fits consist of Crystal Ball functions. The resolution as a function of the offline τ lepton p_T (right), where the resolution is estimated by the root-mean-square of the $E_T^{\tau,\,L1}/p_T^{\tau,\,offline}$ distribution, divided by its mean, in bins of $p_T^{\tau,\,offline}$.

maximum efficiency at high E_T. The isolation thresholds are stored in a LUT that can be optimized to target a specific rate and efficiency for a given p_T range, e.g., for a τ lepton pair from a Higgs boson decay. With the intense LHC running conditions during Run 2, the working point for isolation is adjusted to provide optimum efficiency even at the peak instantaneous luminosity of $2.1 \times 10^{34}\,\mathrm{cm}^{-2}\,\mathrm{s}^{-1}$. The isolation optimization is performed on simulated $Z \rightarrow \tau\tau$ samples to evaluate the signal efficiency and on unbiased data to estimate the rate.

The τ lepton E_T is calibrated using corrections that depend on the raw E_T and η of the candidate, the presence of a merged cluster, and an estimate of the H/E fraction. The upgraded Level-1 τ lepton trigger energy resolution for barrel and endcap separately is shown in figure 20 (left).

By using a smaller number of TTs to reconstruct the energy deposit footprint of the τ lepton more precisely, the upgraded algorithm is more resilient against pileup and allows more precisely adjustable thresholds for physics. Figure 20 (right) shows the energy resolution of the upgraded τ trigger algorithm as a function of p_T.

The performance of the Level-1 τ algorithm is measured in Run 2 data for τ leptons from $Z \rightarrow \tau_\mu\tau_h$ decays using a tag-and-probe technique, where τ_μ represents a decay to a muon and neutrinos. The measurement is performed in events that satisfy the single-muon HLT path with a 27 GeV threshold on the muon p_T. The events contain a well-identified and isolated μ-τ_h pair satisfying transverse mass $m_T(E_T^{miss},\mu) < 30\,\mathrm{GeV}$ and visible mass $40 < m_{vis}(\tau_h,\mu) < 80\,\mathrm{GeV}$, where the computation of $m_{vis}(\tau_h,\mu)$ only includes the visible decay products of the τ_h. The tag muon is required to have $\Delta R < 0.5$ to the HLT muon. The probe hadronically decaying τ leptons are reconstructed using the standard hadrons-plus-strip algorithm [24], and selected using a "medium" isolation criteria [24], and are required to satisfy $p_T > 20\,\mathrm{GeV}$ and $|\eta| < 2.1$; discriminators are also applied to reduce the contamination from muons and electrons. The details of the offline τ lepton reconstruction are described in ref. [24]. The probes are matched to Level-1 hadronic τ candidates within $\Delta R < 0.5$ and used for efficiency measurements.

2020 JINST 15 P10017

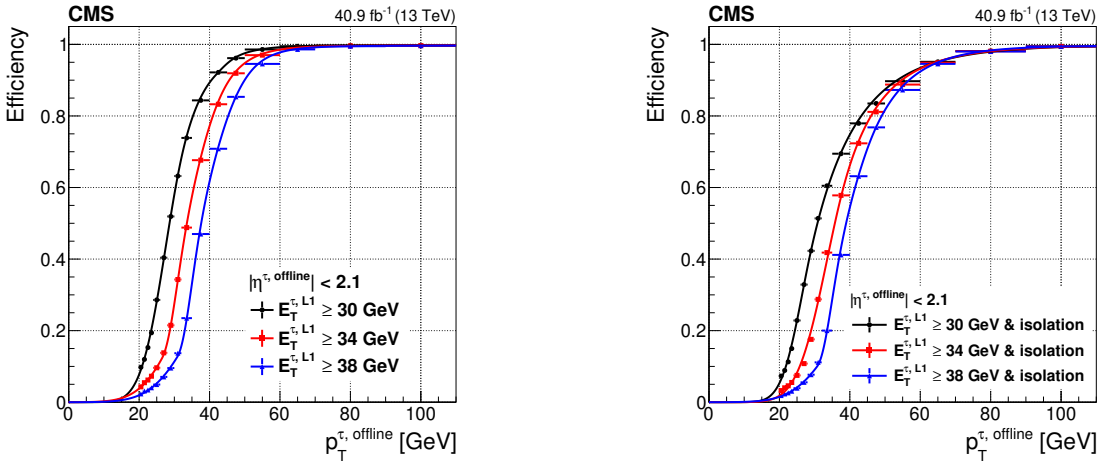


Figure 21. The Level-1 τ trigger efficiency, as a function of the offline reconstructed τ lepton p_T, for typical thresholds of 30, 34, and 38 GeV (left). The Level-1 isolated τ trigger efficiency, as a function of the offline reconstructed τ E_T, for the same three thresholds (right). The functional form of the fits consists of a cumulative Crystal Ball function convolved with an arc-tangent.

The trigger efficiency, plotted as a function of the offline reconstructed τ lepton p_T, is shown in figure 21 for nonisolated and isolated Level-1 τ candidates. The relaxation of the isolation identification criteria with E_T ensures that the efficiency reaches a plateau value of 100% at high E_T. The turn-on curves are obtained by matching geometrically the τ candidates reconstructed offline that pass all the identification and isolation requirements of the $H \rightarrow \tau\tau$ analysis with its Level-1 counterpart. The stability of the efficiency with respect to pileup is illustrated in figure 22 (left). Figure 22 (right) shows the double-τ rate as function of the E_T threshold applied to both of the Level-1 τ candidates. The rate is measured in an unbiased data sample. For typical thresholds of ≈30 GeV, a significant rate reduction is achieved by using the isolation requirement.

7.4 The jet and energy sum trigger algorithms

The Level-1 jet reconstruction algorithm is based on square-jet approach similar to that used in Run 1, but uses a 9×9 TT sliding window centered on a local maximum, the jet seed, with $E_T > 4$ GeV. In the barrel, the window size matches the anti-k_T [25] clustering size of 0.4 used in the offline jet reconstruction. A jet candidate must have a seed energy greater than the TTs in the triangle above the diagonal of the 9×9 square window, and greater than or equal to the TTs in the triangle below the same diagonal. This is to avoid double counting and to prevent TTs with the same energy from vetoing one another when being considered as a jet seed. The veto condition applied is antisymmetric along the diagonal of the 9×9 window to prevent TTs with the same energy from vetoing one another. The jet candidate energy is the sum of all TT energies in the 9×9 window. In addition to reconstructed jets, the total scalar sum of transverse energy over all TTs, E_T, and the magnitude of the vector sum of transverse energy over the same TTs, E_T^{miss}, use trigger tower granularity. The total scalar transverse energy of all jets, H_T, and the corresponding magnitude of the vector sum H_T^{miss} are computed using Level-1 jets.

2020 JINST 15 P10017

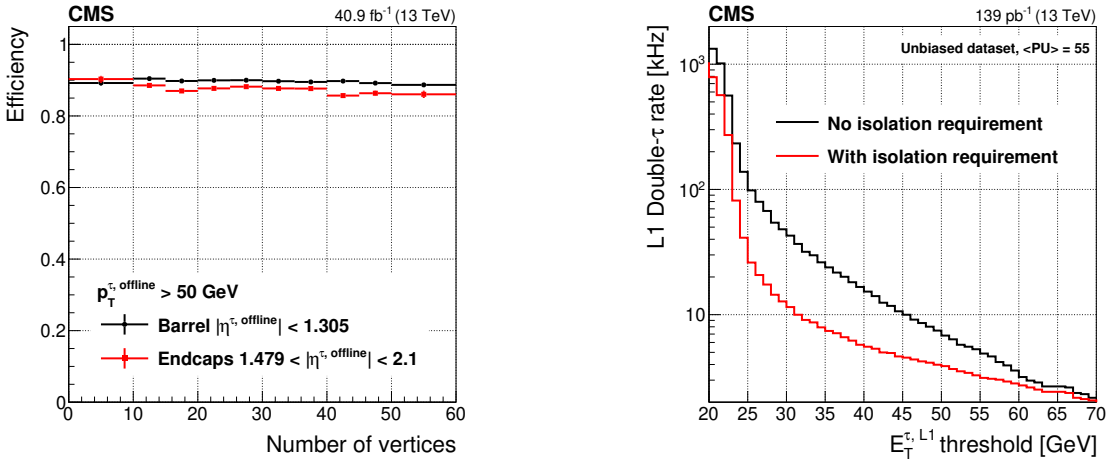


Figure 22. The integrated Level-1 selection efficiency for the isolated τ trigger with $E_T \geq 30$ GeV, matched to an offline reconstructed and identified τ lepton with $p_T > 50$ GeV, as a function of the number of offline reconstructed vertices (left). The Level-1 double-τ trigger rate, as a function of the E_T threshold, for τ candidates with and without an isolation requirement applied (right). The rate is measured requiring two τ candidates with E_T larger than the bin value, in a unbiased data set with an average pileup of 55.

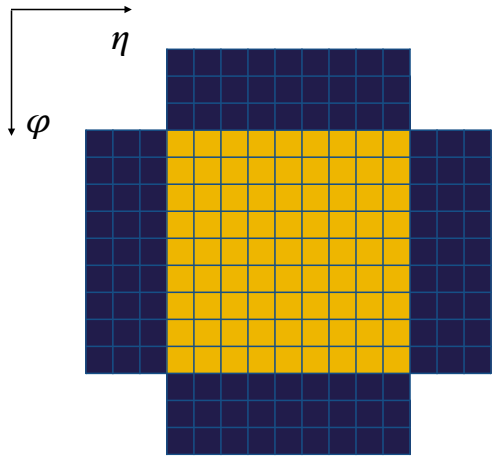


Figure 23. The area used by the jet pileup subtraction algorithm to estimate the energy deposit from the local pileup, in blue, and the area used to measure the energy of the Level-1 jet, in orange.

The estimated E_T from pileup, which is subtracted from each jet, is computed locally on a jet-by-jet basis in each bunch crossing, to respond dynamically to fluctuating pileup conditions. The chosen pileup subtraction algorithm provides a significant rate reduction, while maintaining efficiency. Figure 23 shows the regions that are used to estimate the local pileup energy to be subtracted from the jet energy. The pileup is estimated using four 3×9 outer regions, one on each side of the 9×9 jet square. The pileup E_T is calculated as the energy sum of the three lowest energy regions, so the E_T from an adjacent jet in the remaining outer region is not subtracted from the E_T. Since this area for subtraction (3 of 4 outer areas) equals the jet area, the implementation is simple.

2020 JINST 15 P10017

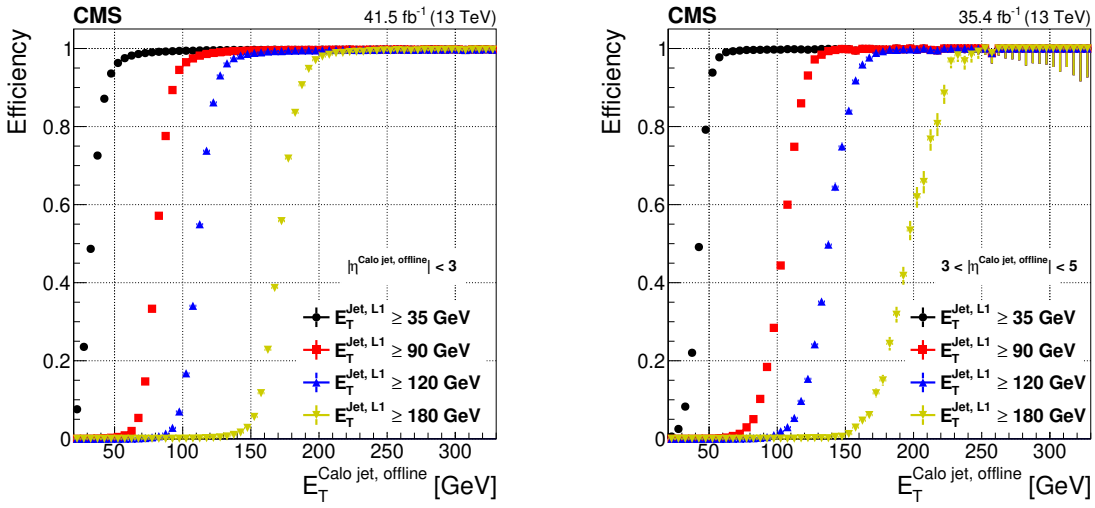


Figure 24. Efficiency curves for the Level-1 jet trigger for the barrel + endcap (left) and forward (right) pseudorapidity ranges.

To ensure consistent jet energy response, Level-1 jets are calibrated in bins of jet p_T and η, since any loss or mismeasurement will depend on the energy of the jet and the material it traverses. A dedicated LUT is derived from a QCD multijet simulation that returns a p_T scale factor that is applied to each jet. The LUT is derived by matching Level-1 jets to generator jets within $\Delta R < 0.25$, then fitting correction curves produced in bins of jet η of $1/\langle E_T^{L1}/E_T^{gen}\rangle$ as a function of $\langle E_T^{L1}\rangle$.

Figure 24 shows the performance of the Level-1 jet triggers in the combined barrel and endcap region and in the forward region, measured using an independent data sample collected with a single-muon trigger. The efficiencies show a sharp turn-on and high efficiency for a number of thresholds, representative of those used in Run 2 for various single-jet and multijet seeds. Figure 25 shows the efficiency curves for the Level-1 H_T and E_T^{miss} triggers. The E_T^{miss} trigger efficiency is measured using events triggered by and reconstructed with a single muon, and is plotted as a function of offline E_T^{miss}, which is the magnitude of the negative vector sum of the p_T of all calorimeter energy deposits, with $|\eta| \leq 5.0$.

Toward the end of 2016 data taking, an increase in the instantaneous luminosity revealed a significantly nonlinear dependence of the E_T^{miss} rates on event pileup. For 2017 and 2018 data taking, pileup mitigation was implemented and applied on an event-by-event basis to the E_T^{miss} algorithm. The event pileup is estimated with the variable n_{TT} (described in section 7.2) and is used along with the TT η to retrieve from a LUT a pileup- and η-dependent E_T threshold below which TTs do not enter the calculation of the E_T^{miss}. The LUT was derived using functions encoding the pileup estimate, the TT η, and the TT width in η, since the pileup energy per TT increases with $|\eta|$ and the TT size. The functional form and corresponding constant factors were optimized to give the best trigger efficiency, measured in single-muon triggered data, for a fixed rate calculated from unbiased data. The LUT was also derived by calculating the average TT E_T for each value of η from unbiased data, and this gave a similar performance to the function-based LUT.

2020 JINST 15 P10017

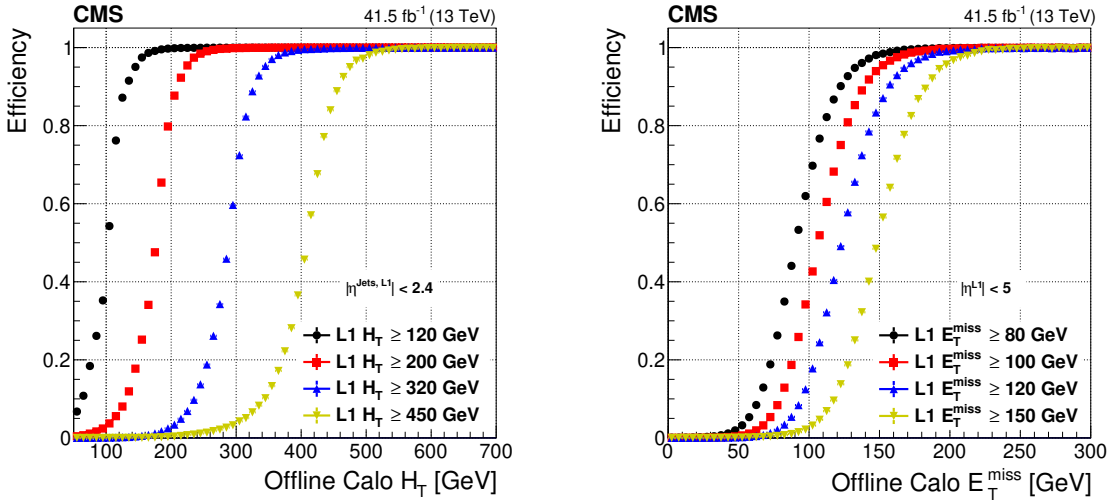


Figure 25. Efficiency curves for the scalar sum of jet energy with E_{T}≥30 GeV (left) and missing transverse energy (right) for various thresholds. The thresholds are indicated as L1 H_{T} and L1 $E_{\mathrm{T}}^{\mathrm{miss}}$ in the legends.

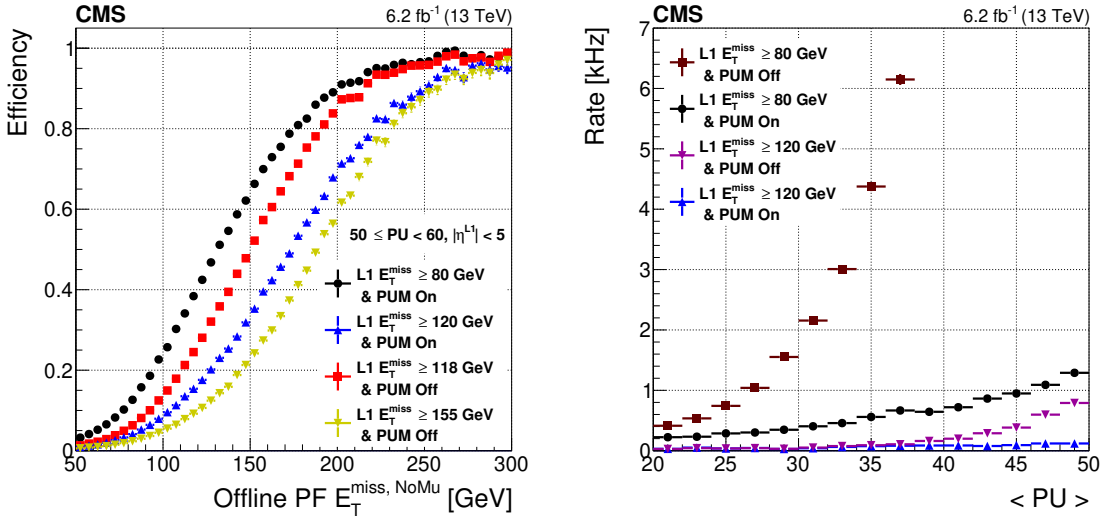


Figure 26. Efficiency curves with and without pileup mitigation (PUM) applied are compared (left) for the thresholds that give the same rate. These are shown as a function of the offline reconstructed particle flow missing energy excluding muons (PF $E_{\mathrm{T}}^{\mathrm{miss,NoMu}}$). Rate versus the average pileup per luminosity section is shown (right) with and without pileup mitigation applied.

2020 JINST 15 P10017

The improvement of the $E_{\mathrm{T}}^{\mathrm{miss}}$ trigger efficiency after using the pileup mitigation algorithm is shown in figure 26, for events from 2018 single-muon triggered data with pileup between 50 and 60. The rate of the Level-1 $E_{\mathrm{T}}^{\mathrm{miss}}$ trigger with a threshold of 80 (120) GeV with pileup mitigation enabled is the same as the rate for a threshold of 118 (155) GeV with pileup mitigation switched off. Also shown in figure 26 is the pileup dependence for fixed thresholds of the Level-1 $E_{\mathrm{T}}^{\mathrm{miss}}$ algorithm, with and without pileup mitigation. Rate is calculated from unbiased data for 2855 filled bunches for the Level-1 thresholds of 80 and 120 GeV, where the pileup shown is the average pileup per luminosity section. Applying pileup mitigation, by excluding low-energy TTs in events with significant pileup and reducing the contribution from large TTs at large eta, provided a significant rate reduction while maintaining trigger efficiency. This allowed the Level-1 $E_{\mathrm{T}}^{\mathrm{miss}}$ threshold to be reduced, increasing sensitivity to a range of important physics channels.

7.5 Adjustments for heavy ion collisions

In heavy ion (HI) lead-lead collisions, a large particle multiplicity variation is observed; although peripheral collisions can result in only a few particles per interaction, central events can produce large multiplicities equivalent to pp collisions with pileup of 200–300. While most of the algorithms developed for pp collisions were reused, the wide range of multiplicity required that some of the Level-1 algorithms were optimized, and a few were developed specifically for HI collisions.

To select low-p_{T} hadronic collisions efficiently, a minimum bias trigger was developed based on a coincidence of energy deposits in the positive and negative η sides of the HF calorimeter. Using the same principle, an ultra-peripheral collision (UPC) trigger was designed to be activated only in a specific low-energy region. A high multiplicity UPC algorithm was also developed, based on the imbalance between the positive and negative η sides of the sum of trigger tower E_{T} in the barrel calorimeter.

In addition, the parameters of the e/γ algorithm were adapted by removing the H/E constraint and adjusting the fine grain bit threshold. For optimal performance in the HI environment, the jet pileup subtraction algorithm used for proton collisions was replaced with an alternative, based on the average energy in ϕ-rings of the calorimeter.

8 The global trigger

The μGT combines information from both the μGMT and the calorimeter Layer-2, and it performs a trigger decision based on a menu of sophisticated algorithms, as described in section 4. The μGT is made compact and reliable by merging the functionality formerly distributed across multiple distinct boards into a single processor board type. The μGT distributes its processing across up to six of these common boards working independently of each other. The outputs of the processing boards are merged before being sent to the HLT.

The μGT began operation with one processing board in 2016 and was extended to its final form of six processing boards by the beginning of 2017. The use of multiple processing boards with larger FPGAs permitted the computation of more high-level quantities, such as invariant or transverse masses, by using LUTs and digital signal processors. In this way, it is possible to migrate increasingly higher-level quantities from the HLT into the Level-1 trigger.

Occasionally, the LHC running parameters change on short notice, making it operationally challenging to reoptimize the Level-1 trigger menu. The μGT calculates preview rates for each

2020 JINST 15 P10017

prescale column, so that the shift crew can avoid premature enabling of prescale columns that would raise the Level-1 rate above the limit.

A unique classification of certain physics objects input to the μGT can be difficult. For example, a hadronic jet could be separately reconstructed as both a τ lepton and a jet by the Layer-2 trigger. This poses a problem in algorithms looking for both jets and τ leptons. The μGT implements a dedicated treatment to resolve ambiguities for all possible object combinations between Level-1 objects, such as τ leptons and jets. For example, in an event with two jets, each having $E_T > 35$ GeV, and one τ lepton with $E_T > 45$ GeV, both jets must be separated by $\Delta R > 0.2$ from the τ candidate, which ensures that such an event contains at least three nonoverlapping objects.

8.1 Dedicated analysis triggers

The large processing power available in the μGT permits the implementation of sophisticated analysis-targeted trigger algorithms. In this section, three types of such algorithms are discussed. The first type selects vector boson fusion (VBF) events using the invariant mass of jet pairs. The second type targets the production of low-mass dimuon resonances (e.g., Υ decays), and the third tags b jet candidates using jet-muon coincidences.

Dedicated vector boson fusion trigger. Higgs boson production via VBF occurs through the interaction of two W or Z bosons. The incoming quarks only lose a small fraction of their energy in the interaction. After hadronizing, the outgoing quarks typically form jets in the forward direction, with a large invariant mass and separation in η. The VBF algorithm looks for at least two jets with $E_T > 115$ and $E_T > 35$ GeV and at least one pair of jets with $E_T > 35$ GeV each and an invariant mass greater than 620 GeV. In the μGT, half of the squared mass is computed:

$$m^2_{j_1 j_2}/2 = p_T^{j_1} p_T^{j_2} [\cosh(\Delta\eta_{j_1 j_2}) - \cos(\Delta\phi_{j_1 j_2})],$$

where $\cosh(\Delta\eta_{j_1 j_2})$ and $\cos(\Delta\phi_{j_1 j_2})$ are obtained through dedicated LUTs using the η and ϕ of the jets as inputs. The algorithm can select 2- or 3-jet topologies, depending on whether the jet with $E_T > 115$ GeV enters a pair with $m_{j_1 j_2} > 620$ GeV. The performance of the Level-1 VBF trigger algorithm was measured in 2017 data, using an unbiased sample collected with a single-muon trigger. Figure 27 shows that the efficiency, as functions of the offline leading jet p_T and the maximum dijet invariant mass, reaches a high efficiency plateau for VBF-like events, making it suitable as a lower rate and high efficiency trigger for VBF-like topologies. The Level-1 VBF trigger algorithms were used to seed HLT paths in 2017 and 2018, increasing the signal acceptance, especially for invisible Higgs boson decays and $H \to \tau\tau$ [26].

Low-mass dimuon triggers. The p_T thresholds for the usual dimuon triggers are not well adapted to record dimuon resonances with masses less than 20 GeV. These thresholds are typically 15 GeV on the leading muon and 5 GeV on the subleading muon, so they only select very boosted low-mass dimuon resonances. To collect inclusive low-mass dimuon pairs at low enough rates, the μGT can compute the dimuon invariant mass $m_{\mu\mu}$, using the same technique described above in the case of the VBF trigger. Seeds requiring $3 < m_{\mu\mu} < 9$ GeV and $5 < m_{\mu\mu} < 17$ GeV are included in the menu, as shown in table 2. Figure 28 shows the Level-1 and the offline $m_{\mu\mu}$ spectrum in Run 2 data collected with multi-muon triggers. The 9.46 GeV Υ meson peak can be isolated quite distinctly after the muon

2020 JINST 15 P10017

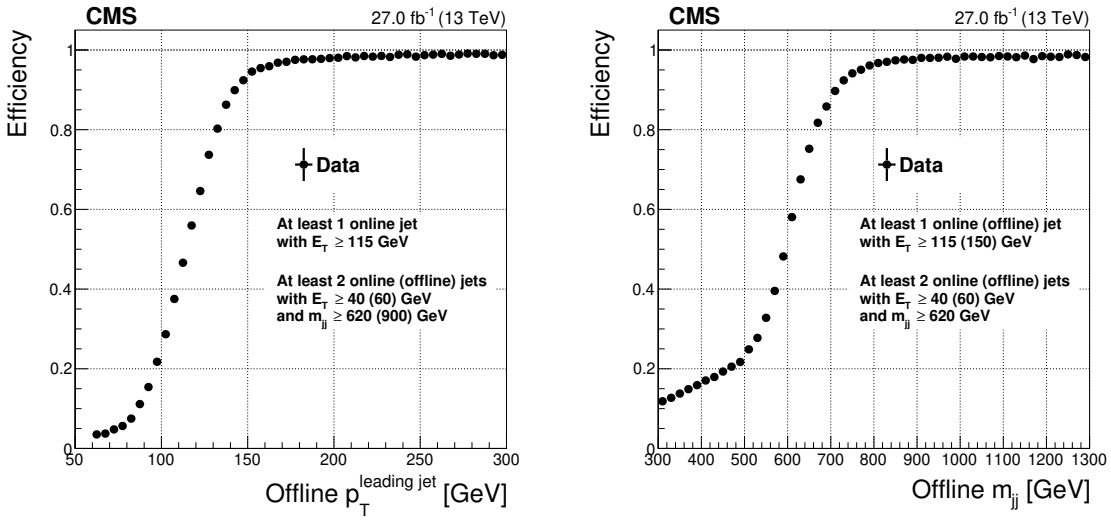


Figure 27. Efficiency of the Level-1 VBF trigger as a function of the offline leading jet p_{T} (left) and m_{jj} (right), estimated as the fraction of $\mathrm{H} \rightarrow \tau\tau$ analysis-like offline events passing the Level-1 VBF trigger selection (the Level-1 and offline requirements applied are detailed in the plots). The efficiency is evaluated using 2017 data.

coordinates are extrapolated to the nominal vertex, as described in section 6.6. A recent example of a successful low-mass trigger is the 5.6 sigma observation of $\mathrm{B}_{\mathrm{s}}^{0} \rightarrow \mu^{+}\mu^{-}$ with a branching fraction of $2.9 \pm 0.7 \pm 0.2 \times 10^{-9}$ with a limit set on $\mathrm{B}^{0} \rightarrow \mu^{+}\mu^{-} < 3.6 \times 10^{-10}$ at 95% confidence level [27].

b jet tagging using muons. A significant fraction of b hadron decays produce muons. These are often in the same direction as the rest of the products of the b hadron. The Level-1 trigger includes a simple b-tagging algorithm based on the proximity of a muon to a jet. For example, the μGT implements seeds looking for events with one $p_{\mathrm{T}} > 3\,\mathrm{GeV}$ muon and two $E_{\mathrm{T}} > 16\,\mathrm{GeV}$ jets, where the muon is within $\Delta R < 0.4$ of one of the jets. This new feature improves the efficiency and reduces the rate of the already available b jet tagging seeds that were previously limited by the use of uncorrelated $\Delta\eta$ and $\Delta\phi$ information between jets and muons.

9 Data certification and validation

The Level-1 trigger performance is monitored online by physicists working in shifts for nonstop data-taking operational support, who are trained to recognize and solve trigger problems. Trigger rates are continuously displayed for each algorithm, as well as occupancy plots and energy distributions for each physics object. Unexpected discrepancies compared with the reference distributions are investigated promptly by Level-1 object experts who determine the appropriate course of action.

The Level-1 trigger system uses a two-step process to certify the collected data. "Express certification" is typically performed within 24 hours, and identifies any anomalous behavior of the trigger that may have passed unnoticed during data taking. In the "final certification", high-quality data are selected for physics analyses. The certification is performed for both collision and cosmic ray data taking.

2020 JINST 15 P10017

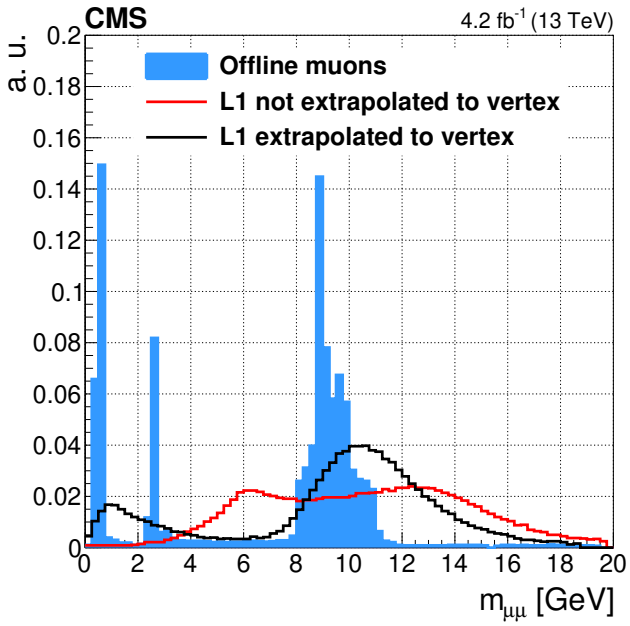


Figure 28. The offline and Level-1 $m_{\mu\mu}$ spectra of oppositely charged muons, with and without extrapolation of the Level-1 track parameters to the nominal vertex, using a data set of low-mass dimuons. The highest-mass resonance corresponds to the Υ mesons, and is clearly identifiable both offline and in Level-1, after extrapolation. The Level-1 $m_{\mu\mu}$ spectrum is shifted higher compared with the offline spectrum because of p_{T} offsets designed to make the Level-1 muon trigger 90% efficient at any given p_{T} threshold.

During express certification, the time evolution of the total output rate of the Level-1 trigger is examined, taking into account information about the beam conditions, prescale values applied, status of each subdetector, and dead time (the recording time lost because the readout system is not ready to accept new events). Individual rates of different trigger seeds targeting physics objects are compared with reference rates as a function of pileup.

For each run, data quality monitoring (DQM) plots are produced, including occupancy of muon and calorimeter trigger systems, physics object variables (such as muon η and ϕ), and the timing of trigger seeds. The data are also compared with an emulation of the Level-1 trigger reconstruction. The DQM system performs statistical tests to identify distributions that differ from expectations. Any abnormal rates or DQM distributions may indicate incorrect functioning of some part of the Level-1 trigger system, which will be studied, corrected (when possible), and taken into account in the final certification.

The final Level-1 trigger certification is based on the comparison of the efficiency and resolution measured for each type of Level-1 object to the corresponding offline quantities, combined with the information from express certification. The efficiencies are calculated for different types of trigger seeds using a tag-and-probe method, and the resolutions are determined by comparing the trigger-level kinematic variables with their offline reconstructed counterparts, similarly to the performance studies presented in this paper. If the efficiencies and resolutions show no significant deviation from the expected performance, and the results of the express certification indicate that the trigger

2020 JINST 15 P10017

operated successfully, the data is certified as valid for physics analyses from the point of view of the Level-1 trigger.

If a certain run does not pass the certification criteria, the source of the performance loss is identified and analyzed. In general, trigger performance losses are caused either by a malfunctioning Level-1 trigger subsystem itself, or by missing or corrupted input from other detector subsystems. In case of a severe performance loss, the data must be discarded independently of the origin of the problem. To minimize the data loss, the certification is performed per luminosity section.

In 2018, 1.36% of the collision data collected by CMS was certified as "bad" by Level-1, but only 0.016% was invalidated solely from Level-1 trigger issues. The remainder included some other significant detector malfunction.

10 Summary and conclusions

The CMS Level-1 trigger system was upgraded for Run 2 of the LHC. The system improved in performance and flexibility using high-bandwidth serial I/O links for data transfer and large, modern field-programmable gate arrays for reconfigurable algorithms. Maintenance improved with increased standardization through the use of the MicroTCA telecommunications standard and common hardware designs for its components.

The new trigger hardware provides improved e/γ isolation performance, substantially more efficient τ lepton identification, improved muon transverse momentum resolution, and the ability to reconstruct jets with finer calorimeter granularity. New features, such as pileup subtraction and invariant mass calculations, expand the trigger design possibilities. These improvements help to control trigger rates and keep thresholds at lower levels than would be required with the previous system despite the significantly increased LHC energy, luminosity, and pileup in Run 2. The adoption of more powerful trigger processors led to the deployment of more advanced trigger algorithms, targeting specific analyses, resulting in significant improvements in physics capability compared to Run 1.

The upgraded Level-1 trigger system operated during Run 2 with high efficiency for all physics objects, and adapted to the rapidly changing LHC running conditions. As a result, the trigger efficiency was stable and independent of the evolving LHC parameters. Special LHC running conditions and heavy-ion data taking were accommodated effectively as well, exploiting the full capability and flexibility of the trigger system.

The upgraded system improved the energy and momentum resolution, and the identification efficiency and background rejection of the Level-1 physics objects. This significantly lowered the rate at a given threshold compared with the Run 1 system, thereby allowing similar trigger requirements to fit within the unchanged Level-1 rate limit.

An analysis of Run 2 data shows that the trigger rate reduction and efficiency gain benefited the physics program of the CMS Collaboration under conditions of increased LHC energy, luminosity, and pileup. An example includes the $H \rightarrow \tau\tau$ analysis [28], which shows a significant improvement in trigger efficiency; other Higgs boson decay channel analyses maintained a similar trigger efficiency despite the harsher beam conditions. Moreover, all analyses looking for large transverse missing energy (E_T^{miss}), including searches for dark matter, supersymmetry [29], and invisible Higgs boson decay [26], were only possible in Run 2 because of the improved resolution of the Level-1 E_T^{miss}

2020 JINST 15 P10017

and the pileup mitigation algorithm. Searches for low-mass dimuon resonances exploited the invariant mass requirement for reducing the rate and lowering the muon momentum requirement [27].

Acknowledgments

We congratulate our colleagues in the CERN accelerator departments for the excellent performance of the LHC and thank the technical and administrative staffs at CERN and at other CMS institutes for their contributions to the success of the CMS effort. In addition, we gratefully acknowledge the computing centers and personnel of the Worldwide LHC Computing Grid for delivering so effectively the computing infrastructure essential to our analyses. Finally, we acknowledge the enduring support for the construction and operation of the LHC and the CMS detector provided by the following funding agencies: the Austrian Federal Ministry of Education, Science and Research and the Austrian Science Fund; the Belgian Fonds de la Recherche Scientifique, and Fonds voor Wetenschappelijk Onderzoek; the Brazilian Funding Agencies (CNPq, CAPES, FAPERJ, FAPERGS, and FAPESP); the Bulgarian Ministry of Education and Science; CERN; the Chinese Academy of Sciences, Ministry of Science and Technology, and National Natural Science Foundation of China; the Colombian Funding Agency (COLCIENCIAS); the Croatian Ministry of Science, Education and Sport, and the Croatian Science Foundation; the Research and Innovation Foundation, Cyprus; the Secretariat for Higher Education, Science, Technology and Innovation, Ecuador; the Ministry of Education and Research, Estonian Research Council via PRG780, PRG803 and PRG445 and European Regional Development Fund, Estonia; the Academy of Finland, Finnish Ministry of Education and Culture, and Helsinki Institute of Physics; the Institut National de Physique Nucléaire et de Physique des Particules / CNRS, and Commissariat à l'Énergie Atomique et aux Énergies Alternatives / CEA, France; the Bundesministerium für Bildung und Forschung, the Deutsche Forschungsgemeinschaft (DFG) under Germany's Excellence Strategy — EXC 2121 "Quantum Universe" — 390833306, and Helmholtz-Gemeinschaft Deutscher Forschungszentren, Germany; the General Secretariat for Research and Technology, Greece; the National Research, Development and Innovation Fund, Hungary; the Department of Atomic Energy and the Department of Science and Technology, India; the Institute for Studies in Theoretical Physics and Mathematics, Iran; the Science Foundation, Ireland; the Istituto Nazionale di Fisica Nucleare, Italy; the Ministry of Science, ICT and Future Planning, and National Research Foundation (NRF), Republic of Korea; the Ministry of Education and Science of the Republic of Latvia; the Lithuanian Academy of Sciences; the Ministry of Education, and University of Malaya (Malaysia); the Ministry of Science of Montenegro; the Mexican Funding Agencies (BUAP, CINVESTAV, CONACYT, LNS, SEP, and UASLP-FAI); the Ministry of Business, Innovation and Employment, New Zealand; the Pakistan Atomic Energy Commission; the Ministry of Science and Higher Education and the National Science Center, Poland; the Fundação para a Ciência e a Tecnologia, Portugal; JINR, Dubna; the Ministry of Education and Science of the Russian Federation, the Federal Agency of Atomic Energy of the Russian Federation, Russian Academy of Sciences, the Russian Foundation for Basic Research, and the National Research Center "Kurchatov Institute"; the Ministry of Education, Science and Technological Development of Serbia; the Secretaría de Estado de Investigación, Desarrollo e Innovación, Programa Consolider-Ingenio 2010, Plan Estatal de Investigación Científica y Técnica y de Innovación 2017–2020, research project IDI-2018-000174 del Principado de Asturias, and

2020 JINST 15 P10017

Fondo Europeo de Desarrollo Regional, Spain; the Ministry of Science, Technology and Research, Sri Lanka; the Swiss Funding Agencies (ETH Board, ETH Zurich, PSI, SNF, UniZH, Canton Zurich, and SER); the Ministry of Science and Technology, Taipei; the Thailand Center of Excellence in Physics, the Institute for the Promotion of Teaching Science and Technology of Thailand, Special Task Force for Activating Research and the National Science and Technology Development Agency of Thailand; the Scientific and Technical Research Council of Turkey, and Turkish Atomic Energy Authority; the National Academy of Sciences of Ukraine; the Science and Technology Facilities Council, U.K.; the U.S. Department of Energy, and the U.S. National Science Foundation. Individuals have received support from the Marie-Curie program and the European Research Council and Horizon 2020 Grant, contract Nos. 675440, 752730, and 765710 (European Union); the Leventis Foundation; the A.P. Sloan Foundation; the Alexander von Humboldt Foundation; the Belgian Federal Science Policy Office; the Fonds pour la Formation à la Recherche dans l'Industrie et dans l'Agriculture (FRIA-Belgium); the Agentschap voor Innovatie door Wetenschap en Technologie (IWT-Belgium); the F.R.S.-FNRS and FWO (Belgium) under the "Excellence of Science — EOS" — be.h project n. 30820817; the Beijing Municipal Science & Technology Commission, No. Z191100007219010; the Ministry of Education, Youth and Sports (MEYS) of the Czech Republic; the Lendület ("Momentum") Program and the János Bolyai Research Scholarship of the Hungarian Academy of Sciences, the New National Excellence Program ÚNKP, the NKFIA research grants 123842, 123959, 124845, 124850, 125105, 128713, 128786, and 129058 (Hungary); the Council of Scientific and Industrial Research, India; the HOMING PLUS program of the Foundation for Polish Science, cofinanced from European Union, Regional Development Fund, the Mobility Plus program of the Ministry of Science and Higher Education, the National Science Center (Poland), contracts Harmonia 2014/14/M/ST2/00428, Opus 2014/13/B/ST2/02543, 2014/15/B/ST2/03998, and 2015/19/B/ST2/02861, Sonata-bis 2012/07/E/ST2/01406; the National Priorities Research Program by Qatar National Research Fund; the Ministry of Science and Higher Education, project no. 02.a03.21.0005 (Russia); the Tomsk Polytechnic University Competitiveness Enhancement Program and "Nauka" Project FSWW-2020-0008 (Russia); the Programa de Excelencia María de Maeztu, and the Programa Severo Ochoa del Principado de Asturias; the Thalis and Aristeia programs cofinanced by EU-ESF, and the Greek NSRF; the Rachadapisek Sompot Fund for Postdoctoral Fellowship, Chulalongkorn University, and the Chulalongkorn Academic into Its 2nd Century Project Advancement Project (Thailand); the Kavli Foundation; the Nvidia Corporation; the SuperMicro Corporation; the Welch Foundation, contract C-1845; and the Weston Havens Foundation (U.S.A.).

A Level-1 trigger prefiring

Since the beginning of Run 2, a slowly developing shift in the shape of the ECAL pulses was observed. This effect, which manifests itself as an increasing offset in the timing calibration of the pulses, is radiation-induced and is related to the transparency loss of the ECAL crystals. Because of this, the endcap crystals at highest pseudorapidity are most affected. This timing calibration offset is compensated offline via regular pulse shape and timing calibration measurements, but was not corrected online in the formation of the ECAL TPs. With time, the accumulated offset brought the endcap pulses to the limit of the region where the trigger bunch-crossing assignment would be affected. Once this was realized, in early 2018, the endcap timing delays in the ECAL front-end

electronics were corrected, and the pulse synchronization was optimized. However, in 2016–2017, a gradually increasing fraction of ECAL TPs at $|\eta| > 2.5$ had wrongly associated an energy deposit to the previous bunch crossing (BX −1). When such a misassignment occurs it causes several effects on the data. First, it may lead the Level-1 trigger system to "prefire", i.e., to accept the earlier collision in BX −1, whereas the collision in BX 0 is the one of interest. Secondly, when the misassigned TP energy is not large enough to pass the trigger condition, it induces a bias in the energy measurement of calorimeter deposits in the trigger chain and offline.

Prefiring happens, e.g., when an ECAL TP, whose E_{T} exceeds the threshold of the single electron trigger, is assigned to BX −1; or when the misassignment of an ECAL TP leads to a large $E_{\mathrm{T}}^{\mathrm{miss}}$ reconstructed at Level-1 in BX −1. Prefiring of Level-1 triggers represents a problem in their combined effect with the CMS trigger rules. These are the conditions that prevent buffer overflows in special cases. Triggers rules are enforced immediately after the final decision of the global trigger (μGT). The most commonly enforced trigger rules prevent the issuance of more than one Level-1 trigger acceptance decision in three consecutive bunch crossings, or more than two Level-1 trigger acceptances in 25 consecutive BXs. Thus, when a trigger accepts the event in BX −1, the interesting event in BX 0 will not be accepted. The readout event in BX −1 will likely be rejected by the HLT since it is unlikely to reconstruct any interesting physics objects. The main consequence of prefiring is therefore an inefficiency in recording potentially interesting events.

The measurement of the prefiring rate requires the use of a special set of events called "unprefirable" events. An event in BX 0 is unprefirable when the event in BX −3 is accepted by the Level-1 trigger: the trigger rules veto events in BX −2 and BX −1. For every triggered event, all Level-1 objects and μGT decision bits are stored in a window of ±2BX. Therefore, from a set of selected unprefirable events, the prefiring probability can be computed for a specific analysis selection. The rate of unprefirable events is very small compared with the total number of events in any given primary data set, about 0.1%. Ad hoc corrections at the analysis level are applied to correct for this effect. One of the most affected analyses is the search for invisible decays of a Higgs boson produced via VBF, with energetic forward jets. Their measurements from an unbiased data sample result in a correction of about 1% for m_{jj} of 200 GeV and up to 20% for m_{jj} larger than 3.5 TeV [26].

Secondary effects of the TP time shift are a potential bias in the energy measurement of the calorimeter deposit in the trigger chain. If the energy of early TPs is large enough to create a Level-1 object that prefires a Level-1 trigger path, the event in BX 0 is lost. In contrast, if BX −1 is not accepted, a residual effect on BX 0 is still present because the information about the TPs associated with BX −1 is lost. This residual effect biases the energy of several Level-1 objects and causes a degradation of the trigger efficiency turn-on . Standard trigger efficiency measurements and scale factors generally applied in physics analyses account for this effect.

A second bias arises because of the impact on the ECAL selective readout logic. The TP inputs are used by the ECAL selective readout units to decide whether a certain region of the detector needs to be read out or not (zero-suppressed). Crystals associated with the early TP will be read out by the ECAL data acquisition system in zero-suppression mode, injecting a bias into the HLT/offline energy measurement. For high-p_{T} jets this effect is expected to be small because the zero-suppression thresholds are low. This energy bias is mostly recovered by the residual jet energy corrections applied at the analysis level.

2020 JINST 15 P10017

References

[1] CMS collaboration, *CMS TriDAS project. Technical design report, volume* 1*: the trigger systems*, Tech. Rep. CERN-LHCC-2000-038, CERN, Geneva, Switzerland (2000).

[2] CMS collaboration, *The CMS trigger system*, 2017 *JINST* **12** P01020 [arXiv:1609.02366].

[3] CMS collaboration, *CMS technical design report for the Level-*1 *trigger upgrade*, Tech. Rep. CERN-LHCC-2013-011, CERN, Geneva, Switzerland (2013) [CMS-TDR-12].

[4] CMS collaboration, *The CMS experiment at the CERN LHC*, 2008 *JINST* **3** S08004.

[5] CMS collaboration, *Technical proposal for the upgrade of the CMS detector through* 2020, Tech. Rep. CERN-LHCC-2011-006, CERN, Geneva, Switzerland (2011) [LHCC-P-004].

[6] G. Rumolo et al., *Electron cloud effects at the LHC and LHC injectors*, in 8$^{\text{th}}$ *International Particle Accelerator Conference (IPAC)*, MOZA1, (2017), pg. 30.

[7] CMS collaboration, *Van der Meer calibration of the CMS luminosity detectors in* 2017, Tech. Rep. CMS-CR-2018-339, CERN, Geneva, Switzerland (2018).

[8] ATLAS collaboration, *Observation of a new particle in the search for the Standard Model Higgs boson with the ATLAS detector at the LHC*, *Phys. Lett. B* **716** (2012) 1 [arXiv:1207.7214].

[9] CMS collaboration, *Observation of a new boson at a mass of* 125 *GeV with the CMS experiment at the LHC*, *Phys. Lett. B* **716** (2012) 30 [arXiv:1207.7235].

[10] CMS collaboration, *Observation of a new boson with mass near* 125 *GeV in pp collisions at* $\sqrt{s} = 7$ *and* 8 *TeV*, *JHEP* **06** (2013) 081 [arXiv:1303.4571].

[11] ATLAS and CMS collaborations, *Combined measurement of the Higgs boson mass in pp collisions at* $\sqrt{s} = 7$ *and* 8 *TeV with the ATLAS and CMS experiments*, *Phys. Rev. Lett.* **114** (2015) 191803 [arXiv:1503.07589].

[12] PCI Industrial Computer Manufacturers Group, *MTCA.*0 *R*1.0 *micro telecommunications computing architecture*, Tech. Rep., http://www.picmg.org, (2006).

[13] R. Frazier et al., *A demonstration of a time multiplexed trigger for the CMS experiment*, 2012 *JINST* **7** C01060.

[14] E. Hazen, A. Heister, C. Hill, J. Rohlf, S.X. Wu and D. Zou, *The AMC*13*XG: a new generation clock/timing/DAQ module for CMS MicroTCA*, 2013 *JINST* **8** C12036.

[15] CMS collaboration, *Performance of the CMS muon detector and muon reconstruction with proton-proton collisions at* $\sqrt{s} = 13$ *TeV*, 2018 *JINST* **13** P06015 [arXiv:1804.04528].

[16] CMS collaboration, *The CMS barrel muon trigger upgrade*, 2017 *JINST* **12** C01095.

[17] C.-J. Wang, Z.-A. Liu, J.-Z. Zhao and Z. Liu, *Design of a high throughput electronics module for high energy physics experiments*, *Chin. Phys. C* **40** (2016) 066102.

[18] J. Ero et al., *The CMS drift tube trigger track finder*, 2008 *JINST* **3** P08006.

[19] W.M. Zabolotny and A. Byszuk, *Algorithm and implementation of muon trigger and data transmission system for barrel-endcap overlap region of the CMS detector*, 2016 *JINST* **11** C03004.

[20] CMS collaboration, *Boosted decision trees in the Level-*1 *muon endcap trigger at CMS*, *J. Phys. Conf. Ser.* **1085** (2018) 042042.

[21] CMS collaboration, *Performance of CMS muon reconstruction in pp collision events at* $\sqrt{s} = 7$ *TeV*, 2012 *JINST* **7** P10002 [arXiv:1206.4071].

2020 JINST 15 P10017

[22] CMS collaboration, *Particle-flow reconstruction and global event description with the CMS detector*, 2017 *JINST* **12** P10003 [arXiv:1706.04965].

[23] CMS collaboration, *Performance of the reconstruction and identification of high-momentum muons in proton-proton collisions at* $\sqrt{s} = 13$ *TeV*, 2020 *JINST* **15** P02027 [arXiv:1912.03516].

[24] CMS collaboration, *Performance of reconstruction and identification of* τ *leptons decaying to hadrons and* ν_τ *in pp collisions at* $\sqrt{s} = 13$ *TeV*, 2018 *JINST* **13** P10005 [arXiv:1809.02816].

[25] M. Cacciari, G.P. Salam and G. Soyez, *The anti-*k_t *jet clustering algorithm*, *JHEP* **04** (2008) 063 [arXiv:0802.1189].

[26] CMS collaboration, *Search for invisible decays of a Higgs boson produced through vector boson fusion in proton-proton collisions at* $\sqrt{s} = 13$ *TeV*, *Phys. Lett. B* **793** (2019) 520 [arXiv:1809.05937].

[27] CMS collaboration, *Measurement of properties of* $B_s^0 \to \mu^+\mu^-$ *decays and search for* $B^0 \to \mu^+\mu^-$ *with the CMS experiment*, *JHEP* **04** (2020) 188 [arXiv:1910.12127].

[28] CMS collaboration, *Observation of the Higgs boson decay to a pair of* τ *leptons with the CMS detector*, *Phys. Lett. B* **779** (2018) 283 [arXiv:1708.00373].

[29] CMS collaboration, *Search for natural and split supersymmetry in proton-proton collisions at* $\sqrt{s} = 13$ *TeV in final states with jets and missing transverse momentum*, *JHEP* **05** (2018) 025 [arXiv:1802.02110].

2020 JINST 15 P10017

The CMS collaboration

Yerevan Physics Institute, Yerevan, Armenia

A.M. Sirunyan[†], A. Tumasyan

Institut für Hochenergiephysik, Wien, Austria

W. Adam, F. Ambrogi, B. Arnold, H. Bergauer, T. Bergauer, M. Dragicevic, J. Erö, A. Escalante Del Valle, M. Flechl, R. Frühwirth[1], M. Jeitler[1], N. Krammer, I. Krätschmer, D. Liko, T. Madlener, I. Mikulec, N. Rad, J. Schieck[1], R. Schöfbeck, M. Spanring, S. Templ, W. Waltenberger, C.-E. Wulz[1], M. Zarucki

Institute for Nuclear Problems, Minsk, Belarus

V. Drugakov, V. Mossolov, J. Suarez Gonzalez

Universiteit Antwerpen, Antwerpen, Belgium

M.R. Darwish, E.A. De Wolf, D. Di Croce, X. Janssen, T. Kello[2], A. Lelek, M. Pieters, H. Rejeb Sfar, H. Van Haevermaet, P. Van Mechelen, S. Van Putte, N. Van Remortel

Vrije Universiteit Brussel, Brussel, Belgium

F. Blekman, E.S. Bols, S.S. Chhibra, J. D'Hondt, J. De Clercq, D. Lontkovskyi, S. Lowette, I. Marchesini, S. Moortgat, Q. Python, S. Tavernier, W. Van Doninck, P. Van Mulders

Université Libre de Bruxelles, Bruxelles, Belgium

D. Beghin, B. Bilin, B. Clerbaux, G. De Lentdecker, H. Delannoy, B. Dorney, L. Favart, A. Grebenyuk, A.K. Kalsi, L. Moureaux, A. Popov, N. Postiau, E. Starling, L. Thomas, C. Vander Velde, P. Vanlaer, D. Vannerom

Ghent University, Ghent, Belgium

T. Cornelis, D. Dobur, I. Khvastunov[3], M. Niedziela, C. Roskas, K. Skovpen, M. Tytgat, W. Verbeke, B. Vermassen, M. Vit

Université Catholique de Louvain, Louvain-la-Neuve, Belgium

G. Bruno, C. Caputo, P. David, C. Delaere, M. Delcourt, A. Giammanco, V. Lemaitre, J. Prisciandaro, A. Saggio, P. Vischia, J. Zobec

Centro Brasileiro de Pesquisas Fisicas, Rio de Janeiro, Brazil

G.A. Alves, G. Correia Silva, C. Hensel, A. Moraes

Universidade do Estado do Rio de Janeiro, Rio de Janeiro, Brazil

E. Belchior Batista Das Chagas, W. Carvalho, J. Chinellato[4], E. Coelho, E.M. Da Costa, G.G. Da Silveira[5], D. De Jesus Damiao, C. De Oliveira Martins, S. Fonseca De Souza, H. Malbouisson, J. Martins[6], D. Matos Figueiredo, M. Medina Jaime[7], M. Melo De Almeida, C. Mora Herrera, L. Mundim, H. Nogima, W.L. Prado Da Silva, P. Rebello Teles, L.J. Sanchez Rosas, A. Santoro, A. Sznajder, M. Thiel, E.J. Tonelli Manganote[4], F. Torres Da Silva De Araujo, A. Vilela Pereira

Universidade Estadual Paulista [a], Universidade Federal do ABC [b], São Paulo, Brazil

C.A. Bernardes[a], L. Calligaris[a], T.R. Fernandez Perez Tomei[a], E.M. Gregores[b], D.S. Lemos, P.G. Mercadante[b], S.F. Novaes[a], Sandra S. Padula[a]

2020 JINST 15 P10017

Institute for Nuclear Research and Nuclear Energy, Bulgarian Academy of Sciences, Sofia, Bulgaria

A. Aleksandrov, G. Antchev, R. Hadjiiska, P. Iaydjiev, M. Misheva, M. Rodozov, M. Shopova, G. Sultanov

University of Sofia, Sofia, Bulgaria

M. Bonchev, A. Dimitrov, T. Ivanov, L. Litov, B. Pavlov, P. Petkov, A. Petrov

Beihang University, Beijing, China

W. Fang[2], X. Gao[2], L. Yuan

Department of Physics, Tsinghua University, Beijing, China

M. Ahmad, Z. Hu, Y. Wang

Institute of High Energy Physics, Beijing, China

G.M. Chen[8], H.S. Chen[8], M. Chen, C.H. Jiang, D. Leggat, H. Liao, Z. Liu, A. Spiezia, J. Tao, E. Yazgan, H. Zhang, S. Zhang[8], J. Zhao

State Key Laboratory of Nuclear Physics and Technology, Peking University, Beijing, China

A. Agapitos, Y. Ban, G. Chen, A. Levin, J. Li, L. Li, Q. Li, Y. Mao, S.J. Qian, D. Wang, Q. Wang

Zhejiang University, Hangzhou, China

M. Xiao

Universidad de Los Andes, Bogota, Colombia

C. Avila, A. Cabrera, C. Florez, C.F. González Hernández, M.A. Segura Delgado

Universidad de Antioquia, Medellin, Colombia

J. Mejia Guisao, J.D. Ruiz Alvarez, C.A. Salazar González, N. Vanegas Arbelaez

University of Split, Faculty of Electrical Engineering, Mechanical Engineering and Naval Architecture, Split, Croatia

D. Giljanović, N. Godinovic, D. Lelas, I. Puljak, T. Sculac

University of Split, Faculty of Science, Split, Croatia

Z. Antunovic, M. Kovac

Institute Rudjer Boskovic, Zagreb, Croatia

V. Brigljevic, D. Ferencek, K. Kadija, D. Majumder, B. Mesic, M. Roguljic, A. Starodumov[9], T. Susa

University of Cyprus, Nicosia, Cyprus

M.W. Ather, A. Attikis, E. Erodotou, A. Ioannou, M. Kolosova, S. Konstantinou, G. Mavromanolakis, J. Mousa, C. Nicolaou, F. Ptochos, P.A. Razis, H. Rykaczewski, H. Saka, D. Tsiakkouri

Charles University, Prague, Czech Republic

M. Finger[10], M. Finger Jr.[10], A. Kveton, J. Tomsa

Escuela Politecnica Nacional, Quito, Ecuador

E. Ayala

2020 JINST 15 P10017

Universidad San Francisco de Quito, Quito, Ecuador

E. Carrera Jarrin

Academy of Scientific Research and Technology of the Arab Republic of Egypt, Egyptian Network of High Energy Physics, Cairo, Egypt

Y. Assran[11,12], S. Elgammal[12]

National Institute of Chemical Physics and Biophysics, Tallinn, Estonia

S. Bhowmik, A. Carvalho Antunes De Oliveira, R.K. Dewanjee, K. Ehataht, M. Kadastik, M. Raidal, C. Veelken

Department of Physics, University of Helsinki, Helsinki, Finland

P. Eerola, L. Forthomme, H. Kirschenmann, K. Osterberg, M. Voutilainen

Helsinki Institute of Physics, Helsinki, Finland

E. Brücken, F. Garcia, J. Havukainen, J.K. Heikkilä, V. Karimäki, M.S. Kim, R. Kinnunen, T. Lampén, K. Lassila-Perini, S. Laurila, S. Lehti, T. Lindén, H. Siikonen, E. Tuominen, J. Tuominiemi

Lappeenranta University of Technology, Lappeenranta, Finland

P. Luukka, T. Tuuva

IRFU, CEA, Université Paris-Saclay, Gif-sur-Yvette, France

M. Besancon, F. Couderc, M. Dejardin, D. Denegri, B. Fabbro, J.L. Faure, F. Ferri, S. Ganjour, A. Givernaud, P. Gras, G. Hamel de Monchenault, P. Jarry, C. Leloup, B. Lenzi, E. Locci, J. Malcles, J. Rander, A. Rosowsky, M.Ö. Sahin, A. Savoy-Navarro[13], M. Titov, G.B. Yu

Laboratoire Leprince-Ringuet, CNRS/IN2P3, Ecole Polytechnique, Institut Polytechnique de Paris, Paris, France

S. Ahuja, C. Amendola, F. Beaudette, M. Bonanomi, P. Busson, C. Charlot, B. Diab, G. Falmagne, R. Granier de Cassagnac, I. Kucher, A. Lobanov, C. Martin Perez, M. Nguyen, C. Ochando, P. Paganini, J. Rembser, R. Salerno, J.B. Sauvan, Y. Sirois, A. Zabi, A. Zghiche

Université de Strasbourg, CNRS, IPHC UMR 7178, Strasbourg, France

J.-L. Agram[14], J. Andrea, D. Bloch, G. Bourgatte, J.-M. Brom, E.C. Chabert, C. Collard, E. Conte[14], J.-C. Fontaine[14], D. Gelé, U. Goerlach, C. Grimault, A.-C. Le Bihan, N. Tonon, P. Van Hove

Centre de Calcul de l'Institut National de Physique Nucleaire et de Physique des Particules, CNRS/IN2P3, Villeurbanne, France

S. Gadrat

Université de Lyon, Université Claude Bernard Lyon 1, CNRS-IN2P3, Institut de Physique Nucléaire de Lyon, Villeurbanne, France

S. Beauceron, C. Bernet, G. Boudoul, C. Camen, A. Carle, N. Chanon, R. Chierici, D. Contardo, P. Depasse, H. El Mamouni, J. Fay, S. Gascon, M. Gouzevitch, B. Ille, Sa. Jain, I.B. Laktineh, H. Lattaud, A. Lesauvage, M. Lethuillier, L. Mirabito, S. Perries, V. Sordini, L. Torterotot, G. Touquet, M. Vander Donckt, S. Viret

2020 JINST 15 P10017

Georgian Technical University, Tbilisi, Georgia
G. Adamov

Tbilisi State University, Tbilisi, Georgia
Z. Tsamalaidze[10]

RWTH Aachen University, I. Physikalisches Institut, Aachen, Germany
C. Autermann, L. Feld, K. Klein, M. Lipinski, D. Meuser, A. Pauls, M. Preuten, M.P. Rauch, J. Schulz, M. Teroerde

RWTH Aachen University, III. Physikalisches Institut A, Aachen, Germany
M. Erdmann, B. Fischer, S. Ghosh, T. Hebbeker, K. Hoepfner, H. Keller, L. Mastrolorenzo, M. Merschmeyer, A. Meyer, P. Millet, G. Mocellin, S. Mondal, S. Mukherjee, D. Noll, A. Novak, T. Pook, A. Pozdnyakov, T. Quast, M. Radziej, Y. Rath, H. Reithler, J. Roemer, A. Schmidt, S.C. Schuler, A. Sharma, S. Wiedenbeck, S. Zaleski

RWTH Aachen University, III. Physikalisches Institut B, Aachen, Germany
G. Flügge, W. Haj Ahmad[15], O. Hlushchenko, T. Kress, T. Müller, A. Nowack, C. Pistone, O. Pooth, D. Roy, H. Sert, A. Stahl[16]

Deutsches Elektronen-Synchrotron, Hamburg, Germany
M. Aldaya Martin, P. Asmuss, I. Babounikau, H. Bakhshiansohi, K. Beernaert, O. Behnke, A. Bermúdez Martínez, A.A. Bin Anuar, K. Borras[17], V. Botta, A. Campbell, A. Cardini, P. Connor, S. Consuegra Rodríguez, C. Contreras-Campana, V. Danilov, A. De Wit, M.M. Defranchis, C. Diez Pardos, D. Domínguez Damiani, G. Eckerlin, D. Eckstein, T. Eichhorn, A. Elwood, E. Eren, L.I. Estevez Banos, E. Gallo[18], A. Geiser, A. Grohsjean, M. Guthoff, M. Haranko, A. Harb, A. Jafari, N.Z. Jomhari, H. Jung, A. Kasem[17], M. Kasemann, H. Kaveh, J. Keaveney, C. Kleinwort, J. Knolle, D. Krücker, W. Lange, T. Lenz, J. Lidrych, K. Lipka, W. Lohmann[19], R. Mankel, I.-A. Melzer-Pellmann, A.B. Meyer, M. Meyer, M. Missiroli, J. Mnich, A. Mussgiller, V. Myronenko, D. Pérez Adán, S.K. Pflitsch, D. Pitzl, A. Raspereza, A. Saibel, M. Savitskyi, V. Scheurer, P. Schütze, C. Schwanenberger, R. Shevchenko, A. Singh, R.E. Sosa Ricardo, H. Tholen, O. Turkot, A. Vagnerini, M. Van De Klundert, R. Walsh, Y. Wen, K. Wichmann, C. Wissing, O. Zenaiev, R. Zlebcik

University of Hamburg, Hamburg, Germany
R. Aggleton, S. Bein, L. Benato, A. Benecke, T. Dreyer, A. Ebrahimi, F. Feindt, A. Fröhlich, C. Garbers, E. Garutti, D. Gonzalez, P. Gunnellini, J. Haller, A. Hinzmann, A. Karavdina, G. Kasieczka, R. Klanner, R. Kogler, N. Kovalchuk, S. Kurz, V. Kutzner, J. Lange, T. Lange, A. Malara, J. Multhaup, C.E.N. Niemeyer, A. Reimers, O. Rieger, P. Schleper, S. Schumann, J. Schwandt, J. Sonneveld, H. Stadie, G. Steinbrück, B. Vormwald, I. Zoi

Karlsruher Institut fuer Technologie, Karlsruhe, Germany
M. Akbiyik, M. Baselga, S. Baur, T. Berger, E. Butz, R. Caspart, T. Chwalek, W. De Boer, A. Dierlamm, K. El Morabit, N. Faltermann, M. Giffels, A. Gottmann, F. Hartmann[16], C. Heidecker, U. Husemann, M.A. Iqbal, S. Kudella, S. Maier, S. Mitra, M.U. Mozer, D. Müller, Th. Müller, M. Musich, A. Nürnberg, G. Quast, K. Rabbertz, D. Savoiu, D. Schäfer, M. Schnepf, M. Schröder, I. Shvetsov, H.J. Simonis, R. Ulrich, M. Wassmer, M. Weber, C. Wöhrmann, R. Wolf, S. Wozniewski

2020 JINST 15 P10017

Institute of Nuclear and Particle Physics (INPP), NCSR Demokritos, Aghia Paraskevi, Greece

G. Anagnostou, P. Asenov, G. Daskalakis, T. Geralis, A. Kyriakis, D. Loukas, G. Paspalaki, A. Stakia

National and Kapodistrian University of Athens, Athens, Greece

M. Diamantopoulou, G. Karathanasis, P. Kontaxakis, C.K. Koraka, A. Manousakis-katsikakis, A. Panagiotou, I. Papavergou, N. Saoulidou, S. Sotiropoulos, K. Theofilatos, K. Vellidis, E. Vourliotis

National Technical University of Athens, Athens, Greece

G. Bakas, K. Kousouris, I. Papakrivopoulos, G. Tsipolitis, A. Zacharopoulou

University of Ioánnina, Ioánnina, Greece

I. Evangelou, C. Foudas, P. Gianneios, P. Katsoulis, P. Kokkas, S. Mallios, K. Manitara, N. Manthos, I. Papadopoulos, J. Strologas, F.A. Triantis, D. Tsitsonis

MTA-ELTE Lendület CMS Particle and Nuclear Physics Group, Eötvös Loránd University, Budapest, Hungary

M. Bartók[20], R. Chudasama, M. Csanad, P. Major, K. Mandal, A. Mehta, G. Pasztor, O. Surányi, G.I. Veres

Wigner Research Centre for Physics, Budapest, Hungary

G. Bencze, C. Hajdu, D. Horvath[21], F. Sikler, V. Veszpremi, G. Vesztergombi[†]

Institute of Nuclear Research ATOMKI, Debrecen, Hungary

N. Beni, S. Czellar, J. Karancsi[20], J. Molnar, Z. Szillasi

Institute of Physics, University of Debrecen, Debrecen, Hungary

P. Raics, D. Teyssier, B. Ujvari, G. Zilizi

Eszterhazy Karoly University, Karoly Robert Campus, Gyongyos, Hungary

T. Csorgo, S. Lökös, W.J. Metzger, F. Nemes, T. Novak

Indian Institute of Science (IISc), Bangalore, India

S. Choudhury, J.R. Komaragiri, L. Panwar, P.C. Tiwari

National Institute of Science Education and Research, HBNI, Bhubaneswar, India

S. Bahinipati[23], A.K. Das, C. Kar, G. Kole, P. Mal, V.K. Muraleedharan Nair Bindhu, A. Nayak[24], D.K. Sahoo[23], S.K. Swain

Panjab University, Chandigarh, India

S. Bansal, S.B. Beri, V. Bhatnagar, S. Chauhan, N. Dhingra[25], R. Gupta, A. Kaur, M. Kaur, S. Kaur, P. Kumari, M. Lohan, M. Meena, K. Sandeep, S. Sharma, J.B. Singh, A.K. Virdi

University of Delhi, Delhi, India

A. Bhardwaj, B.C. Choudhary, R.B. Garg, M. Gola, S. Keshri, A. Kumar, M. Naimuddin, P. Priyanka, K. Ranjan, A. Shah, R. Sharma

2020 JINST 15 P10017

Saha Institute of Nuclear Physics, HBNI, Kolkata, India

R. Bhardwaj[26], M. Bharti[26], R. Bhattacharya, S. Bhattacharya, U. Bhawandeep[26], D. Bhowmik, S. Dutta, S. Ghosh, B. Gomber[27], M. Maity[28], K. Mondal, S. Nandan, A. Purohit, P.K. Rout, G. Saha, S. Sarkar, M. Sharan, B. Singh[26], S. Thakur[26]

Indian Institute of Technology Madras, Madras, India

P.K. Behera, S.C. Behera, P. Kalbhor, A. Muhammad, R. Pradhan, P.R. Pujahari, A. Sharma, A.K. Sikdar

Bhabha Atomic Research Centre, Mumbai, India

D. Dutta, V. Jha, D.K. Mishra, P.K. Netrakanti, L.M. Pant, P. Shukla

Tata Institute of Fundamental Research-A, Mumbai, India

T. Aziz, M.A. Bhat, S. Dugad, R. Kumar Verma, G.B. Mohanty, N. Sur

Tata Institute of Fundamental Research-B, Mumbai, India

S. Banerjee, S. Bhattacharya, S. Chatterjee, P. Das, M. Guchait, S. Karmakar, S. Kumar, G. Majumder, K. Mazumdar, N. Sahoo, S. Sawant

Indian Institute of Science Education and Research (IISER), Pune, India

S. Dube, B. Kansal, A. Kapoor, K. Kothekar, S. Pandey, A. Rane, A. Rastogi, S. Sharma

Institute for Research in Fundamental Sciences (IPM), Tehran, Iran

S. Chenarani, S.M. Etesami, M. Khakzad, M. Mohammadi Najafabadi, M. Naseri, F. Rezaei Hosseinabadi

University College Dublin, Dublin, Ireland

M. Felcini, M. Grunewald

INFN Sezione di Bari [a], Università di Bari [b], Politecnico di Bari [c], Bari, Italy

M. Abbrescia[a,b], R. Aly[a,b,29], C. Calabria[a,b], A. Colaleo[a], D. Creanza[a,c], L. Cristella[a,b], N. De Filippis[a,c], M. De Palma[a,b], A. Di Florio[a,b], W. Elmetenawee[a,b], L. Fiore[a], A. Gelmi[a,b], G. Iaselli[a,c], M. Ince[a,b], S. Lezki[a,b], G. Maggi[a,c], M. Maggi[a], J.A. Merlin[a], G. Miniello[a,b], S. My[a,b], S. Nuzzo[a,b], A. Pompili[a,b], G. Pugliese[a,c], R. Radogna[a], A. Ranieri[a], G. Selvaggi[a,b], L. Silvestris[a], F.M. Simone[a,b], R. Venditti[a], P. Verwilligen[a]

INFN Sezione di Bologna [a], Università di Bologna [b], Bologna, Italy

G. Abbiendi[a], C. Battilana[a,b], D. Bonacorsi[a,b], L. Borgonovi[a,b], S. Braibant-Giacomelli[a,b], R. Campanini[a,b], P. Capiluppi[a,b], A. Castro[a,b], F.R. Cavallo[a], C. Ciocca[a], G. Codispoti[a,b], M. Cuffiani[a,b], G.M. Dallavalle[a], F. Fabbri[a], A. Fanfani[a,b], E. Fontanesi[a,b], P. Giacomelli[a], C. Grandi[a], L. Guiducci[a,b], F. Iemmi[a,b], S. Lo Meo[a,30], S. Marcellini[a], G. Masetti[a], F.L. Navarria[a,b], A. Perrotta[a], F. Primavera[a,b], A.M. Rossi[a,b], T. Rovelli[a,b], G.P. Siroli[a,b], N. Tosi[a]

INFN Sezione di Catania [a], Università di Catania [b], Catania, Italy

S. Albergo[a,b,31], S. Costa[a,b], A. Di Mattia[a], R. Potenza[a,b], A. Tricomi[a,b,31], C. Tuve[a,b]

2020 JINST 15 P10017

INFN Sezione di Firenze [a], Università di Firenze [b], Firenze, Italy

G. Barbagli[a], A. Cassese[a], R. Ceccarelli[a,b], V. Ciulli[a,b], C. Civinini[a], R. D'Alessandro[a,b], F. Fiori[a], E. Focardi[a,b], G. Latino[a,b], P. Lenzi[a,b], M. Lizzo[a,b], M. Meschini[a], S. Paoletti[a], R. Seidita[a,b], G. Sguazzoni[a], L. Viliani[a]

INFN Laboratori Nazionali di Frascati, Frascati, Italy

L. Benussi, S. Bianco, D. Piccolo

INFN Sezione di Genova [a], Università di Genova [b], Genova, Italy

M. Bozzo[a,b], F. Ferro[a], R. Mulargia[a,b], E. Robutti[a], S. Tosi[a,b]

INFN Sezione di Milano-Bicocca [a], Università di Milano-Bicocca [b], Milano, Italy

A. Benaglia[a], A. Beschi[a,b], F. Brivio[a,b], V. Ciriolo[a,b,16], F. De Guio[a,b], M.E. Dinardo[a,b], P. Dini[a], S. Gennai[a], A. Ghezzi[a,b], P. Govoni[a,b], L. Guzzi[a,b], M. Malberti[a], S. Malvezzi[a], D. Menasce[a], F. Monti[a,b], L. Moroni[a], M. Paganoni[a,b], D. Pedrini[a], S. Ragazzi[a,b], T. Tabarelli de Fatis[a,b], D. Valsecchi[a,b,16], D. Zuolo[a,b]

INFN Sezione di Napoli [a], Università di Napoli 'Federico II' [b], Napoli, Italy, Università della Basilicata [c], Potenza, Italy, Università G. Marconi [d], Roma, Italy

S. Buontempo[a], N. Cavallo[a,c], A. De Iorio[a,b], A. Di Crescenzo[a,b], F. Fabozzi[a,c], F. Fienga[a], G. Galati[a], A.O.M. Iorio[a,b], L. Layer[a,b], L. Lista[a,b], S. Meola[a,d,16], P. Paolucci[a,16], B. Rossi[a], C. Sciacca[a,b], E. Voevodina[a,b]

INFN Sezione di Padova [a], Università di Padova [b], Padova, Italy, Università di Trento [c], Trento, Italy

P. Azzi[a], N. Bacchetta[a], L. Barcellan[a], M. Bellato[a], M. Benettoni[a], A. Bergnoli[a], D. Bisello[a,b], A. Boletti[a,b], A. Bragagnolo[a,b], R. Carlin[a,b], L. Castellani[a], P. Checchia[a], L. Ciano[a], D. Corti, P. De Castro Manzano[a], T. Dorigo[a], U. Dosselli[a], F. Fanzago[a], F. Gasparini[a,b], U. Gasparini[a,b], F. Gonella[a], A. Gozzelino[a], A. Griggio, S.Y. Hoh[a,b], R. Isocrate[a], M. Margoni[a,b], A.T. Meneguzzo[a,b], L. Modenese[a], F. Montecassiano[a], M. Passaseo[a], J. Pazzini[a,b], M. Presilla[b], P. Ronchese[a,b], R. Rossin[a,b], F. Simonetto[a,b], A. Tiko[a], M. Tosi[a,b], S. Ventura[a], M. Zanetti[a,b], P. Zotto[a,b], A. Zucchetta[a,b], G. Zumerle[a,b]

INFN Sezione di Pavia [a], Università di Pavia [b], Pavia, Italy

A. Braghieri[a], D. Fiorina[a,b], P. Montagna[a,b], S.P. Ratti[a,b], V. Re[a], M. Ressegotti[a,b], C. Riccardi[a,b], P. Salvini[a], I. Vai[a], P. Vitulo[a,b]

INFN Sezione di Perugia [a], Università di Perugia [b], Perugia, Italy

M. Biasini[a,b], G.M. Bilei[a], D. Ciangottini[a,b], L. Fanò[a,b], P. Lariccia[a,b], R. Leonardi[a,b], E. Manoni[a], G. Mantovani[a,b], V. Mariani[a,b], M. Menichelli[a], A. Rossi[a,b], A. Santocchia[a,b], D. Spiga[a]

INFN Sezione di Pisa [a], Università di Pisa [b], Scuola Normale Superiore di Pisa [c], Pisa, Italy

K. Androsov[a], P. Azzurri[a], G. Bagliesi[a], V. Bertacchi[a,c], L. Bianchini[a], T. Boccali[a], R. Castaldi[a], M.A. Ciocci[a,b], R. Dell'Orso[a], S. Donato[a], L. Giannini[a,c], A. Giassi[a], M.T. Grippo[a], F. Ligabue[a,c], E. Manca[a,c], G. Mandorli[a,c], A. Messineo[a,b], F. Palla[a], A. Rizzi[a,b], G. Rolandi[a,c],

2020 JINST 15 P10017

S. Roy Chowdhury[a,c], A. Scribano[a], P. Spagnolo[a], R. Tenchini[a], G. Tonelli[a,b], N. Turini[a], A. Venturi[a], P.G. Verdini[a]

INFN Sezione di Roma [a], Sapienza Università di Roma [b], Rome, Italy

F. Cavallari[a], M. Cipriani[a,b], D. Del Re[a,b], E. Di Marco[a], M. Diemoz[a], E. Longo[a,b], P. Meridiani[a], G. Organtini[a,b], F. Pandolfi[a], R. Paramatti[a,b], C. Quaranta[a,b], S. Rahatlou[a,b], C. Rovelli[a], F. Santanastasio[a,b], L. Soffi[a,b], R. Tramontano[a,b]

INFN Sezione di Torino [a], Università di Torino [b], Torino, Italy, Università del Piemonte Orientale [c], Novara, Italy

N. Amapane[a,b], R. Arcidiacono[a,c], S. Argiro[a,b], M. Arneodo[a,c], N. Bartosik[a], R. Bellan[a,b], A. Bellora[a,b], C. Biino[a], A. Cappati[a,b], N. Cartiglia[a], S. Cometti[a], M. Costa[a,b], R. Covarelli[a,b], N. Demaria[a], J.R. González Fernández[a], B. Kiani[a,b], F. Legger[a], C. Mariotti[a], S. Maselli[a], E. Migliore[a,b], V. Monaco[a,b], E. Monteil[a,b], M. Monteno[a], M.M. Obertino[a,b], G. Ortona[a], L. Pacher[a,b], N. Pastrone[a], M. Pelliccioni[a], G.L. Pinna Angioni[a,b], A. Romero[a,b], M. Ruspa[a,c], R. Salvatico[a,b], V. Sola[a], A. Solano[a,b], D. Soldi[a,b], A. Staiano[a], D. Trocino[a,b]

INFN Sezione di Trieste [a], Università di Trieste [b], Trieste, Italy

S. Belforte[a], V. Candelise[a,b], M. Casarsa[a], F. Cossutti[a], A. Da Rold[a,b], G. Della Ricca[a,b], F. Vazzoler[a,b], A. Zanetti[a]

Kyungpook National University, Daegu, Korea

B. Kim, D.H. Kim, G.N. Kim, J. Lee, S.W. Lee, C.S. Moon, Y.D. Oh, S.I. Pak, S. Sekmen, D.C. Son, Y.C. Yang

Chonnam National University, Institute for Universe and Elementary Particles, Kwangju, Korea

H. Kim, D.H. Moon

Hanyang University, Seoul, Korea

B. Francois, T.J. Kim, J. Park

Korea University, Seoul, Korea

S. Cho, S. Choi, Y. Go, S. Ha, B. Hong, K. Lee, K.S. Lee, J. Lim, J. Park, S.K. Park, Y. Roh, J. Yoo

Kyung Hee University, Department of Physics, Seoul, Republic of Korea

J. Goh

Sejong University, Seoul, Korea

H.S. Kim

Seoul National University, Seoul, Korea

J. Almond, J.H. Bhyun, J. Choi, S. Jeon, J. Kim, J.S. Kim, H. Lee, K. Lee, S. Lee, K. Nam, M. Oh, S.B. Oh, B.C. Radburn-Smith, U.K. Yang, H.D. Yoo, I. Yoon

University of Seoul, Seoul, Korea

D. Jeon, J.H. Kim, J.S.H. Lee, I.C. Park, I.J. Watson

Sungkyunkwan University, Suwon, Korea

Y. Choi, C. Hwang, Y. Jeong, J. Lee, Y. Lee, I. Yu

2020 JINST 15 P10017

Riga Technical University, Riga, Latvia
V. Veckalns[32]

Vilnius University, Vilnius, Lithuania
V. Dudenas, A. Juodagalvis, A. Rinkevicius, G. Tamulaitis, J. Vaitkus

National Centre for Particle Physics, Universiti Malaya, Kuala Lumpur, Malaysia
F. Mohamad Idris[33], W.A.T. Wan Abdullah, M.N. Yusli, Z. Zolkapli

Universidad de Sonora (UNISON), Hermosillo, Mexico
J.F. Benitez, A. Castaneda Hernandez, J.A. Murillo Quijada, L. Valencia Palomo

Centro de Investigacion y de Estudios Avanzados del IPN, Mexico City, Mexico
H. Castilla-Valdez, E. De La Cruz-Burelo, I. Heredia-De La Cruz[34], R. Lopez-Fernandez, A. Sanchez-Hernandez

Universidad Iberoamericana, Mexico City, Mexico
S. Carrillo Moreno, C. Oropeza Barrera, M. Ramirez-Garcia, F. Vazquez Valencia

Benemerita Universidad Autonoma de Puebla, Puebla, Mexico
J. Eysermans, I. Pedraza, H.A. Salazar Ibarguen, C. Uribe Estrada

Universidad Autónoma de San Luis Potosí, San Luis Potosí, Mexico
A. Morelos Pineda

University of Montenegro, Podgorica, Montenegro
J. Mijuskovic[3], N. Raicevic

University of Auckland, Auckland, New Zealand
D. Krofcheck

University of Canterbury, Christchurch, New Zealand
S. Bheesette, P.H. Butler, P. Lujan

National Centre for Physics, Quaid-I-Azam University, Islamabad, Pakistan
A. Ahmad, M. Ahmad, M.I.M. Awan, Q. Hassan, H.R. Hoorani, W.A. Khan, M.A. Shah, M. Shoaib, M. Waqas

AGH University of Science and Technology Faculty of Computer Science, Electronics and Telecommunications, Krakow, Poland
V. Avati, L. Grzanka, M. Malawski

National Centre for Nuclear Research, Swierk, Poland
H. Bialkowska, M. Bluj, B. Boimska, M. Górski, M. Kazana, M. Szleper, P. Zalewski

Institute of Experimental Physics, Faculty of Physics, University of Warsaw, Warsaw, Poland
K. Bunkowski, A. Byszuk[35], K. Doroba, A. Kalinowski, K. Kierzkowski, M. Konecki, J. Krolikowski, W. Oklinski, M. Olszewski, K. Pozniak[35], M. Walczak, W. Zabolotny[35]

Laboratório de Instrumentação e Física Experimental de Partículas, Lisboa, Portugal
M. Araujo, P. Bargassa, D. Bastos, A. Di Francesco, P. Faccioli, B. Galinhas, M. Gallinaro, J. Hollar, N. Leonardo, T. Niknejad, J. Seixas, K. Shchelina, G. Strong, O. Toldaiev, J. Varela

2020 JINST 15 P10017

Joint Institute for Nuclear Research, Dubna, Russia

S. Afanasiev, P. Bunin, M. Gavrilenko, I. Golutvin, I. Gorbunov, A. Kamenev, V. Karjavine, A. Lanev, A. Malakhov, V. Matveev[36,37], P. Moisenz, V. Palichik, V. Perelygin, M. Savina, S. Shmatov, S. Shulha, N. Skatchkov, V. Smirnov, N. Voytishin, A. Zarubin

Petersburg Nuclear Physics Institute, Gatchina (St. Petersburg), Russia

L. Chtchipounov, V. Golovtcov, Y. Ivanov, V. Kim[38], E. Kuznetsova[39], P. Levchenko, V. Murzin, V. Oreshkin, I. Smirnov, D. Sosnov, V. Sulimov, L. Uvarov, A. Vorobyev

Institute for Nuclear Research, Moscow, Russia

Yu. Andreev, A. Dermenev, S. Gninenko, N. Golubev, A. Karneyeu, M. Kirsanov, N. Krasnikov, A. Pashenkov, D. Tlisov, A. Toropin

Institute for Theoretical and Experimental Physics named by A.I. Alikhanov of NRC 'Kurchatov Institute', Moscow, Russia

V. Epshteyn, V. Gavrilov, N. Lychkovskaya, A. Nikitenko[40], V. Popov, I. Pozdnyakov, G. Safronov, A. Spiridonov, A. Stepennov, M. Toms, E. Vlasov, A. Zhokin

Moscow Institute of Physics and Technology, Moscow, Russia

T. Aushev

National Research Nuclear University 'Moscow Engineering Physics Institute' (MEPhI), Moscow, Russia

M. Chadeeva[41], P. Parygin, S. Polikarpov[41], E. Popova, V. Rusinov

P.N. Lebedev Physical Institute, Moscow, Russia

V. Andreev, M. Azarkin, I. Dremin, M. Kirakosyan, A. Terkulov

Skobeltsyn Institute of Nuclear Physics, Lomonosov Moscow State University, Moscow, Russia

A. Belyaev, E. Boos, M. Dubinin[42], L. Dudko, A. Ershov, A. Gribushin, A. Kaminskiy[43], V. Klyukhin, O. Kodolova, I. Lokhtin, S. Obraztsov, S. Petrushanko, V. Savrin

Novosibirsk State University (NSU), Novosibirsk, Russia

A. Barnyakov[44], V. Blinov[44], T. Dimova[44], L. Kardapoltsev[44], I. Ovtin[44], Y. Skovpen[44]

Institute for High Energy Physics of National Research Centre 'Kurchatov Institute', Protvino, Russia

I. Azhgirey, I. Bayshev, S. Bitioukov, V. Kachanov, D. Konstantinov, P. Mandrik, V. Petrov, R. Ryutin, S. Slabospitskii, A. Sobol, S. Troshin, N. Tyurin, A. Uzunian, A. Volkov

National Research Tomsk Polytechnic University, Tomsk, Russia

A. Babaev, A. Iuzhakov, V. Okhotnikov

Tomsk State University, Tomsk, Russia

V. Borchsh, V. Ivanchenko, E. Tcherniaev

University of Belgrade: Faculty of Physics and VINCA Institute of Nuclear Sciences, Belgrade, Serbia

P. Adzic[45], P. Cirkovic, M. Dordevic, P. Milenovic, J. Milosevic, V. Rekovic[39], M. Stojanovic

2020 JINST 15 P10017

Centro de Investigaciones Energéticas Medioambientales y Tecnológicas (CIEMAT), Madrid, Spain

M. Aguilar-Benitez, J. Alcaraz Maestre, A. Álvarez Fernández, I. Bachiller, M. Barrio Luna, Cristina F. Bedoya, J.A. Brochero Cifuentes, C.A. Carrillo Montoya, M. Cepeda, M. Cerrada, N. Colino, B. De La Cruz, A. Delgado Peris, J.P. Fernández Ramos, J. Flix, M.C. Fouz, O. Gonzalez Lopez, S. Goy Lopez, J.M. Hernandez, M.I. Josa, D. Moran, Á. Navarro Tobar, A. Pérez-Calero Yzquierdo, J. Puerta Pelayo, I. Redondo, L. Romero, S. Sánchez Navas, M.S. Soares, A. Triossi, C. Willmott

Universidad Autónoma de Madrid, Madrid, Spain

C. Albajar, J.F. de Trocóniz, R. Reyes-Almanza

Universidad de Oviedo, Instituto Universitario de Ciencias y Tecnologías Espaciales de Asturias (ICTEA), Oviedo, Spain

B. Alvarez Gonzalez, J. Cuevas, C. Erice, J. Fernandez Menendez, S. Folgueras, I. Gonzalez Caballero, E. Palencia Cortezon, C. Ramón Álvarez, V. Rodríguez Bouza, S. Sanchez Cruz

Instituto de Física de Cantabria (IFCA), CSIC-Universidad de Cantabria, Santander, Spain

I.J. Cabrillo, A. Calderon, B. Chazin Quero, J. Duarte Campderros, M. Fernandez, P.J. Fernández Manteca, A. García Alonso, G. Gomez, C. Martinez Rivero, P. Martinez Ruiz del Arbol, F. Matorras, J. Piedra Gomez, C. Prieels, F. Ricci-Tam, T. Rodrigo, A. Ruiz-Jimeno, L. Russo[46], L. Scodellaro, I. Vila, J.M. Vizan Garcia

University of Colombo, Colombo, Sri Lanka

D.U.J. Sonnadara

University of Ruhuna, Department of Physics, Matara, Sri Lanka

W.G.D. Dharmaratna, N. Wickramage

CERN, European Organization for Nuclear Research, Geneva, Switzerland

T.K. Aarrestad, D. Abbaneo, B. Akgun, E. Auffray, G. Auzinger, J. Baechler, P. Baillon, A.H. Ball, D. Barney, J. Bendavid, M. Bianco, A. Bocci, P. Bortignon, E. Bossini, E. Brondolin, T. Camporesi, A. Caratelli, G. Cerminara, E. Chapon, G. Cucciati, D. d'Enterria, A. Dabrowski, N. Daci, V. Daponte, A. David, O. Davignon, A. De Roeck, M. Deile, R. Di Maria, M. Dobson, M. Dünser, N. Dupont, A. Elliott-Peisert, N. Emriskova, F. Fallavollita[47], D. Fasanella, S. Fiorendi, G. Franzoni, J. Fulcher, W. Funk, S. Giani, D. Gigi, K. Gill, F. Glege, L. Gouskos, M. Gruchala, M. Guilbaud, D. Gulhan, J. Hegeman, C. Heidegger, Y. Iiyama, V. Innocente, T. James, P. Janot, O. Karacheban[19], J. Kaspar, J. Kieseler, M. Krammer[1], N. Kratochwil, C. Lange, P. Lecoq, K. Long, C. Lourenço, L. Malgeri, M. Mannelli, A. Massironi, F. Meijers, S. Mersi, E. Meschi, F. Moortgat, M. Mulders, J. Ngadiuba, J. Niedziela, S. Nourbakhsh, S. Orfanelli, L. Orsini, F. Pantaleo[16], L. Pape, E. Perez, M. Peruzzi, A. Petrilli, G. Petrucciani, A. Pfeiffer, M. Pierini, F.M. Pitters, D. Rabady, A. Racz, M. Rieger, M. Rovere, H. Sakulin, J. Salfeld-Nebgen, S. Scarfi, C. Schäfer, C. Schwick, M. Selvaggi, A. Sharma, P. Silva, W. Snoeys, P. Sphicas[48], J. Steggemann, S. Summers, V.R. Tavolaro, D. Treille, A. Tsirou, G.P. Van Onsem, A. Vartak, M. Verzetti, K.A. Wozniak, W.D. Zeuner

Paul Scherrer Institut, Villigen, Switzerland

L. Caminada[49], K. Deiters, W. Erdmann, R. Horisberger, Q. Ingram, H.C. Kaestli, D. Kotlinski, U. Langenegger, T. Rohe

2020 JINST 15 P10017

ETH Zurich — Institute for Particle Physics and Astrophysics (IPA), Zurich, Switzerland

M. Backhaus, P. Berger, A. Calandri, N. Chernyavskaya, G. Dissertori, M. Dittmar, M. Donegà, C. Dorfer, T.A. Gómez Espinosa, C. Grab, D. Hits, W. Lustermann, R.A. Manzoni, M.T. Meinhard, F. Micheli, P. Musella, F. Nessi-Tedaldi, F. Pauss, V. Perovic, G. Perrin, L. Perrozzi, S. Pigazzini, M.G. Ratti, M. Reichmann, C. Reissel, T. Reitenspiess, B. Ristic, D. Ruini, D.A. Sanz Becerra, M. Schönenberger, L. Shchutska, M.L. Vesterbacka Olsson, R. Wallny, D.H. Zhu

Universität Zürich, Zurich, Switzerland

C. Amsler[50], C. Botta, D. Brzhechko, M.F. Canelli, A. De Cosa, R. Del Burgo, B. Kilminster, S. Leontsinis, V.M. Mikuni, I. Neutelings, G. Rauco, P. Robmann, K. Schweiger, Y. Takahashi, S. Wertz

National Central University, Chung-Li, Taiwan

C.M. Kuo, W. Lin, A. Roy, T. Sarkar[28], S.S. Yu

National Taiwan University (NTU), Taipei, Taiwan

P. Chang, Y. Chao, K.F. Chen, P.H. Chen, W.-S. Hou, Y.y. Li, R.-S. Lu, E. Paganis, A. Psallidas, A. Steen

Chulalongkorn University, Faculty of Science, Department of Physics, Bangkok, Thailand

B. Asavapibhop, C. Asawatangtrakuldee, N. Srimanobhas, N. Suwonjandee

Çukurova University, Physics Department, Science and Art Faculty, Adana, Turkey

A. Bat, F. Boran, A. Celik[51], S. Damarseckin[52], Z.S. Demiroglu, F. Dolek, C. Dozen[53], I. Dumanoglu[54], G. Gokbulut, Y. Guler, E. Gurpinar Guler[55], I. Hos[56], C. Isik, E.E. Kangal[57], O. Kara, A. Kayis Topaksu, U. Kiminsu, G. Onengut, K. Ozdemir[58], A.E. Simsek, U.G. Tok, S. Turkcapar, I.S. Zorbakir, C. Zorbilmez

Middle East Technical University, Physics Department, Ankara, Turkey

B. Isildak[59], G. Karapinar[60], M. Yalvac[61]

Bogazici University, Istanbul, Turkey

I.O. Atakisi, E. Gülmez, M. Kaya[62], O. Kaya[63], Ö. Özçelik, S. Tekten[64], E.A. Yetkin[65]

Istanbul Technical University, Istanbul, Turkey

A. Cakir, K. Cankocak[54], Y. Komurcu, S. Sen[66]

Istanbul University, Istanbul, Turkey

S. Cerci[67], B. Kaynak, S. Ozkorucuklu, D. Sunar Cerci[67]

Institute for Scintillation Materials of National Academy of Science of Ukraine, Kharkov, Ukraine

B. Grynyov

National Scientific Center, Kharkov Institute of Physics and Technology, Kharkov, Ukraine

L. Levchuk

2020 JINST 15 P10017

University of Bristol, Bristol, United Kingdom

E. Bhal, S. Bologna, J.J. Brooke, D. Burns[68], E. Clement, D. Cussans, H. Flacher, J. Goldstein, G.P. Heath, H.F. Heath, L. Kreczko, B. Krikler, S. Paramesvaran, T. Sakuma, S. Seif El Nasr-Storey, V.J. Smith, J. Taylor, A. Titterton

Rutherford Appleton Laboratory, Didcot, United Kingdom

K.W. Bell, A. Belyaev[69], C. Brew, R.M. Brown, D.J.A. Cockerill, J.A. Coughlan, K. Harder, S. Harper, J. Linacre, K. Manolopoulos, D.M. Newbold, E. Olaiya, D. Petyt, T. Reis, T. Schuh, C.H. Shepherd-Themistocleous, A. Thea, I.R. Tomalin, T. Williams

Imperial College, London, United Kingdom

R. Bainbridge, P. Bloch, S. Bonomally, J. Borg, S. Breeze, O. Buchmuller, A. Bundock, G.S. Chahal[70], D. Colling, P. Dauncey, G. Davies, M. Della Negra, P. Everaerts, G. Hall, G. Iles, M. Komm, J. Langford, L. Lyons, A.-M. Magnan, S. Malik, A. Martelli, V. Milosevic, A. Morton, J. Nash[71], V. Palladino, M. Pesaresi, D.M. Raymond, A. Richards, A. Rose, E. Scott, C. Seez, A. Shtipliyski, M. Stoye, T. Strebler, A. Tapper, K. Uchida, T. Virdee[16], N. Wardle, S.N. Webb, D. Winterbottom, A.G. Zecchinelli, S.C. Zenz

Brunel University, Uxbridge, United Kingdom

J.E. Cole, P.R. Hobson, A. Khan, P. Kyberd, C.K. Mackay, I.D. Reid, L. Teodorescu, S. Zahid

Baylor University, Waco, U.S.A.

A. Brinkerhoff, K. Call, B. Caraway, J. Dittmann, K. Hatakeyama, C. Madrid, B. McMaster, N. Pastika, C. Smith

Catholic University of America, Washington, DC, U.S.A.

R. Bartek, A. Dominguez, R. Uniyal, A.M. Vargas Hernandez

The University of Alabama, Tuscaloosa, U.S.A.

A. Buccilli, S.I. Cooper, S.V. Gleyzer, C. Henderson, P. Rumerio, C. West

Boston University, Boston, U.S.A.

A. Albert, D. Arcaro, Z. Demiragli, D. Gastler, E. Hazen, C. Richardson, J. Rohlf, D. Sperka, D. Spitzbart, I. Suarez, L. Sulak, D. Zou

Brown University, Providence, U.S.A.

G. Benelli, B. Burkle, X. Coubez[17], D. Cutts, Y.t. Duh, M. Hadley, U. Heintz, J.M. Hogan[72], K.H.M. Kwok, E. Laird, G. Landsberg, K.T. Lau, J. Lee, M. Narain, S. Sagir[73], R. Syarif, E. Usai, W.Y. Wong, D. Yu, W. Zhang

University of California, Davis, Davis, U.S.A.

R. Band, C. Brainerd, R. Breedon, M. Calderon De La Barca Sanchez, M. Chertok, J. Conway, R. Conway, P.T. Cox, R. Erbacher, C. Flores, G. Funk, F. Jensen, W. Ko[†], O. Kukral, R. Lander, M. Mulhearn, D. Pellett, J. Pilot, M. Shi, D. Taylor, K. Tos, M. Tripathi, Z. Wang, F. Zhang

University of California, Los Angeles, U.S.A.

M. Bachtis, C. Bravo, R. Cousins, A. Dasgupta, A. Florent, J. Hauser, M. Ignatenko, N. Mccoll, W.A. Nash, S. Regnard, D. Saltzberg, C. Schnaible, B. Stone, V. Valuev

2020 JINST 15 P10017

University of California, Riverside, Riverside, U.S.A.

K. Burt, Y. Chen, R. Clare, J.W. Gary, S.M.A. Ghiasi Shirazi, G. Hanson, G. Karapostoli, O.R. Long, N. Manganelli, M. Olmedo Negrete, M.I. Paneva, W. Si, S. Wimpenny, B.R. Yates, Y. Zhang

University of California, San Diego, La Jolla, U.S.A.

J.G. Branson, P. Chang, S. Cittolin, S. Cooperstein, N. Deelen, M. Derdzinski, J. Duarte, R. Gerosa, D. Gilbert, B. Hashemi, D. Klein, V. Krutelyov, J. Letts, M. Masciovecchio, S. May, S. Padhi, M. Pieri, V. Sharma, M. Tadel, F. Würthwein, A. Yagil, G. Zevi Della Porta

University of California, Santa Barbara — Department of Physics, Santa Barbara, U.S.A.

N. Amin, R. Bhandari, C. Campagnari, M. Citron, V. Dutta, J. Incandela, B. Marsh, H. Mei, A. Ovcharova, H. Qu, J. Richman, U. Sarica, D. Stuart, S. Wang

California Institute of Technology, Pasadena, U.S.A.

D. Anderson, A. Bornheim, O. Cerri, I. Dutta, J.M. Lawhorn, N. Lu, J. Mao, H.B. Newman, T.Q. Nguyen, J. Pata, M. Spiropulu, J.R. Vlimant, S. Xie, Z. Zhang, R.Y. Zhu

Carnegie Mellon University, Pittsburgh, U.S.A.

J. Alison, M.B. Andrews, T. Ferguson, T. Mudholkar, M. Paulini, M. Sun, I. Vorobiev, M. Weinberg

University of Colorado Boulder, Boulder, U.S.A.

J.P. Cumalat, W.T. Ford, E. MacDonald, T. Mulholland, R. Patel, A. Perloff, K. Stenson, K.A. Ulmer, S.R. Wagner

Cornell University, Ithaca, U.S.A.

J. Alexander, Y. Cheng, J. Chu, A. Datta, A. Frankenthal, K. Mcdermott, J.R. Patterson, D. Quach, A. Ryd, S.M. Tan, Z. Tao, J. Thom, P. Wittich, M. Zientek

Fermi National Accelerator Laboratory, Batavia, U.S.A.

S. Abdullin, M. Albrow, M. Alyari, G. Apollinari, A. Apresyan, A. Apyan, S. Banerjee, L.A.T. Bauerdick, A. Beretvas, D. Berry, J. Berryhill, P.C. Bhat, K. Burkett, J.N. Butler, A. Canepa, G.B. Cerati, H.W.K. Cheung, F. Chlebana, M. Cremonesi, V.D. Elvira, J. Freeman, Z. Gecse, E. Gottschalk, L. Gray, D. Green, S. Grünendahl, O. Gutsche, J. Hanlon, R.M. Harris, S. Hasegawa, R. Heller, J. Hirschauer, B. Jayatilaka, S. Jindariani, M. Johnson, U. Joshi, T. Klijnsma, B. Klima, M.J. Kortelainen, B. Kreis, S. Lammel, J. Lewis, D. Lincoln, R. Lipton, M. Liu, T. Liu, J. Lykken, K. Maeshima, J.M. Marraffino, D. Mason, P. McBride, P. Merkel, S. Mrenna, S. Nahn, V. O'Dell, V. Papadimitriou, K. Pedro, C. Pena[42], F. Ravera, A. Reinsvold Hall, L. Ristori, B. Schneider, E. Sexton-Kennedy, N. Smith, A. Soha, W.J. Spalding, L. Spiegel, S. Stoynev, J. Strait, L. Taylor, S. Tkaczyk, N.V. Tran, L. Uplegger, E.W. Vaandering, R. Vidal, M. Wang, H.A. Weber, A. Woodard

University of Florida, Gainesville, U.S.A.

D. Acosta, P. Avery, D. Bourilkov, L. Cadamuro, A. Carnes, V. Cherepanov, F. Errico, R.D. Field, I.K. Furic, D. Guerrero, B.M. Joshi, M. Kim, J. Konigsberg, A. Korytov, K.H. Lo, J.F. Low, A. Madorsky, K. Matchev, N. Menendez, G. Mitselmakher, D. Rosenzweig, K. Shi, J. Wang, S. Wang, X. Zuo

Florida International University, Miami, U.S.A.

Y.R. Joshi

2020 JINST 15 P10017

Florida State University, Tallahassee, U.S.A.

T. Adams, A. Askew, R. Habibullah, S. Hagopian, V. Hagopian, K.F. Johnson, R. Khurana, T. Kolberg, G. Martinez, T. Perry, H. Prosper, C. Schiber, R. Yohay, J. Zhang

Florida Institute of Technology, Melbourne, U.S.A.

M.M. Baarmand, M. Hohlmann, D. Noonan, M. Rahmani, M. Saunders, F. Yumiceva

University of Illinois at Chicago (UIC), Chicago, U.S.A.

M.R. Adams, L. Apanasevich, R.R. Betts, R. Cavanaugh, X. Chen, S. Dittmer, O. Evdokimov, C.E. Gerber, D.A. Hangal, D.J. Hofman, V. Kumar, C. Mills, G. Oh, T. Roy, M.B. Tonjes, N. Varelas, J. Viinikainen, H. Wang, X. Wang, Z. Wu

The University of Iowa, Iowa City, U.S.A.

M. Alhusseini, B. Bilki[55], K. Dilsiz[74], S. Durgut, R.P. Gandrajula, M. Haytmyradov, V. Khristenko, O.K. Köseyan, J.-P. Merlo, A. Mestvirishvili[75], A. Moeller, J. Nachtman, H. Ogul[76], Y. Onel, F. Ozok[77], A. Penzo, C. Snyder, E. Tiras, J. Wetzel, K. Yi[78]

Johns Hopkins University, Baltimore, U.S.A.

B. Blumenfeld, A. Cocoros, N. Eminizer, A.V. Gritsan, W.T. Hung, S. Kyriacou, P. Maksimovic, C. Mantilla, J. Roskes, M. Swartz, T.Á. Vámi

The University of Kansas, Lawrence, U.S.A.

C. Baldenegro Barrera, P. Baringer, A. Bean, S. Boren, A. Bylinkin, T. Isidori, S. Khalil, J. King, G. Krintiras, A. Kropivnitskaya, C. Lindsey, W. Mcbrayer, N. Minafra, M. Murray, C. Rogan, C. Royon, S. Sanders, E. Schmitz, J.D. Tapia Takaki, Q. Wang, J. Williams, G. Wilson

Kansas State University, Manhattan, U.S.A.

S. Duric, A. Ivanov, K. Kaadze, D. Kim, Y. Maravin, D.R. Mendis, T. Mitchell, A. Modak, A. Mohammadi

Lawrence Livermore National Laboratory, Livermore, U.S.A.

F. Rebassoo, D. Wright

University of Maryland, College Park, U.S.A.

A. Baden, O. Baron, A. Belloni, S.C. Eno, Y. Feng, N.J. Hadley, S. Jabeen, G.Y. Jeng, R.G. Kellogg, A.C. Mignerey, S. Nabili, M. Seidel, A. Skuja, S.C. Tonwar, L. Wang, K. Wong

Massachusetts Institute of Technology, Cambridge, U.S.A.

D. Abercrombie, B. Allen, R. Bi, S. Brandt, W. Busza, I.A. Cali, M. D'Alfonso, G. Gomez Ceballos, M. Goncharov, P. Harris, D. Hsu, M. Hu, M. Klute, D. Kovalskyi, Y.-J. Lee, P.D. Luckey, B. Maier, A.C. Marini, C. Mcginn, C. Mironov, S. Narayanan, X. Niu, C. Paus, D. Rankin, C. Roland, G. Roland, Z. Shi, G.S.F. Stephans, K. Sumorok, K. Tatar, D. Velicanu, J. Wang, T.W. Wang, B. Wyslouch

University of Minnesota, Minneapolis, U.S.A.

R.M. Chatterjee, A. Evans, S. Guts[†], P. Hansen, J. Hiltbrand, Sh. Jain, Y. Kubota, Z. Lesko, J. Mans, M. Revering, R. Rusack, R. Saradhy, N. Schroeder, N. Strobbe, M.A. Wadud

2020 JINST 15 P10017

University of Mississippi, Oxford, U.S.A.

J.G. Acosta, S. Oliveros

University of Nebraska-Lincoln, Lincoln, U.S.A.

K. Bloom, S. Chauhan, D.R. Claes, C. Fangmeier, L. Finco, F. Golf, R. Kamalieddin, I. Kravchenko, J.E. Siado, G.R. Snow[†], B. Stieger, W. Tabb

State University of New York at Buffalo, Buffalo, U.S.A.

G. Agarwal, C. Harrington, I. Iashvili, A. Kharchilava, C. McLean, D. Nguyen, A. Parker, J. Pekkanen, S. Rappoccio, B. Roozbahani

Northeastern University, Boston, U.S.A.

G. Alverson, E. Barberis, C. Freer, Y. Haddad, A. Hortiangtham, G. Madigan, B. Marzocchi, D.M. Morse, V. Nguyen, T. Orimoto, L. Skinnari, A. Tishelman-Charny, T. Wamorkar, B. Wang, A. Wisecarver, D. Wood

Northwestern University, Evanston, U.S.A.

S. Bhattacharya, J. Bueghly, G. Fedi, A. Gilbert, T. Gunter, K.A. Hahn, N. Odell, M.H. Schmitt, K. Sung, M. Velasco

University of Notre Dame, Notre Dame, U.S.A.

R. Bucci, N. Dev, R. Goldouzian, M. Hildreth, K. Hurtado Anampa, C. Jessop, D.J. Karmgard, K. Lannon, W. Li, N. Loukas, N. Marinelli, I. Mcalister, F. Meng, Y. Musienko[36], R. Ruchti, P. Siddireddy, G. Smith, S. Taroni, M. Wayne, A. Wightman, M. Wolf

The Ohio State University, Columbus, U.S.A.

J. Alimena, B. Bylsma, B. Cardwell, L.S. Durkin, B. Francis, C. Hill, W. Ji, A. Lefeld, T.Y. Ling, B.L. Winer

Princeton University, Princeton, U.S.A.

G. Dezoort, P. Elmer, J. Hardenbrook, N. Haubrich, S. Higginbotham, A. Kalogeropoulos, S. Kwan, D. Lange, M.T. Lucchini, J. Luo, D. Marlow, K. Mei, I. Ojalvo, J. Olsen, C. Palmer, P. Piroué, D. Stickland, C. Tully

University of Puerto Rico, Mayaguez, U.S.A.

S. Malik, S. Norberg

Purdue University, West Lafayette, U.S.A.

A. Barker, V.E. Barnes, R. Chawla, S. Das, L. Gutay, M. Jones, A.W. Jung, B. Mahakud, D.H. Miller, G. Negro, N. Neumeister, C.C. Peng, S. Piperov, H. Qiu, J.F. Schulte, N. Trevisani, F. Wang, R. Xiao, W. Xie

Purdue University Northwest, Hammond, U.S.A.

T. Cheng, J. Dolen, N. Parashar

Rice University, Houston, U.S.A.

A. Baty, U. Behrens, S. Dildick, K.M. Ecklund, S. Freed, F.J.M. Geurts, M. Kilpatrick, A. Kumar, W. Li, B.P. Padley, R. Redjimi, J. Roberts, J. Rorie, W. Shi, A.G. Stahl Leiton, Z. Tu, A. Zhang

2020 JINST 15 P10017

University of Rochester, Rochester, U.S.A.

A. Bodek, P. de Barbaro, R. Demina, J.L. Dulemba, C. Fallon, T. Ferbel, M. Galanti, A. Garcia-Bellido, O. Hindrichs, A. Khukhunaishvili, E. Ranken, R. Taus

Rutgers, The State University of New Jersey, Piscataway, U.S.A.

B. Chiarito, J.P. Chou, A. Gandrakota, Y. Gershtein, E. Halkiadakis, A. Hart, M. Heindl, E. Hughes, S. Kaplan, I. Laflotte, A. Lath, R. Montalvo, K. Nash, M. Osherson, S. Salur, S. Schnetzer, S. Somalwar, R. Stone, S. Thomas

University of Tennessee, Knoxville, U.S.A.

H. Acharya, A.G. Delannoy, S. Spanier

Texas A&M University, College Station, U.S.A.

O. Bouhali[79], M. Dalchenko, A. Delgado, R. Eusebi, J. Gilmore, T. Huang, T. Kamon[80], H. Kim, S. Luo, S. Malhotra, D. Marley, R. Mueller, D. Overton, L. Perniè, D. Rathjens, A. Safonov

Texas Tech University, Lubbock, U.S.A.

N. Akchurin, J. Damgov, V. Hegde, S. Kunori, K. Lamichhane, S.W. Lee, T. Mengke, S. Muthumuni, T. Peltola, S. Undleeb, I. Volobouev, Z. Wang, A. Whitbeck

Vanderbilt University, Nashville, U.S.A.

S. Greene, A. Gurrola, R. Janjam, W. Johns, C. Maguire, A. Melo, H. Ni, K. Padeken, F. Romeo, P. Sheldon, S. Tuo, J. Velkovska, M. Verweij

University of Virginia, Charlottesville, U.S.A.

L. Ang, M.W. Arenton, P. Barria, B. Cox, G. Cummings, J. Hakala, R. Hirosky, M. Joyce, A. Ledovskoy, C. Neu, B. Tannenwald, Y. Wang, E. Wolfe, F. Xia

Wayne State University, Detroit, U.S.A.

R. Harr, P.E. Karchin, N. Poudyal, J. Sturdy, P. Thapa

University of Wisconsin — Madison, Madison, WI, U.S.A.

K. Black, T. Bose, J. Buchanan, C. Caillol, D. Carlsmith, S. Dasu, I. De Bruyn, L. Dodd, C. Galloni, H. He, M. Herndon, A. Hervé, U. Hussain, A. Lanaro, A. Loeliger, R. Loveless, J. Madhusudanan Sreekala, A. Mallampalli, D. Pinna, T. Ruggles, A. Savin, V. Sharma, W.H. Smith, D. Teague, S. Trembath-reichert

†: Deceased
1: Also at Vienna University of Technology, Vienna, Austria
2: Also at Université Libre de Bruxelles, Bruxelles, Belgium
3: Also at IRFU, CEA, Université Paris-Saclay, Gif-sur-Yvette, France
4: Also at Universidade Estadual de Campinas, Campinas, Brazil
5: Also at Federal University of Rio Grande do Sul, Porto Alegre, Brazil
6: Also at UFMS, Nova Andradina, Brazil
7: Also at Universidade Federal de Pelotas, Pelotas, Brazil
8: Also at University of Chinese Academy of Sciences, Beijing, China
9: Also at Institute for Theoretical and Experimental Physics named by A.I. Alikhanov of NRC 'Kurchatov Institute', Moscow, Russia

2020 JINST 15 P10017

10: Also at Joint Institute for Nuclear Research, Dubna, Russia
11: Also at Suez University, Suez, Egypt
12: Now at British University in Egypt, Cairo, Egypt
13: Also at Purdue University, West Lafayette, U.S.A.
14: Also at Université de Haute Alsace, Mulhouse, France
15: Also at Erzincan Binali Yildirim University, Erzincan, Turkey
16: Also at CERN, European Organization for Nuclear Research, Geneva, Switzerland
17: Also at RWTH Aachen University, III. Physikalisches Institut A, Aachen, Germany
18: Also at University of Hamburg, Hamburg, Germany
19: Also at Brandenburg University of Technology, Cottbus, Germany
20: Also at Institute of Physics, University of Debrecen, Debrecen, Hungary, Debrecen, Hungary
21: Also at Institute of Nuclear Research ATOMKI, Debrecen, Hungary
22: Also at MTA-ELTE Lendület CMS Particle and Nuclear Physics Group, Eötvös Loránd University, Budapest, Hungary, Budapest, Hungary
23: Also at IIT Bhubaneswar, Bhubaneswar, India, Bhubaneswar, India
24: Also at Institute of Physics, Bhubaneswar, India
25: Also at G.H.G. Khalsa College, Punjab, India
26: Also at Shoolini University, Solan, India
27: Also at University of Hyderabad, Hyderabad, India
28: Also at University of Visva-Bharati, Santiniketan, India
29: Now at INFN Sezione di Bari [a], Università di Bari [b], Politecnico di Bari [c], Bari, Italy
30: Also at Italian National Agency for New Technologies, Energy and Sustainable Economic Development, Bologna, Italy
31: Also at Centro Siciliano di Fisica Nucleare e di Struttura Della Materia, Catania, Italy
32: Also at Riga Technical University, Riga, Latvia, Riga, Latvia
33: Also at Malaysian Nuclear Agency, MOSTI, Kajang, Malaysia
34: Also at Consejo Nacional de Ciencia y Tecnología, Mexico City, Mexico
35: Also at Warsaw University of Technology, Institute of Electronic Systems, Warsaw, Poland
36: Also at Institute for Nuclear Research, Moscow, Russia
37: Now at National Research Nuclear University 'Moscow Engineering Physics Institute' (MEPhI), Moscow, Russia
38: Also at St. Petersburg State Polytechnical University, St. Petersburg, Russia
39: Also at University of Florida, Gainesville, U.S.A.
40: Also at Imperial College, London, United Kingdom
41: Also at P.N. Lebedev Physical Institute, Moscow, Russia
42: Also at California Institute of Technology, Pasadena, U.S.A.
43: Also at INFN Sezione di Padova [a], Università di Padova [b], Padova, Italy, Università di Trento [c], Trento, Italy, Padova, Italy
44: Also at Budker Institute of Nuclear Physics, Novosibirsk, Russia
45: Also at Faculty of Physics, University of Belgrade, Belgrade, Serbia
46: Also at Università degli Studi di Siena, Siena, Italy
47: Also at INFN Sezione di Pavia [a], Università di Pavia [b], Pavia, Italy, Pavia, Italy
48: Also at National and Kapodistrian University of Athens, Athens, Greece
49: Also at Universität Zürich, Zurich, Switzerland
50: Also at Stefan Meyer Institute for Subatomic Physics, Vienna, Austria, Vienna, Austria
51: Also at Burdur Mehmet Akif Ersoy University, BURDUR, Turkey
52: Also at Şırnak University, Sirnak, Turkey
53: Also at Department of Physics, Tsinghua University, Beijing, China, Beijing, China

2020 JINST 15 P10017

54: Also at Near East University, Research Center of Experimental Health Science, Nicosia, Turkey
55: Also at Beykent University, Istanbul, Turkey, Istanbul, Turkey
56: Also at Istanbul Aydin University, Application and Research Center for Advanced Studies (App. & Res. Cent. for Advanced Studies), Istanbul, Turkey
57: Also at Mersin University, Mersin, Turkey
58: Also at Piri Reis University, Istanbul, Turkey
59: Also at Ozyegin University, Istanbul, Turkey
60: Also at Izmir Institute of Technology, Izmir, Turkey
61: Also at Bozok Universitetesi Rektörlügü, Yozgat, Turkey
62: Also at Marmara University, Istanbul, Turkey
63: Also at Milli Savunma University, Istanbul, Turkey
64: Also at Kafkas University, Kars, Turkey
65: Also at Istanbul Bilgi University, Istanbul, Turkey
66: Also at Hacettepe University, Ankara, Turkey
67: Also at Adiyaman University, Adiyaman, Turkey
68: Also at Vrije Universiteit Brussel, Brussel, Belgium
69: Also at School of Physics and Astronomy, University of Southampton, Southampton, United Kingdom
70: Also at IPPP Durham University, Durham, United Kingdom
71: Also at Monash University, Faculty of Science, Clayton, Australia
72: Also at Bethel University, St. Paul, Minneapolis, U.S.A., St. Paul, U.S.A.
73: Also at Karamanoğlu Mehmetbey University, Karaman, Turkey
74: Also at Bingol University, Bingol, Turkey
75: Also at Georgian Technical University, Tbilisi, Georgia
76: Also at Sinop University, Sinop, Turkey
77: Also at Mimar Sinan University, Istanbul, Istanbul, Turkey
78: Also at Nanjing Normal University Department of Physics, Nanjing, China
79: Also at Texas A&M University at Qatar, Doha, Qatar
80: Also at Kyungpook National University, Daegu, Korea, Daegu, Korea

2020 JINST 15 P10017